Florida International University
FIU Digital Commons

FIU Electronic Theses and Dissertations | University Graduate School

11-6-2017

Thermodynamic Investigation of Yttria-Stabilized Zirconia (YSZ) System

Mohammad Asadikiya
masad005@fiu.edu

DOI: 10.25148/etd.FIDC004016
Follow this and additional works at: https://digitalcommons.fiu.edu/etd

Part of the Ceramic Materials Commons, Other Materials Science and Engineering Commons, and the Structural Materials Commons

Recommended Citation
Asadikiya, Mohammad, "Thermodynamic Investigation of Yttria-Stabilized Zirconia (YSZ) System" (2017). *FIU Electronic Theses and Dissertations*. 3550.
https://digitalcommons.fiu.edu/etd/3550

This work is brought to you for free and open access by the University Graduate School at FIU Digital Commons. It has been accepted for inclusion in FIU Electronic Theses and Dissertations by an authorized administrator of FIU Digital Commons. For more information, please contact dcc@fiu.edu.

FLORIDA INTERNATIONAL UNIVERSITY

Miami, Florida

THERMODYNAMIC INVESTIGATION OF YTTRIA-STABILIZED ZIRCONIA (YSZ) SYSTEM

A dissertation submitted in partial fulfillment of the

requirements for the degree of

DOCTOR OF PHILOSOPHY

in

MATERIALS SCIENCE AND ENGINEERING

by

Mohammad Asadikiya

2017

To: Dean John Volakis
College of Engineering and Computing

This dissertation, written by Mohammad Asadikiya, and entitled Thermodynamic Investigation of Yttria-Stabilized Zirconia (YSZ) System, having been approved in respect to style and intellectual content, is referred to you for judgment.

We have read this dissertation and recommend that it be approved.

_____
Surendra K. Saxena

_____
Jiuhua Chen

_____
Norman D. H. Munroe

_____
Wenzhi Li

_____
Yu Zhong, Major Professor

Date of Defense: November 6, 2017

The dissertation of Mohammad Asadikiya is approved.

_____
Dean John Volakis
College of Engineering and Computing

_____
Andrés G. Gil
Vice President for Research and Economic Development
and Dean of the University Graduate School

Florida International University, 2017

© Copyright 2017 by Mohammad Asadikiya

All rights reserved.

Journal of Materials Science, Oxygen ion mobility and conductivity prediction in cubic yttria-stabilized zirconia single crystals, 2017, 1-11, Asadikiya, Mohammad, and Yu Zhong, © Springer Science + Business Media, LLC 2017 "With permission of Springer".

Asadikiya, Mohammad, et al. "Phase diagram for a nano-yttria-stabilized zirconia system." RSC Advances 6.21 (2016): 17438-17445 - Reproduced by permission of The Royal Society of Chemistry.

DEDICATION

I dedicate this dissertation to my dear parents and my beloved wife. Without their support, patience, understanding, inspiration, and love, the completion of this dissertation would have never been possible, undoubtedly.

ACKNOWLEDGMENTS

I would like to thank the committee members for their support and good humor. Their gentle but firm direction is mostly appreciated. I would also like to express my appreciation to my major advisor, Dr. Yu Zhong, whose support and patience considerably enhanced my path towards completion of this dissertation. From the beginning, he was a real companion to help solving the project-related problems. All of his technical supports, scientific advices, and kindnesses are greatly appreciated.

The Doctoral Evidence Acquisition (DEA) Fellowship from Graduate School of Florida International University is highly acknowledged.

The Royal Society of Chemistry and Springer are greatly acknowledged for their permissions to reproduce the published materials in this dissertation.

ABSTRACT OF THE DISSERTATION

THERMODYNAMIC INVESTIGATION OF YTTRIA-STABILIZED ZIRCONIA (YSZ) SYSTEM

by

Mohammad Asadikiya

Florida International University, 2017

Miami, Florida

Professor Yu Zhong, Major Professor

The yttria-stabilized zirconia (YSZ) system has been extensively studied because of its critical applications, like solid oxide fuel cells (SOFCs), oxygen sensors, and jet engines. However, there are still important questions that need to be answered and significant thermodynamic information that needs to be provided for this system. There is no predictive tool for the ionic conductivity of the cubic-YSZ (c-YSZ), as an electrolyte in SOFCs. In addition, no quantitative diagram is available regarding the oxygen ion mobility in c-YSZ, which is highly effective on its ionic conductivity. Moreover, there is no applicable phase stability diagram for the nano-YSZ, which is applied in oxygen sensors. Phase diagrams are critical tools to design new applications of materials. Furthermore, even after extensive studies on the thermodynamic database of the YSZ system, the zirconia-rich side of the system shows considerable uncertainties regarding the phase equilibria, which can make the application designs unreliable.

During this dissertation, the CALPHAD (CALculation of PHase Diagrams) approach was applied to provide a predictive diagram for the ionic conductivity of the c-YSZ system. The oxygen ion mobility, activation energy, and pre-exponential factor were also predicted.

In addition, the CALPHAD approach was utilized to predict the Gibbs energy of bulk YSZ at different temperatures. The surface energy of each polymorph was then added to the predicted Gibbs energy of bulk YSZ to obtain the total Gibbs energy of nano-YSZ. Therefore, a 3-D phase stability diagram for the nano-YSZ system was provided, by which the stability range of each polymorph versus temperature and particle size are presented.

Re-assessment of the thermodynamic database of the YSZ system was done by applying the CALPHAD approach. All of the available thermochemical and phase equilibria data were evaluated carefully and the most reliable ones were selected for the Gibbs energy optimization process. The results calculated by the optimized thermodynamic database showed good agreement with the selected experimental data, particularly on the zirconia-rich side of the system.

TABLE OF CONTENTS

CHAPTER PAGE

CHAPTER 1: INTRODUCTION AND OUTLINE OF THE DISSERTATION 1
1.1. Introduction 1
1.1.1. Yttria-stabilized zirconia system 1
1.1.2. Computational thermodynamics 1
1.2. The objectives of this work 2
1.3. Dissertation outline 4

CHAPTER 2: THE BACKGROUND REVIEW AND METHODOLOGY 6
2.1. Background and methodology 6
2.1.1. The CALPHAD approach 6
2.1.1.1. Modeling of the phases 7
2.1.1.1.1. Modeling of pure elements and stoichiometric compounds 8
2.1.1.1.2. Modeling of the multicomponent solution phases 8
2.1.2. Yttria-stabilized zirconia 9

CHAPTER 3: OXYGEN ION MOBILITY AND CONDUCTIVITY PREDICTION IN CUBIC YTTRIA-STABILIZED ZIRCONIA SINGLE CRYSTALS 11
3.1. Introduction 11
3.2. Background theories on the calculation of conductivity 12
3.3. Thermodynamic Modeling 13
3.4. Results and discussion 15
3.4.1. The overall approach 15
3.4.2. Prediction of oxygen vacancy concentration 17
3.4.3. Conductivity 18
3.4.4. Prediction of mobility, activation energy, and pre-exponential factor 24
3.4.4.1. Prediction of mobility 24
3.4.4.2. Prediction of activation energy 28
3.4.4.3. Prediction of pre-exponential factor 30
3.5. Conclusion 31

CHAPTER 4: PHASE DIAGRAM FOR NANO YTTRIA-STABILIZED ZIRCONIA SYSTEM 33
4.1. Introduction 33
4.2. Background review 34
4.3. Thermodynamic Modeling 35
4.3.1. Gibbs energy calculation for the bulk materials 35
4.3.2. T-zero temperature method to determine phase boundaries 37
4.3.3. Amorphous phase modeling 38
4.3.4. Gibbs energy calculation for nano particles 38
4.4. Results and discussion 39
4.5. Conclusion 49

CHAPTER 5: RE-EVALUATION OF THE THERMODYNAMIC EQUILIBRIA ON THE ZIRCONIA-RICH SIDE OF THE ZRO_2-$YO_{1.5}$ SYSTEM 51
5.1. Introduction 51
5.2. The recent discovery from the nano-YSZ phase diagram 53
5.3. Experimental data in the ZrO_2-$YO_{1.5}$ system 53
5.4. Thermodynamics and kinetics of ZrO_2-rich side and experimental data evaluation 55
5.5. Thermodynamic Modeling 58
5.6. Parameters optimization procedure and discussion of results 61
5.6.1. ZrO_2-$YO_{1.5}$ Phase diagram 65
5.6.2. T_0 method for the diffusionless phase transformation 69
5.6.3. Thermodynamic properties 74
5.7. Summary 76

CHAPTER 6: SUMMARY AND FUTURE WORKS 78
6.1. The contributions of this dissertation 78
6.2. The future works 80

LIST OF REFERENCES 81

APPENDICES 92

VITA 126

LIST OF FIGURES

FIGURE PAGE

Figure 1. Schematic picture of electrolyte function in the SOFCs. 4

Figure 2. The flowchart showing the process of database development in the CALPHAD approach. 7

Figure 3. Schematic picture of doping ZrO_2 by Y_2O_3. 10

Figure 4. Vacancy concertation vs. a) temperature and b) yttria content at 873K. 17

Figure 5. Site fraction of various species in c-YSZ vs. a) temperature for 6YSZ and b) yttria content at 873K..... 18

Figure 6. Predicted conductivity of c-YSZ single crystals. a) vs. reciprocal temperatures. The experimental data are from Pimenov et al. [36], Guo and Maier [57], Ramamoorthy et al. [59], and Liou and Worrell [58]. The inset table shows the activation energies, b) vs. yttria concentration at three different temperatures. The experimental data are from Liou and Worrell [58], Pimenov et al. [36], Ramamoorthy et al. [59], and Ikeda et al. [40]. 22

Figure 7. Predicted oxygen ion mobility. a) vs. temperature for 6YSZ. The experimental data were calculated using the conductivity measurements by Ramamoorthy et al. [59]. The equation of the mobility vs. temperature derived from this work is also shown, b) vs. yttria concentration at three different temperatures. The experimental data were calculated using the conductivity measurements by Ramamoorthy et al. [59], Pimenov et al. [36], Ikeda et al. [40], and Liou and Worrell [58]..... 27

Figure 8. The activation energy vs. YSZ composition at 1073K. The experimental and calculated data provided for comparison are by Ikeda et al. [40], Huang et al. [48], Sawaguchi and Ogawa [69], Pornprasertsuk et al. [45], Ramamoorthy et al. [59], Guo and Maier [57], Pimenov et al. [36], and Liou and Worrell [58]. The equation of the activation energy vs. Y_2O_3 content derived from this work is also shown. 29

Figure 9. The pre-exponential factor (A) vs. YSZ composition at 1073K. 31

Figure 10. Crystal structures of YSZ polymorphs [71, 72]. 33

Figure 11. T-zero temperature method. A) T_0 temperature as a point at a defined composition, B) T_0 temperature as a line when the composition changes..... 37

Figure 12. The Gibbs energy of monoclinic, tetragonal, cubic, and amorphous (supercooling liquid) phases vs. yttria mole fraction at room temperature for the bulk YSZ. 39

Figure 13. The Gibbs energy vs. yttria mole fraction at room temperature for n-YSZ with different particle sizes. 41

Figure 14. The phase diagram for n-YSZ system at room temperature in comparison with the experimental data which represent experimentally measured crystal structure by Drazin and Castro [17]. ★ sign indicates the largest tetragonal pure zirconia particle size experimentally observed [17]. (M: Monoclinic, T: Tetragonal, C: Cubic, A: Amorphous) 43

Figure 15. The phase diagram for n-YSZ system at 25, 100, 250, and 500˚C. (M: Monoclinic, T: Tetragonal, C: Cubic, A: Amorphous)..... 46

Figure 16. T_0 and T'_0 temperature lines related to bulk YSZ. (T_0 is M/T T-zero temperature line and T'_0 is T/C T-zero temperature line). 47

Figure 17. The changes of particle size vs. temperature for each boundary curve of n-0.01YSZ (Nano YSZ with 0. 01 mole fraction of Y_2O_3). 48

Figure 18. The 3-D phase diagram for n-YSZ system from different angles. 49

Figure 19. A) The ZrO_2-$YO_{1.5}$ quasi-binary phase diagram together with the experimental data from various groups. The phase diagram by Chen et al. [56] is shown in dash line. B) The ZrO_2-rich side comparing with the work by Chen et al. [56]..... 66

Figure 20. Schematic Gibbs energy diagram for the phases in ZrO_2-rich side of YSZ system. 70

Figure 21. The calculated $T_0^{m\text{-}t}$ line compared with the one calculated by Chen et al. [56] along with the experimental data. 71

Figure 22. The calculated $T_0^{t\text{-}c}$ line compared with the one calculated by Chen et al. [56] in dash line. 72

Figure 23- The calculated $T_0^{m\text{-}c}$ line compared with the one calculated by Chen et al [56] in dash line. 73

Figure 24.The activity of ZrO_2 in the c-ZrO_2 phase at 2773 K..... 74

Figure 25. The relative chemical potential of ZrO_2 in the c-ZrO_2 phase at 1273 K. 75

Figure 26. The heat capacity of c-ZrO_2 vs. temperature for $YO_{1.5}$ mole fraction of 0.2039. The C_p results calculated by the database from Chen et al. [56] are exactly the same as this work. 76

CHAPTER 1: INTRODUCTION AND OUTLINE OF THE DISSERTATION

1.1. Introduction

In this study, the thermodynamics of yttria-stabilized zirconia (YSZ) is investigated by applying the CALPHAD (Calculation of Phase Diagrams) approach. The main goal is developing accurate predictive tools to predict various properties and behaviors of the YSZ system, like ionic conductivity, phase equilibria, and thermochemical data.

1.1.1. Yttria-stabilized zirconia system

Yttria-stabilized zirconia (YSZ) is one of the most interesting ceramic systems, and has been studied extensively because of its critical applications. In the YSZ system, the zirconia (ZrO_2) is doped by yttria (Y_2O_3) to make its high-temperature phases stable at low temperatures. This material has several polymorphs including monoclinic, tetragonal, cubic and amorphous. Tetragonal polymorph is used as advanced structural ceramics like tooth crowns and jet engines since it has high toughness [1-3]. Cubic polymorph has the ability to conduct oxygen ions due to its high oxygen vacancy concentration, which increases by elevating temperature [2]. This characteristic of cubic polymorph is the reason of its applicability in solid oxide fuel cells (SOFCs), solid oxide electrolysis cells (SOECs), and oxygen sensors [4-7].

1.1.2. Computational thermodynamics

Computational approaches to design materials are effective tools, by which a lot of materials properties can be predicted in different conditions. They can provide valuable information about materials, which can be applied in designing new applications. For example, the CALPHAD approach can be applied to calculate phase equilibria of materials at different temperatures, which is called phase diagrams. Phase diagrams are advantageous

tools for effective design of engineering products. Various thermochemical data, like heat capacity, enthalpy, activity, and entropy, can also be derived by applying the CALPHAD approach [8].

In the CALPHAD approach as a method of computational thermodynamics, the Gibbs energy of each individual phase of a system is carefully modeled. The Gibbs energy of each phase can then be calculated accurately in different conditions. This characteristic state function could be applied to predict various properties of a system [9].

1.2. The objectives of this work

In the current work, three major objectives are followed.

The first objective is to develop a predictive tool for the ionic conductivity prediction of the YSZ cubic polymorph (c-YSZ). The c-YSZ polymorph is a very attractive material as the electrolyte of SOFCs [7]. Figure 1 shows the SOFC structure and the role of electrolyte schematically. Electrolytes should have high ionic conductivity and low electronic conduction. Therefore, knowing the ionic conductivity of c-YSZ in different conditions is very important to design the function of a SOFC. The c-YSZ ionic conductivity is highly dependent on the oxygen vacancy concentration. Predicting the concentration of oxygen vacancy in different conditions can lead to the prediction of c-YSZ ionic conductivity. This objective is fulfilled by applying the CALPHAD approach to predict the ionic conductivity of c-YSZ polymorph versus temperature and YSZ composition. The oxygen ion mobility, activation energy, and pre-exponential factor were also predicted.

The second objective is to develop a phase stability diagram for nano-YSZ (n-YSZ) system. The n-YSZ has critical applications due to its specific properties. For example, one important factor in the gas sensors is response time, which is related to the electrode

microstructure because of the effect of surface diffusion. Particles with smaller grain size and higher specific surface help reducing the response time. The larger surface area also causes higher catalytic activities [10]. The CALPHAD approach is applied in this work to predict the Gibbs energy of a bulk YSZ system. By considering the effect of surface energy, the total Gibbs energy of an n-YSZ system is developed. Therefore, by predicting the total Gibbs energy of each polymorph in a range of temperature, a 3-D phase diagram for n-YSZ system is developed, in which the crystal structure of the material is predicted based on the temperature, particle size, and the n-YSZ composition.

The third objective is to re-assess the thermodynamic database of a YSZ system. This objective was added to this work after observing a considerable discrepancy between the calculated tetragonal/cubic phase boundary and related experimental data in the developed n-YSZ phase stability diagram in the second objective. The YSZ thermodynamic database is optimized based on the most accurate experimental observations. The optimization focus is on the zirconia-rich side of the system. Therefore, the respective Gibbs energies of different involved phases in YSZ system are defined accurately. The newly developed YSZ thermodynamic database is reliable to derive various phase equilibria and thermochemical data of the YSZ system, which could be applied in developing new applications and improving the current ones.

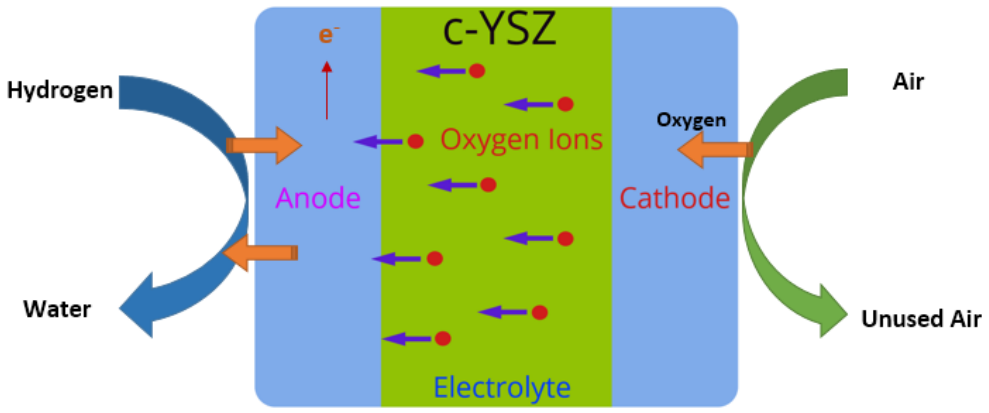

Figure 1. Schematic picture of electrolyte function in the SOFCs.

1.3. Dissertation outline

This work is organized into 6 chapters and 1 appendix.

Chapter 1, which is the current chapter, is the introduction. The system to study and the applied approach are briefly introduced. The objectives of the work are also discussed.

Chapter 2 presents the detailed background on the YSZ system and the CALPHAD approach.

Chapter 3 discusses objective one of this work, in which the ionic conductivity of c-YSZ polymorph is studied.

Chapter 4 explains the procedure of developing the n-YSZ phase stability diagram, including discussion of the final diagrams.

Chapter 5 describes the YSZ thermodynamic database optimization. The optimized parameters in addition to the calculated thermodynamic properties are discussed in this chapter.

Chapter 6 summarizes the outcomes of the present work and explains the contributions. The future works are also discussed in this chapter.

The details of the thermodynamic database optimization process including the POP file and setup file are shown in the appendix. The final YSZ thermodynamic database is also presented in the appendix.

CHAPTER 2: THE BACKGROUND REVIEW AND METHODOLOGY

2.1. Background and methodology

In this chapter, the CALPHAD approach is introduced and its details are explained. The YSZ system is also discussed in this chapter and its significant applications are described.

2.1.1. The CALPHAD approach

CALPHAD is an acronym for the calculation of phase diagrams. It is in fact the computer coupling of phase diagrams and thermochemistry. The CALPHAD approach was actually rooted by Van Laar in 1908 [11], who utilized the Gibbs energy concept to study the phase equilibria. Many years later, the CALPHAD approach was officially pioneered by Kaufman and Bernstein [12], who published a textbook that discussed the quantitative computer calculation of phase diagrams. The CALPHAD approach is based on the modeling of the Gibbs energies of individual phases in the system. This characteristic state function is crucial because under constant temperature and pressure, the Gibbs energy is minimized at equilibrium. Temperature and pressure are the variables which are typically controlled in the experiments. The thermodynamic databases based on the Gibbs energies are then constructed using experimental data and software programs [9, 13]. The assessed thermodynamic database can be applied to predict the behavior and properties of different phases of a system at various conditions [14-18]. Figure 2 shows the process of defining the Gibbs energy of each phase during database development in the CALPHAD approach.

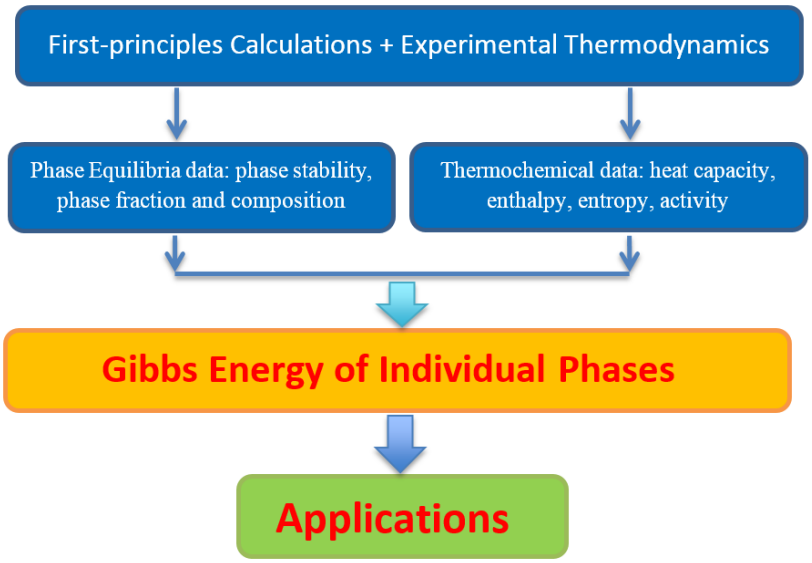

Figure 2. The flowchart showing the process of database development in the CALPHAD approach.

2.1.1.1. Modeling of the phases

One of the most applicable methods to model various phases of a system is sublattice modeling. This method is interesting due to its flexibility, which makes it possible to be accounted in a variety of phases including ionic liquid and crystalline compounds and solutions. A typical term used in the sublattice modelling method is site fraction (y_i^s), which means the fractional site occupation by each component (i) on the various sublattices (s). For example, if a four-component system is modeled by $(A,B)_a(C,D)_b$, it means species A and B occupy the first sublattice and species C and D occupy the second one and the ratio between first and second sublattices is a:b. The Gibbs energy of each phase is defined according to its model. It is worth mentioning that for a gas or liquid, which do not have crystallographic structure, the random substitutional model is applied. The positional occupation of the components in gases and liquids relies on random substitution rather than preferential occupation.

2.1.1.1.1. Modeling of pure elements and stoichiometric compounds

The Gibbs energy of a pure element or stoichiometric compound is defined by Equation 1, in which G is Gibbs energy, H is enthalpy, and S is entropy, all as a function of temperature and pressure.

$$G = H - TS \quad (1)$$

In a database developed by the CALPHAD approach, the model commonly used for pure elements and stoichiometric compounds is given as Equation 2 [19], which has been utilized by the Scientific Group Thermodata Europe (SGTE) [20].

$$G_m - H_m^{SER} = a + bT + cTln(T) + \sum_2^n d_n T^n \quad (2)$$

In this equation, a, b, c, and d_n are the model coefficients and n represents a set of integers, which is typically -1, 2, and 3. The $G_m - H_m^{SER}$ gives the Gibbs energy relative to a standard element reference state (SER) and the H_m^{SER} means the enthalpy of the element or compound in its determined reference state at 298.15 K.

2.1.1.1.2. Modeling of the multicomponent solution phases

A general definition of the Gibbs energy of a multicomponent solution is as Equation 3, in which the G_m is the total Gibbs energy of mixing, $^{\circ}G_m$ is the Gibbs energy of pure components in the mechanical mixing state, $^{ideal}G_m$ represents the Gibbs energy of ideal solution which gives the configurational entropy of mixing, and $^{xs}G_m$ denotes the excess Gibbs energy which is from the interactions between the components.

$$G_m = {}^{\circ}G_m + {}^{ideal}G_m + {}^{xs}G_m \quad (3)$$

For a binary solution, which is modeled as $(A,B)_a(A,B)_b$, $^{\circ}G_m$, $^{ideal}G_m$, and $^{xs}G_m$ are given by Equations 4, 5, and 6, respectively.

$$^{\circ}G_m = y_A^I y_A^{II\,\circ}G_{A:A} + y_A^I y_B^{II\,\circ}G_{A:B} + y_B^I y_A^{II\,\circ}G_{B:A} + y_B^I y_B^{II\,\circ}G_{B:B} \quad (4)$$

$$^{ideal}G_m = aRT[y_A^I \ln(y_A^I) + y_B^I \ln(y_B^I)] + bRT[y_A^{II} \ln(y_A^{II}) + y_B^{II} \ln(y_B^{II})] \quad (5)$$

$$^{xs}G_m = y_A^I y_B^I \left[y_A^{II} \sum_{k=0} {}^kL_{A,B:A}(y_A^I - y_B^I)^k + y_B^{II} \sum_{k=0} {}^kL_{A,B:B}(y_A^I - y_B^I)^k\right] +$$

$$y_A^{II} y_B^{II} \left[y_A^I \sum_{k=0} {}^kL_{A:A,B}(y_A^{II} - y_B^{II})^k + y_B^I \sum_{k=0} {}^kL_{B:A,B}(y_A^{II} - y_B^{II})^k\right] \quad (6)$$

${}^kL_{A,B:B}$ is the interaction parameter between species A and B in the first sublattice, while is expressing in regard to species B in the second sublattice. The term k determines the type of solution. If k=0, the solution is regular, if k=1, the solution is sub-regular, and if k=2, the solution will be sub-sub-regular. In other words, when the interaction parameter is independent of composition, then the solution is regular. But when the interaction parameter changes with composition linearly, the solution is sub-regular. When the k=2, the interaction parameter changes with composition non-linearly and the solution is sub-sub-regular. It is worth noting that k does not usually rise above 2 in practice and if rising k above 2 is found necessary, then presumably the chosen model to represent the phase is incorrect [8]. The summation of Equations 4, 5, and 6 constructs an equation called Redlich-Kister polynomial equation [21].

2.1.2. Yttria-stabilized zirconia

Pure zirconia (ZrO_2) has limited applications because of the disruptive monoclinic-tetragonal phase transformation [22]. ZrO_2 undergoes a phase transformation from monoclinic, which is stable at room temperature, to tetragonal at about 1170˚C and then to cubic at about 2370˚C [23-25]. During monoclinic-tetragonal phase transformation in ZrO_2, a large volume change happens [22, 24], which can cause cracks in the sample. In addition, cubic phase in ZrO_2 is only stable at very high temperatures [24], which restricts its applications. However, Ruff and Ebert [26] found that the phase transformations in ZrO_2 can be suppressed by doping zirconia with the specific concentrations of MgO, CaO,

Sc_2O_3, Y_2O_3, or CeO_2. Therefore, a metastable tetragonal or cubic solid solution can be achieved at low temperatures, which makes their various applications possible. Among the abovementioned dopants to stabilize ZrO_2, yttria (Y_2O_3) is of particular interest due to the specific properties of ZrO_2-Y_2O_3 (YSZ) system. When the appropriate amount of Y_2O_3 is applied to dope ZrO_2, fully stabilized zirconia (FSZ) with cubic fluorite structure is produced. If the ZrO_2 is doped with the smaller concentrations of Y_2O_3, partially stabilized zirconia (PSZ) with tetragonal structure is produced. Tetragonal polymorph is considered as advanced structural ceramics like tooth crowns, jet engines, and thermal barrier coatings (TBC) since it has high toughness, high melting point, low thermal conductivity, and high chemical stability [1-3, 27, 28]. Cubic fluorite polymorph is applied in oxygen sensors and solid oxide fuel cells (SOFCs) as an electrolyte due to its high ionic conductivity, which is attributed to its high oxygen vacancy concentration [4-6, 29-31]. Yttria makes cubic or tetragonal phases stable by substitution of some of the Zr^{+4} ions with Y^{+3} ions, which the latter is larger than the former. This produces oxygen vacancies, as three O^{-2} ions replace four O^{-2} ions [32]. Figure 3 shows the ZrO_2 doping by Y_2O_3 schematically.

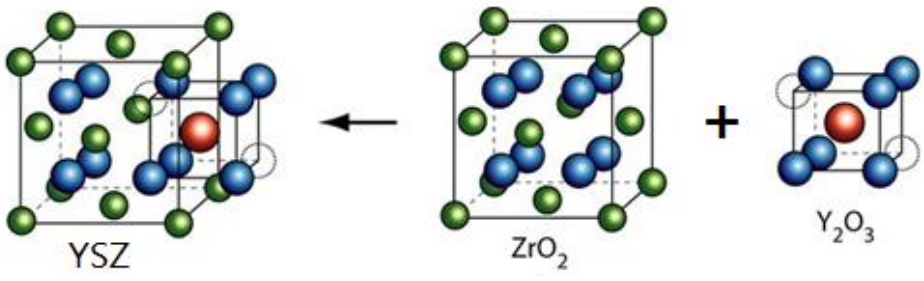

Figure 3. Schematic picture of doping ZrO_2 by Y_2O_3.

CHAPTER 3: OXYGEN ION MOBILITY AND CONDUCTIVITY PREDICTION IN CUBIC YTTRIA-STABILIZED ZIRCONIA SINGLE CRYSTALS

3.1. Introduction

Cubic yttria-stabilized zirconia (c-YSZ) is a well-known candidate as solid state electrolyte for solid oxide fuel cells (SOFCs). c-YSZ can be also applied in oxygen sensors and catalytic membrane reactors. It is attractive due to its high ionic conductivity, which is related to its high oxygen vacancy concentration [4, 29-31]. Doping zirconia with yttria can make c-YSZ stable at low temperatures by substitution of Zr^{+4} ions with Y^{+3} ions. This substitution produces oxygen vacancies, since three O^{-2} ions replace four O^{-2} ions [32].

Due to the critical role of c-YSZ as electrolyte in SOFCs, it is crucial to know its ionic conductivity at different conditions. Extensive studies have been carried out to measure the conductivity of c-YSZ with different compositions at various temperatures [33-37]. In addition, several investigations tried to discover the relationship between ionic conductivity of c-YSZ and the temperature, oxygen partial pressure, oxygen vacancy concentration, and concentration of yttria. Nakamura and Wagner reported that the ionic conductivity of c-YSZ is a function of oxygen vacancy concentration and temperature [4]. Luo et al. claimed that the composition of c-YSZ affects its conductivity [38]. Park and Blumenthal measured the ionic conductivity of 8 mole% YSZ in a range of temperature and oxygen partial pressure [39]. The highest ionic conductivity has been reported to be for around 8 mole% YSZ [36, 38, 40]. Besides experimental approaches, simulation methods, which are useful tools to predict the properties of materials [41], have been extensively applied to investigate the conductivity of YSZ [42-45]. Pornprasertsuk et al. applied first-principles calculations to predict the ionic conductivity of YSZ [45]. They

used density-functional theory (DFT) to calculate the energy barriers that oxygen ions encounter during migration in YSZ by a vacancy mechanism. The kinetic Monte Carlo (KMC) simulations were then performed based on the calculated DFT barriers to study the effect of yttria concentration on the oxygen diffusion coefficient. Other studies performed molecular dynamics (MD) simulations to investigate the oxygen ion diffusion in YSZ [46-48]. However, to the best of my knowledge, a quantitative mobility diagram to show the effect of yttria concentration and also temperature on the oxygen ion mobility in c-YSZ is still not available. Furthermore, there is no oxygen vacancy concentration quantitative diagram in various temperatures and YSZ compositions. In addition, it is not easily possible to experimentally measure the conductivity of low yttria content c-YSZ, since cubic-tetragonal phase transformation interferes. Therefore, there is lack of studies on the conductivity of c-YSZ with low yttria concentration.

In the current study, the CALPHAD (calculation of phase diagrams) approach was applied to predict the conductivity of c-YSZ single crystals with different compositions, at various temperatures. A similar work was carried out by Darvish et al., in which they applied the CALPHAD approach to develop predictive diagrams for the electronic conductivity of $La_{0.8}Sr_{0.2}MnO_{3\pm\delta}$ perovskite [49, 50]. In this work, the oxygen ion mobility for various compositions of c-YSZ was also calculated at different temperatures. Therefore, a predictive conductivity diagram was developed, in which the conductivity of c-YSZ single crystals is predicted versus its composition in a range of temperature.

3.2. Background theories on the calculation of conductivity

Equation 1 shows the parameters, which affect the ionic conductivity. In this equation, σ is the ionic conductivity, z is the charge of carrier, n is the concentration of carrier, and μ

is the mobility of ions [51, 52].

$$\sigma = zn\mu \quad (1)$$

In c-YSZ, the carrier is oxygen vacancy, therefore, z is 2e (e is the electronic charge of electron), n is oxygen vacancy concentration ($[V_O^{\cdot\cdot}]$), and μ is the mobility of oxygen ions. The mobility of oxygen ions is determined by the following traditional Arrhenius equation [4, 53].

$$\mu = \frac{A}{T}\exp\left(-\frac{E_a}{kT}\right) \quad (2)$$

In Equation 2, A is the pre-exponential factor, T is the temperature in K, E_a is the activation energy, and k is the Boltzmann constant. The pre-exponential factor is consisted of several parameters, including geometric factor, which depends on the crystal structure, jump distance, which is related to the lattice parameter, and vacancy hopping rate [54].

According to Equation 1, to calculate the ionic conductivity of c-YSZ, the two key parameters i.e. oxygen ion mobility and the oxygen vacancy concentration should be known in each condition.

3.3. Thermodynamic Modeling

The CALPHAD approach is based on the modeling of the Gibbs energies of individual phases in the system. This characteristic state function is crucial because under constant temperature and pressure, the Gibbs energy is minimized at equilibrium. Temperature and pressure are the variables that typically controlled in the experiments. The thermodynamic databases based on the Gibbs energies are then constructed using experimental data and software programs [9, 13]. The assessed thermodynamic database can be applied to predict the behavior and properties of different phases of a system at various conditions [14-18, 55].

The latest thermodynamic database for the ZrO_2-Y_2O_3 system, which has been developed by Chen et al. [56], was applied in the current study to predict the oxygen vacancy concentration of c-YSZ at different conditions. The model used for c-YSZ phase in this database is $(Y,Y^{3+},Zr,Zr^{4+})_1(O^{2-},Va)_2$. The Gibbs energy definition of c-YSZ phase is as Equation 3. It is worth mentioning that the presence of Y and Zr elements in the model is due to the possible ionization or recombination at extreme conditions. Therefore, the model is mainly controlled by the ions along with vacancy at the regular conditions.

$$G_m = y_{Y^{3+}} y_{O^{2-}} {}^{\circ}G_{Y^{3+}:O^{2-}} + y_{Zr^{4+}} y_{O^{2-}} {}^{\circ}G_{Zr^{4+}:O^{2-}} + y_{Y^{3+}} y_{Va} {}^{\circ}G_{Y^{3+}:Va} + y_{Zr^{4+}} y_{Va} {}^{\circ}G_{Zr^{4+}:Va} + y_Y y_{O^{2-}} {}^{\circ}G_{Y:O^{2-}} + y_{Zr} y_{O^{2-}} {}^{\circ}G_{Zr:O^{2-}} + y_Y y_{Va} {}^{\circ}G_{Y:Va} + y_{Zr} y_{Va} {}^{\circ}G_{Zr:Va} + RT[y_Y \ln y_Y + y_{Y^{3+}} \ln y_{Y^{3+}} + y_{Zr} \ln y_{Zr} + y_{Zr^{4+}} \ln y_{Zr^{4+}} + 2(y_{O^{2-}} \ln y_{O^{2-}} + y_{Va} \ln y_{Va})] + {}^{E}G_m \quad (3)$$

where y_j is site fraction of specie j in a particular sublattice. ${}^{\circ}G_{a:b}$ represents the standard Gibbs energy when the first sublattice is occupied by species a and the second one is occupied by species b. The excess Gibbs energy ${}^{E}G_m$, which includes the interactions between atoms in the solution, is defined as Equation 4.

$${}^{E}G_m = y_{Y^{3+}} y_{Zr^{4+}} y_{O^{2-}} \sum_{i=0}^{n} {}^{i}L_{Y^{3+},Zr^{4+}:O^{2-}} (y_{Y^{3+}} - y_{Zr^{4+}})^i + y_{Y^{3+}} y_{Zr^{4+}} y_{Va} \sum_{i=0}^{n} {}^{i}L_{Y^{3+},Zr^{4+}:Va} (y_{Y^{3+}} - y_{Zr^{4+}})^i + y_{Zr} y_{Zr^{4+}} y_{O^{2-}} \sum_{i=0}^{n} {}^{i}L_{Zr,Zr^{4+}:O^{2-}} (y_{Zr} - y_{Zr^{4+}})^i + y_{Zr} y_{Zr^{4+}} y_{Va} \sum_{i=0}^{n} {}^{i}L_{Zr,Zr^{4+}:Va} (y_{Zr} - y_{Zr^{4+}})^i \quad (4)$$

where ${}^{i}L_{a,b:c}$ is the interaction parameter when species a and b have occupied the first sublattice and species c has occupied the second one. Interaction parameter is written in the form of A+BT. i=0 represents the regular solution, i=1 represents the sub-regular solution, and i=2 represents the sub-sub-regular solution. The c-YSZ phase was considered as a sub-regular solution in this database [56], in which the interaction parameter changes linearly with the composition. The model clearly indicates that the yttrium ions can only

occupy the zirconium sites. Vacancies are produced in the oxygen sites to maintain the charge neutrality.

3.4. Results and discussion

In the first part of this section, the overall approach to develop a quantitative mobility diagram, the pre-exponential factor diagram, and the activation energy diagram is explained. In addition, the details of developing the conductivity diagrams in a range of temperature and yttria concentration is discussed. In the second part, the modeling results of oxygen vacancy concentration are presented and discussed. Finally in the third part, the developed quantitative mobility and conductivity diagrams are displayed and compared with the previous results from the literature. The diagrams of pre-exponential factor and activation energy are also presented and discussed.

3.4.1. The overall approach

Based on Equation 1, the mobility and the oxygen vacancy concentration are the two critical parameters to make the prediction of conductivity. There are various experimental measurements available on the conductivity of c-YSZ. It is desired to develop an approach to systematically investigate and predict the conductivity of c-YSZ in the composition and temperature regions outside of the available experimentally investigated areas. However, the main obstacle for the conductivity prediction is lacking of the reliable amount of oxygen vacancy concentration of c-YSZ. In the current work, the CALPHAD approach is applied to predict the oxygen vacancy concentration at different temperatures and c-YSZ compositions.

Since the effect of grain boundaries was not considered in the calculation of oxygen vacancy concentration, the simulations in the current work are applied only for c-YSZ

single crystals and only the experimental data for the c-YSZ single crystals were considered.

Although the available experimental data for the conductivity of c-YSZ single crystals in the literature is limited, the measured conductivity of c-YSZ single crystals at different conditions was carefully selected among the available ones.

The mobility can be predicted in different conditions when the conductivity and oxygen vacancy concentration are known. Therefore, the quantitative mobility diagrams were developed based on Equation 1, in a range of temperature and yttria concentration. By extrapolating the preliminary mobility diagrams, final versions of such diagrams were plotted in an extended temperature and c-YSZ composition ranges. Thus, the conductivity diagrams were developed based on Equation 1 since the oxygen ion mobility and oxygen vacancy concentration diagrams were developed in an extended range of temperature and c-YSZ composition. By combining Equations 1 and 2 and taking the natural logarithm of both sides, the following equation is obtained, in which A´ is znA.

$$\ln \sigma \mathrm{T} = \ln A' + \left(\frac{-E_a}{K}\right)\frac{1}{T} \quad (5)$$

Equation 5 dominates if the trend of $\ln \sigma$T versus inverse temperature is essentially linear. Based on Equation 5, the slope of the line in the $\ln \sigma$T-1/T diagram will be equal to $\frac{-E_a}{K}$, from which the activation energy (E_a) can be extracted. The Y-axis intercept of the line is ln A´, from which the pre-exponential factor (A) can be extracted. If the trend of $\ln \sigma$T-1/T diagram is linear, the E_a and A should be constant with temperature. However, if the $\ln \sigma$T trend versus inverse temperature is not completely linear, the E_a and A should be changed by temperature.

3.4.2. Prediction of oxygen vacancy concentration

Figure 4 shows the oxygen vacancy concentration of c-YSZ at different temperatures and YSZ compositions. The vacancy concentration does not change with the temperature, but it increases with increasing the yttria concentration, as demonstrated in Figure 4a and b respectively. The constant trend of oxygen vacancy concentration versus temperature is due to the high thermal formation energy of vacancies. In the other words, the number of vacancies formed thermally is negligible [45].

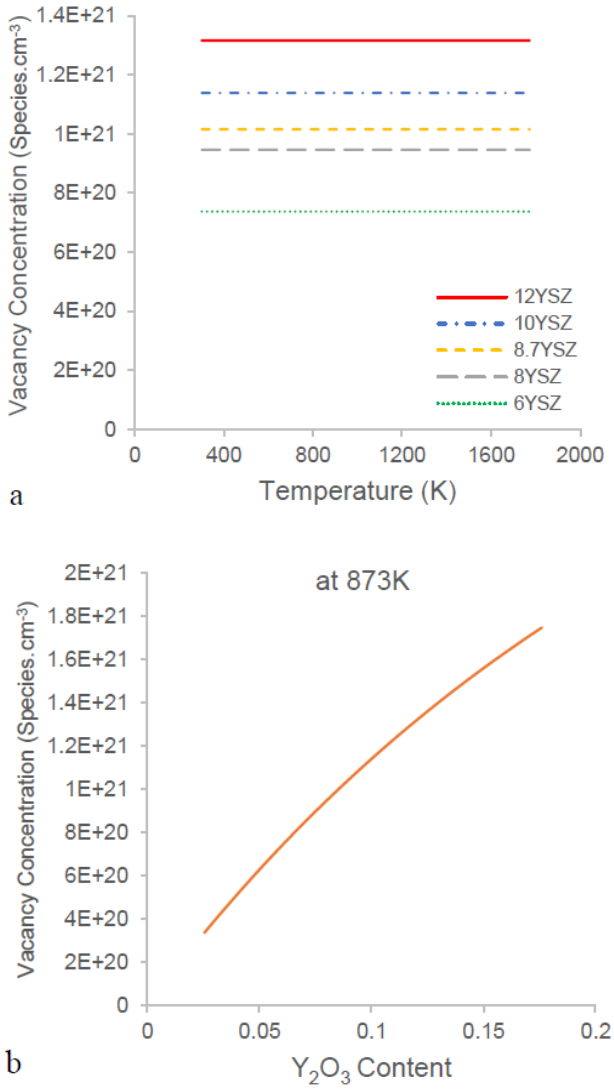

Figure 4. Vacancy concertation vs. a) temperature and b) yttria content at 873K.

Figure 5 shows the site fraction of each species in c-YSZ versus temperature and yttria concentration. The site fraction of all species are constant versus temperature, as indicated in Figure 5a; however, that of all species changes by yttria content, as indicated in Figure 5b. According to this figure, while the Y^{+3} ions substitute the Zr^{+4} ions, the vacancy concentration increases and the concentration of O^{-2} ions decreases. It is worth noting that the site fraction of Y and Zr is zero in both diagrams in Figure 5.

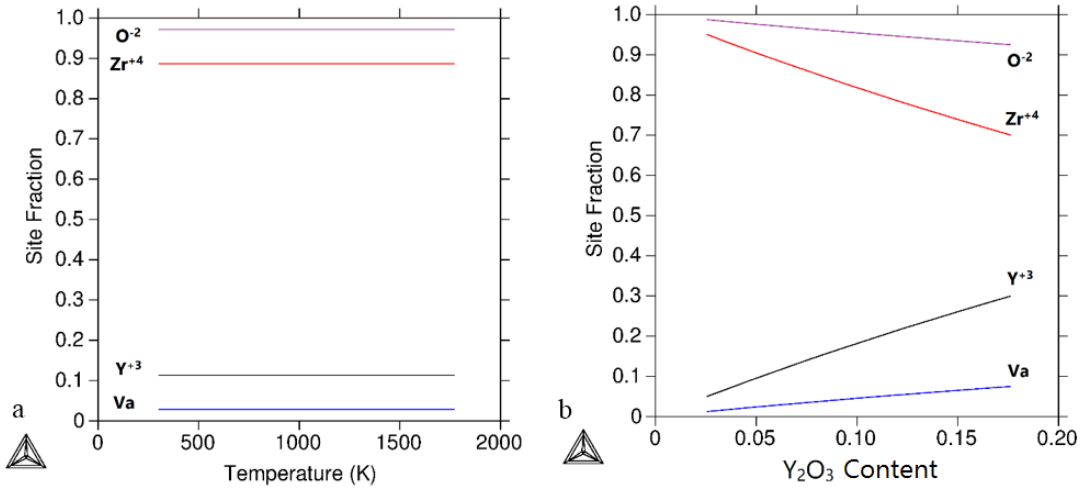

Figure 5. Site fraction of various species in c-YSZ vs. a) temperature for 6YSZ and b) yttria content at 873K.

3.4.3. Conductivity

There are experimental data available from various research groups for the conductivity of YSZ. The conductivity of YSZ single crystals was investigated by Ikeda et al. [40], and Pimenov et al. [36]. Meanwhile, polycrystalline YSZ samples were adopted to study the conductivity changes versus temperature and the YSZ composition by Guo and Maier [57], Liou and Worrell [58], and Ramamoorthy et al. [59]. The four-probe method and impedance spectroscopy method, which can differentiate the conductivity of lattice and grain boundary in the polycrystalline YSZ samples, were applied to measure the

conductivity. X-ray diffraction spectroscopy was also applied to characterize the crystal structure of YSZ samples. In the current work, I only focused on the lattice conductivity of c-YSZ, which should have the same value with the one measured from c-YSZ single crystals.

There are mainly two types of conductivity measurements. One is to measure the conductivity of c-YSZ with a specific composition versus reciprocal temperature, as shown in Figure 6a. The other one is to measure the conductivity of c-YSZ versus the yttria concentration at specific temperature as shown in Figure 6b.

In the current work, the mobility was tuned and combined with the oxygen vacancy concentration to reproduce the conductivity of c-YSZ single crystals. The oxygen vacancy concentration was taken from the simulation results as shown in Figure 4 and Figure 5. By knowing the oxygen vacancy concentration, Equation 1 was applied and the mobility data was tuned based on the accuracy of the reported conductivities in the literature, by examining all the experimental data simultaneously. The complete and self-consistent description of mobility is discussed in the next sub-section.

All of the experimental data from Figure 6a clearly show that the conductivity increases with the increase of temperature. However, the relationship between the conductivity and the YSZ composition is not clear, since the experimental data were gathered from different research groups. The main experimental data utilized in this work is from Ikeda et al. [40], which show the YSZ single crystals conductivity drops with the increase of yttria concentration at three different temperatures in the region that the yttria concentration is larger than 8 mole%. The second set of data are from Ramamoorthy et al. [59], which is the conductivity of 6YSZ at various temperatures. It shows the conductivity of 6YSZ is

lower than that of 8YSZ, which indicates that the conductivity drops by decreasing the yttria concentration below 8 mole%. In addition, Lou and Worrell [58] measured the conductivity for 12 YSZ, which is higher than that from Ikeda et al. Meanwhile, the 10 YSZ data measured by Pimenov [36] show lower conductivity than that from Ikeda et al., at 873 and 1073K. The experimental results by Liou and Worrell [58] contradict the results by Pimenov et al. [36], while confirmed by the results from Badwal et al. [60] and Abelard et al. [61]. Thus, the data by Liou and Worrell [58] was considered in this work for the mobility calculation. Except the data by Pimenov et al. [36], the rest of experimental data were considered equally for the calculation of mobility, since there were no technical preferences between them. It should be mentioned that the discrepancies between the experimental results of different groups are due to the fact that different groups may have slightly different standards in performing experiments [46], and also the quality of the samples used by each group might be slightly different. However, there is no information available to determine which group used the more pure samples and higher standards to do experiments.

According to the aforementioned assessments, in the first step of the parameter evaluation process, the $\log \sigma T$ lines for each YSZ compositions were fitted on the related available experimental data in Figure 6a. Based on the initial $\log \sigma T$-1/T relationship, the preliminary $\log \sigma T$ versus yttria content diagram was constructed. Using least-squares fitting technique, $\log \sigma T$-Y_2O_3 content diagram was fitted with the experimental data in Figure 6b, which was carried out by slight tunings of mobility (Figure 7b). It should be mentioned that the conductivity is affected by changing the mobility as explained in Equation 1 and the mobility can be adjusted by changing the activation energy as shown in Equation 2. In the

next step, the initial $\log \sigma$T-1/T was altered based on the updated $\log \sigma$T-Y_2O_3 content diagram to obtain the final $\log \sigma$T-1/T diagram. Therefore, the $\log \sigma$T-1/T and $\log \sigma$T-Y_2O_3 content diagrams were developed, as shown in Figure 6a and b, respectively. The compatibility of the two diagrams was checked several times to ensure one can be derived from the other accurately.

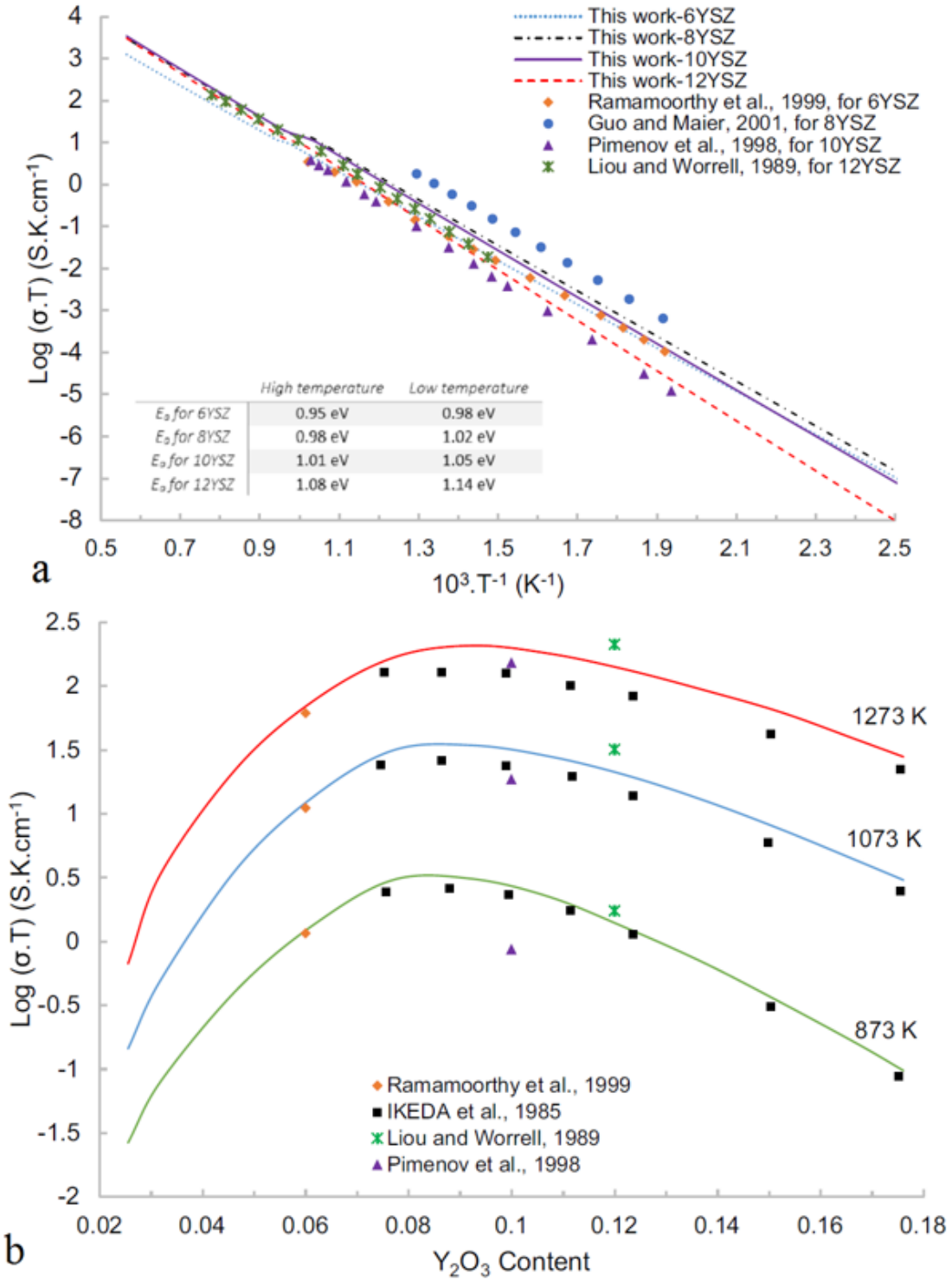

Figure 6. Predicted conductivity of c-YSZ single crystals. a) vs. reciprocal temperatures. The experimental data are from Pimenov et al. [36], Guo and Maier [57], Ramamoorthy et al. [59], and Liou and Worrell [58]. The inset table shows the activation energies, b) vs. yttria concentration at three different temperatures. The experimental data are from Liou and Worrell [58], Pimenov et al. [36], Ramamoorthy et al. [59], and Ikeda et al. [40].

The predicted log σT versus reciprocal temperature has linear trend in each section of before and after slight transition (Figure 6a). The conductivity of c-YSZ single crystals increases by increasing the temperature; however, the conductivity trends of different compositions are not parallel. At low temperatures, 10YSZ has lower conductivity than 6YSZ in Figure 6a, while its conductivity is higher than 6YSZ at high temperatures. This behavior is also indicated in Figure 6b, in which the conductivity differences between c-YSZ single crystals with the yttria content of higher than 8 mole% decreases by increasing the temperature. However, the slope of the conductivity curves increases by increasing the temperature, for the c-YSZ compositions with lower than 8 mole% yttria. In all the studied regions, the maximum conductivity belongs to c-YSZ with around 8 mole% yttria, as shown in Figure 6, which is in agreement with the previous works [36, 38, 40].

A transition in the slope of each conductivity line is seen in Figure 6a. This is because at higher temperatures, the activation energy is reduced due to the reduction in the effect of clusters. The barrier effect of clusters against movement of ions, which is high at low temperatures, considerably reduces at high temperatures [62]. This reduction causes a drop in the activation energy, which appears in the form of sudden change in the slope of the log σT-1/T graph. The transition temperature for YSZ is reported to be around 800˚C [47, 62].

As it is shown in Figure 6b, by decreasing the yttria content of c-YSZ from 8 mole%, the conductivity decreases dramatically. According to Figure 4b and Figure 5b, by decreasing the yttria content of c-YSZ, oxygen vacancy concentration decreases and results in the decrease of the oxygen ion mobility. Therefore, dramatic decrease in the conductivity of c-

YSZ is expected. According to Equation 1, the ionic conductivity is reduced toward zero when the vacancy concentration reduces toward zero.

One important contribution of this work is the prediction of the ionic conductivity of low yttria c-YSZ. As it is shown in Figure 6b, the conductivity of c-YSZ single crystals is plotted for the yttria concentration lower than 6 mole%. This became possible by predicting the oxygen vacancy concentration and the oxygen ion mobility at low yttria concentrations. Since sample preparation of low yttria c-YSZ is not easily possible due to tetragonal-cubic phase transformation, the ionic conductivity predictions in the current work could be of great importance. It is worth noting that due to sluggish kinetics of ZrO_2 rich side of the YSZ system, low yttria c-YSZ, which is thermodynamically stable at very high temperatures, can be stabilized at lower temperatures. This state is called frozen state of high-temperatures [25]. Moreover, various studies have observed the coexistence of cubic and tetragonal YSZ phases with low yttria content [40, 59, 60]. The predictions in the current work can provide the conductivity prediction for the cubic phase in such state.

3.4.4. Prediction of mobility, activation energy, and pre-exponential factor

3.4.4.1. Prediction of mobility

The mobility of oxygen ions in c-YSZ single crystals was predicted versus temperature and yttria concentration, as shown in Figure 7a and b, respectively. In Figure 7a, the mobility of 6YSZ single crystals is shown in a range of temperature. The same trend was observed for 8, 10, and 12YSZ single crystals. As it is shown in Figure 7a, the mobility of oxygen ions is increasing with the temperature increase. This behavior is also seen in Figure 7b.

According to Equation 2, the mobility is controlled by pre-exponential factor, activation energy, and temperature. Based on Figure 4a and Figure 5a, the concentration of oxygen

vacancy is constant with temperature, while the mobility increases with the temperature increase. One reason can be associated with the decrease of activation energy due to temperature increase [62]. Thus, the barrier against movement of ions is reduced by temperature increase. Other reason can be related to the altering of effective oxygen vacancy concentration by increasing the temperature.

According to Figure 4b and Figure 5b, the oxygen vacancy concentration increases with the yttria concentration increase. In contrast, although the mobility obeys the trend of the oxygen vacancy concentration and increases with the increase of yttria concentration until around 8YSZ, it starts to decrease after that (Figure 7b). One explanation for the mobility decrease after around 8YSZ is that the effective oxygen vacancy concentration decreases due to the formation of defect clusters. The cluster formation happens when the cations of the dopant and oxygen vacancies are associated at higher oxygen vacancy concentration [63-65]. Another possible reason for the mobility decrease can be related to interactions of the oxygen vacancies, which is considerable at higher oxygen vacancy concentrations [66, 67].

It is worth mentioning that the left side of the mobility diagram in Figure 7b for the yttria concentrations lower than 6 mole% was extrapolated toward the yttria concentration of zero. As the calculated mobility points for 6YSZ based on the conductivity measurements by Ramamoorthy et al. [59] show in Figure 7b, the mobility curve has descending trend below 8YSZ. Moreover, the ionic mobility and conductivity of YSZ is closely tied up with the presence of oxygen vacancies. Therefore, when the vacancy concentration decreases, the mobility reduces as well. As shown in Figure 4b and Figure 5b, the vacancy concentration decreases by decreasing the yttria concentration, which leads to mobility

decrease as shown in Figure 7b. Although based on the abovementioned explanations, it is believed that the general trend of the mobility is descending below the 8 mole% yttria toward zero, I assumed this descending trend is continuous. However, the descending trend might not happen continuously in real conditions. In other words, the probability of a sudden increase or a plateau during a general descending trend of mobility cannot be denied.

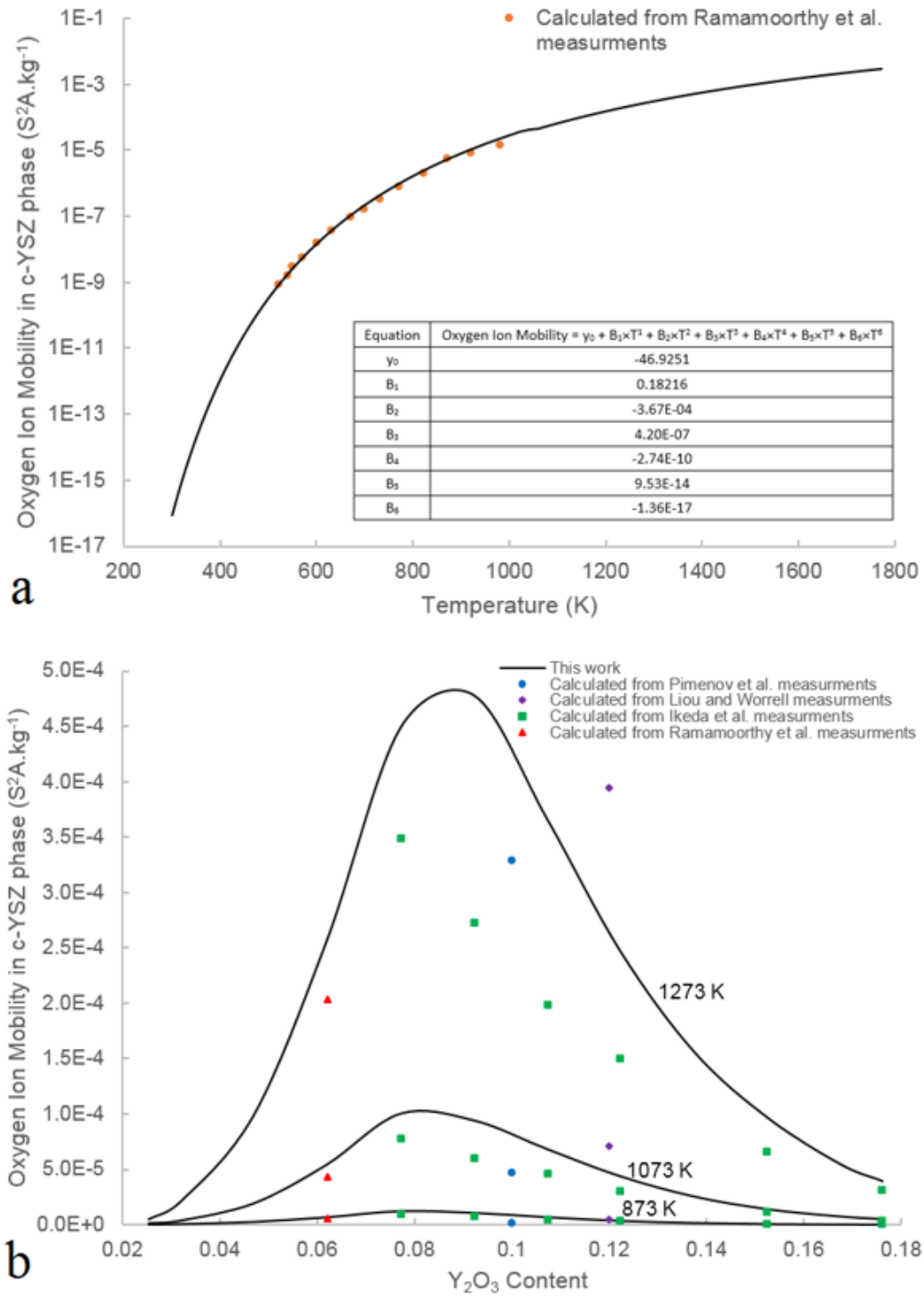

Figure 7. Predicted oxygen ion mobility. a) vs. temperature for 6YSZ. The experimental data were calculated using the conductivity measurements by Ramamoorthy et al. [59]. The equation of the mobility vs. temperature derived from this work is also shown, b) vs. yttria concentration at three different temperatures. The experimental data were calculated using the conductivity measurements by Ramamoorthy et al. [59], Pimenov et al. [36], Ikeda et al. [40], and Liou and Worrell [58].

3.4.4.2. Prediction of activation energy

The activation energy (E_a) for oxygen ion motion is composed of two parts, which are the migration energy (E_m) and the association energy (E_s) [62]. E_m is the energy consumed to move the oxygen ions from an occupied site to an empty site and E_s is the summation of energies related to the interaction between oxygen vacancies and dopant cations and interaction between oxygen vacancies with each other [62-65]. At low yttria concentrations, E_s is negligible. While by increasing the yttria concentration, the oxygen vacancy concentration increases, which leads to considerable interactions between vacancies and yttrium cations and also oxygen vacancies with each other. This phenomenon causes the increase of E_s. In addition, by increasing the Y_2O_3 concentration, oxygen ions need to diffuse across a Y-Y common edge relative to diffusion across a Zr-Y common edge. The Y-Y common edge provides higher energy barrier [68]. Therefore, E_m will also increases by increasing the yttria concentration. As it is shown in Figure 6b, by increasing the temperature, the slope of the curve on the right side of the graph decreases. In other words, the conductivity curves at different temperatures are not parallel. This may be related to the multiple effect of temperature on reducing the E_a. Particularly, increasing the temperature helps to reduce both the migration and association energies. The reduction of E_a is not linear since the conductivity curves at different temperatures are not parallel.

Figure 8 shows the activation energy versus yttria concentration at 1073K, extracted from the conductivity predictions in Figure 6. The results of different groups with various approaches are also presented in Figure 8. It is worth noting that the transition temperature in the current study occurs at the temperatures less than 1073K (Figure 6a). The activation energy increases by increasing the yttria concentration up to around 5 mole% Y_2O_3. After

that, it is close to a constant till 10 mole% Y_2O_3, similar to results from Ikeda et al. [40] and Pornprasertsuk et al. [45]. Meanwhile, the ionic conductivity increases in this range of yttria concentration (Figure 6b), which is due to the dominant effect of oxygen vacancy concentration increase in this region. After around 10 mole% yttria, dramatic increase of the activation energy is observed, which causes the decrease of the conductivity as shown in Figure 6b. The regions at low and high yttria concentration were extrapolated based on the reported trends of E_a in the literature.

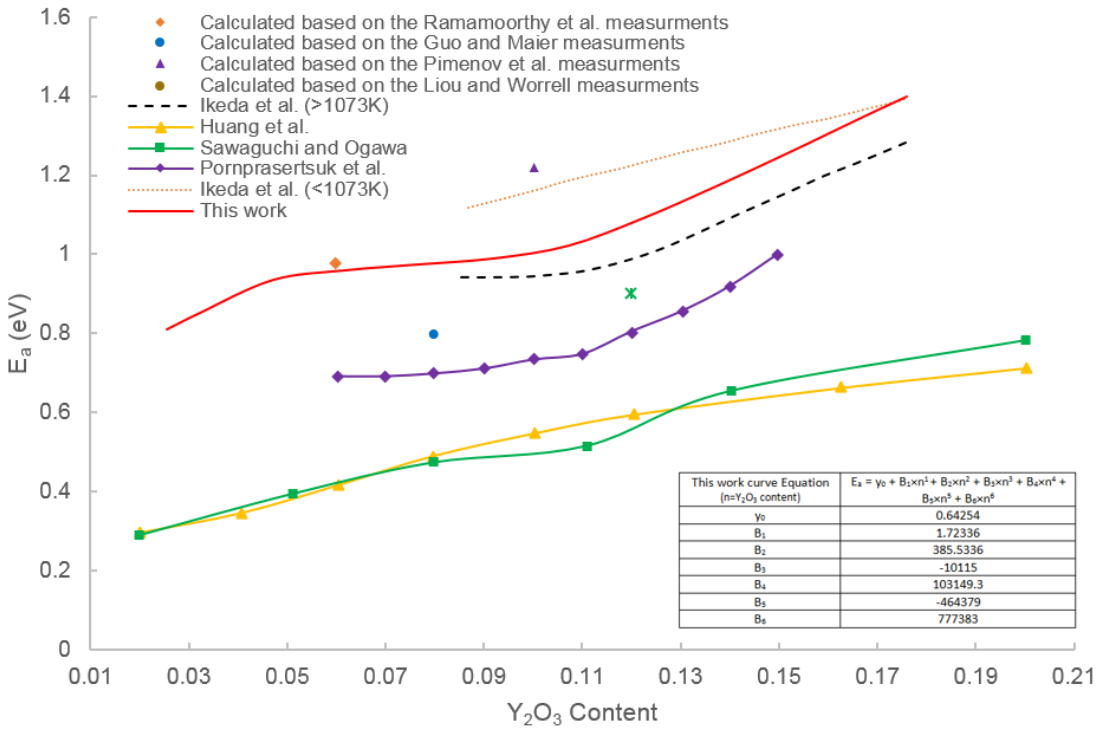

Figure 8. The activation energy vs. YSZ composition at 1073K. The experimental and calculated data provided for comparison are by Ikeda et al. [40], Huang et al. [48], Sawaguchi and Ogawa [69], Pornprasertsuk et al. [45], Ramamoorthy et al. [59], Guo and Maier [57], Pimenov et al. [36], and Liou and Worrell [58]. The equation of the activation energy vs. Y_2O_3 content derived from this work is also shown.

As it is shown in Figure 8, Huang et al. [48] and Sawaguchi and Ogawa [69] applied the MD method to simulate the oxygen ion diffusion in YSZ single crystals and derived the activation energy for oxygen ion diffusion. Pornprasertsuk et al. [45] also applied the first-

principles quantum simulations to calculate a set of energy barriers that oxygen ions encounter during migration in YSZ by a vacancy mechanism. Ikeda et al. [40] calculated the activation energy derived from the slope of $\log \sigma T$-1/T diagram they provided. The discrepancies between the predicted E_a in this work and calculated results from the literature are due to underestimations in the simulations by MD and DFT-KMC [45, 48, 70], because of limitations of the classical potentials and routine simplifications. For example, the interaction of oxygen vacancies and also interactions between oxygen vacancy and their outlying neighbors were neglected in MD and DFT-KMC calculations for simplicity.

3.4.4.3. Prediction of pre-exponential factor

In Figure 9, the pre-exponential factor (A) at 1073K, as introduced in Equation 2, is plotted versus Y_2O_3 concentration for the first time. It shows A is increasing with the yttria concentration increase, except between 8 to 11 mole% yttria. It is possible that the pre-exponential factor is affected in this region, due to cluster formations and vacancy interactions. But the effect of vacancy concentration increase on A is dominant after 11 mole% yttria, since the A-Y_2O_3 content graph resumes its ascending trend. It should be mentioned that the behavior of oxygen ion mobility is the outcome of both A and E_a trends.

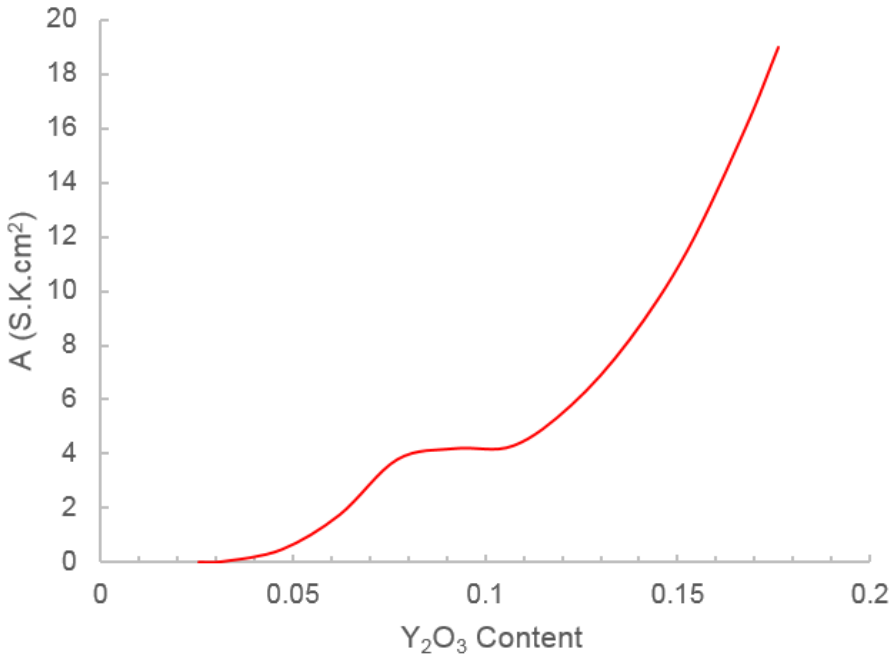

Figure 9. The pre-exponential factor (A) vs. YSZ composition at 1073K.

3.5. Conclusion

Due to the application of c-YSZ as an electrolyte in SOFCs, understanding the ionic conductivity of c-YSZ at different temperatures and compositions is important. The oxygen vacancy concentration of c-YSZ was predicted in a range of temperature and yttria concentration by applying the CALPHAD approach. The quantitative diagrams of the oxygen ion mobility versus temperature and yttria content of c-YSZ were also developed for c-YSZ single crystals. The ionic conductivity of c-YSZ single crystals in a range of temperature and yttria concentration was predicted as well. In addition, the pre-exponential factor and activation energy versus yttria concentration were calculated and discussed with respect to the trend of predicted ionic conductivity and mobility. As one of the important contributions of the current work, the conductivity of c-YSZ single crystals with low Y_2O_3 concentration was predicted, since sample preparation of c-YSZ single crystals with low

Y_2O_3 concentration is not easily feasible due to the cubic-tetragonal phase transformation. Furthermore, my predictions on c-YSZ single crystals can be treated as the baseline and can be applied in the future conductivity predictions for polycrystalline c-YSZ.

CHAPTER 4: PHASE DIAGRAM FOR NANO YTTRIA-STABILIZED ZIRCONIA SYSTEM

4.1. Introduction

As mentioned in chapter 1, Yttria-stabilized zirconia (YSZ) is one of the most interesting ceramic systems which has been studied extensively because of its critical applications. Tetragonal polymorph is used as advanced structural ceramic like tooth crowns and jet engines since it has high toughness [1-3]. Cubic polymorph has the ability of conducting oxygen ions due to the high oxygen vacancy concentration, which increases when temperature rises [2]. This characteristic of cubic polymorph is the reason of its applicability in solid oxide fuel cells (SOFCs) and oxygen sensors [4-6]. Figure 10 shows the crystal structure of YSZ polymorphs.

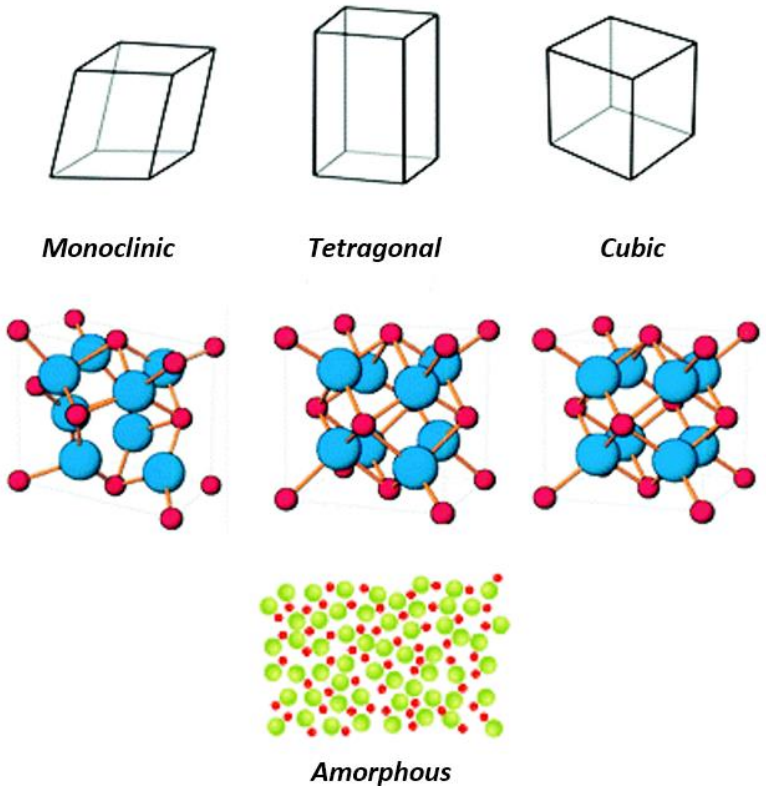

Figure 10. Crystal structures of YSZ polymorphs [71, 72].

Nano crystalline YSZ (n-YSZ) has been investigated recently because of its different properties with respect to the bulk. For example, one important factor in the gas sensors is response time which is related to electrode microstructure because of the effect of surface diffusion. Particles with smaller grain size and higher specific surface help reducing the response time. The larger surface area also causes higher catalytic activities [10]. n-YSZ properties are attributed to the large fraction of atoms within the interface region [73]. In fact, in the systems with nano sized particles, the effect of surface area becomes significant and affects the Gibbs energy of each phase [74, 75]. Therefore, n-YSZ system shows different behavior in comparison with the bulk YSZ. In other words, the stability regions in n-YSZ system can be significantly different from that of the bulk YSZ.

For the bulk YSZ system, different groups have conducted extensive studies to understand the phase regions at different temperatures and compositions [56, 76-78]. However, for n-YSZ system, there is no applicable accurate phase diagram especially at elevated temperatures.

In this chapter, the CALPHAD (Calculation of Phase Diagrams) approach was applied to predict the Gibbs energy of bulk YSZ system. By considering the effect of surface energy, the total Gibbs energy of n-YSZ system was developed. Therefore, by predicting the total Gibbs energy of each polymorph in a range of temperature, a 3-D phase diagram for n-YSZ system was established in which the stability range of each crystal structure can be determined based on the particle size, composition, and temperature.

4.2. Background review

Several groups have attempted to observe the changes in the transformation temperatures as a function of grain size for n-YSZ system [1, 2, 79, 80]. The total surface energy is

consisting of surface area and specific surface energy. Hence, to have Gibbs energy definition for n-YSZ system, the specific surface energy has to be measured. Based on the recent advancements in microcalorimetry for measuring specific surface energy of nano particles, Drazin and Castro have measured multiple specific surface energies in the n-YSZ system for yttria mole fraction of 0 to 0.2 at room temperature [81]. Water adsorption microcalorimetry theory was applied to collect the specific surface energy data [82]. The experiments were done for m-ZrO_2, t-ZrO_2, c-ZrO_2, and amorphous phases with the particle size of 32.4 to 39.8 nm, 14.2 to 17.7 nm, 4 to 6.3 nm, and 1 to 1.1 nm respectively.

4.3. Thermodynamic Modeling

4.3.1. Gibbs energy calculation for the bulk materials

The CALPHAD approach relies on modeling the Gibbs energies of each individual phases in the system. This characteristic state function is of particular interest because the Gibbs energy is minimized at equilibrium under constant temperature and pressure. Temperature and pressure are the variables that are typically controlled experimentally. The thermodynamic databases based on the Gibbs energies are then constructed using experimental data and programs like Thermo-Calc [9].

The thermodynamic database for the ZrO_2-Y_2O_3 system was provided by Chen et al. [56]. It was applied in the current study to calculate the Gibbs energy of each phase for the bulk YSZ at different temperatures. Equation below is for the Gibbs free energy of bulk materials:

$$\Delta G_{bulk} = \Delta H - T\Delta S \quad (1)$$

in which H is enthalpy, T is temperature, and S is entropy.

The model used for m-ZrO_2 (monoclinic YSZ phase) and t-ZrO_2 (tetragonal YSZ phase)

in the database by Chen et al. is $(Y^{3+},Zr^{4+})_1(O^{2-},Va)_2$ [56]. In this model, the first sublattice is occupied by Y^{3+} and Zr^{4+} ions and the second one is occupied by O^{2-} ion and vacancy. The model used for c-ZrO_2 (cubic YSZ phase) is $(Y,Y^{3+},Zr,Zr^{4+})_1(O^{2-},Va)_2$. Thus, the Gibbs energy of the m-ZrO_2 and t-ZrO_2 phases are given by:

$$G_m = y_{Y^{3+}}\, y_{O^{2-}}\, {}^{\circ}G_{Y^{3+}:O^{2-}} + y_{Zr^{4+}}\, y_{O^{2-}}\, {}^{\circ}G_{Zr^{4+}:O^{2-}} + y_{Y^{3+}}\, y_{Va}\, {}^{\circ}G_{Y^{3+}:Va} + y_{Zr^{4+}}\, y_{Va}\, {}^{\circ}G_{Zr^{4+}:Va} + RT[y_{Y^{3+}} \ln y_{Y^{3+}} + y_{Zr^{4+}} \ln y_{Zr^{4+}} + 2(y_{O^{2-}} \ln y_{O^{2-}} + y_{Va} \ln y_{Va})] + {}^{E}G_m$$

And the Gibbs energy of the c-ZrO_2 phase is given by:

$$G'_m = y_{Y^{3+}}\, y_{O^{2-}}\, {}^{\circ}G_{Y^{3+}:O^{2-}} + y_{Zr^{4+}}\, y_{O^{2-}}\, {}^{\circ}G_{Zr^{4+}:O^{2-}} + y_{Y^{3+}}\, y_{Va}\, {}^{\circ}G_{Y^{3+}:Va} + y_{Zr^{4+}}\, y_{Va}\, {}^{\circ}G_{Zr^{4+}:Va} + y_Y\, y_{O^{2-}}\, {}^{\circ}G_{Y:O^{2-}} + y_{Zr}\, y_{O^{2-}}\, {}^{\circ}G_{Zr:O^{2-}} + y_Y\, y_{Va}\, {}^{\circ}G_{Y:Va} + y_{Zr}\, y_{Va}\, {}^{\circ}G_{Zr:Va} + RT[y_Y \ln y_Y + y_{Y^{3+}} \ln y_{Y^{3+}} + y_{Zr} \ln y_{Zr} + y_{Zr^{4+}} \ln y_{Zr^{4+}} + 2(y_{O^{2-}} \ln y_{O^{2-}} + y_{Va} \ln y_{Va})] + {}^{E}G'_m$$

where y_j is site fraction of specie j in a particular sublattice. The excess Gibbs energy ${}^{E}G_m$ is defined as below:

$${}^{E}G_m = y_{Y^{3+}}\, y_{Zr^{4+}}\, y_{O^{2-}} \sum_{i=0}^{n} {}^{i}L_{Y^{3+},\,Zr^{4+}:O^{2-}} (y_{Y^{3+}} - y_{Zr^{4+}})^i + y_{Y^{3+}}\, y_{Zr^{4+}}\, y_{Va} \sum_{i=0}^{n} {}^{i}L_{Y^{3+},\,Zr^{4+}:Va} (y_{Y^{3+}} - y_{Zr^{4+}})^i$$

And the excess Gibbs energy ${}^{E}G'_m$ is defined as below:

$${}^{E}G'_m = y_{Y^{3+}}\, y_{Zr^{4+}}\, y_{O^{2-}} \sum_{i=0}^{n} {}^{i}L_{Y^{3+},\,Zr^{4+}:O^{2-}} (y_{Y^{3+}} - y_{Zr^{4+}})^i + y_{Y^{3+}}\, y_{Zr^{4+}}\, y_{Va} \sum_{i=0}^{n} {}^{i}L_{Y^{3+},\,Zr^{4+}:Va} (y_{Y^{3+}} - y_{Zr^{4+}})^i + y_{Zr}\, y_{Zr^{4+}}\, y_{O^{2-}} \sum_{i=0}^{n} {}^{i}L_{Zr,\,Zr^{4+}:O^{2-}} (y_{Zr} - y_{Zr^{4+}})^i + y_{Zr}\, y_{Zr^{4+}}\, y_{Va} \sum_{i=0}^{n} {}^{i}L_{Zr,\,Zr^{4+}:Va} (y_{Zr} - y_{Zr^{4+}})^i$$

where ${}^{i}L$ is the interaction parameter with the form of A+BT. If i=0, the solution is regular, if i=1, the solution is sub-regular, and if i=2, the solution is sub-sub-regular.

The interaction parameter for m-ZrO_2 phase was considered zero by Chen et al. [56] since yttria concentration in m-ZrO_2 is extremely low. t-ZrO_2 phase was considered as a regular solution and c-ZrO_2 phase was treated as a sub-regular solution in their database.

4.3.2. T-zero temperature method to determine phase boundaries

In order to calculate the Gibbs energy for bulk YSZ, partial equilibria simulation has been applied. Since the kinetics is very slow in the YSZ system, phase transitions are observed with a considerable delay. The m-ZrO_2↔t-ZrO_2 transition occurs as a martensitic transformation [56]. In order to determine the phase boundaries under such conditions, Kaufman and Cohen suggested T-zero temperature approach [83], which is one type of the partial equilibrium method. In this method, the starting transition temperature of tetragonal to monoclinic phases during cooling and also the starting transition temperature of monoclinic to tetragonal phases during heating are captured. Based on these two transition temperatures, an average temperature is calculated as the equilibrium temperature. In other words, T_0 is a temperature in which the Gibbs energies of two adjacent phases are equal in a determined composition. T_0 temperature is located in the two-phase region and it is a theoretical limit for a diffusionless transformation as illustrated in Figure 11. In this figure, u_j is defined as the site fraction of element j with reference to the substitutional sublattices only.

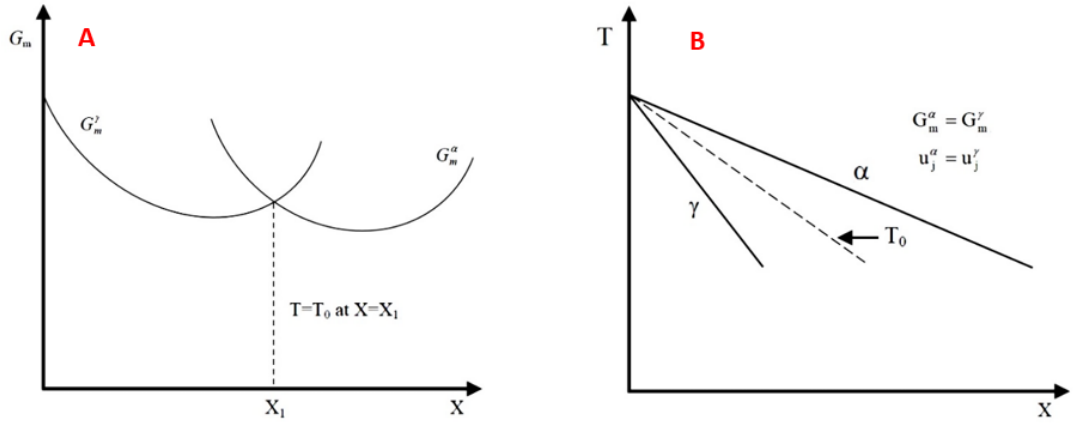

Figure 11. T-zero temperature method. A) T_0 temperature as a point at a defined composition, B) T_0 temperature as a line when the composition changes.

4.3.3. Amorphous phase modeling

The model for ionic liquid was used to calculate the amorphous phase. In the thermodynamic database by Chen et al., the liquid phase was modeled as $(Y^{3+},Zr^{4+})_p(O^{2-})_q$, in which $p = 2y_{O^{2-}}$ and $q = 3y_{Y^{3+}} + 4y_{Zr^{4+}}$ [56]. The Gibbs energy description of liquid is given by:

$$G^L_m = y_Y{}^{3+}\, y_O{}^{2-} {}^{\circ}G^L_{Y^{3+}:O^{2-}} + y_Zr{}^{4+}\, y_O{}^{2-} {}^{\circ}G^L_{Zr^{4+}:O^{2-}} + pRT[y_Y{}^{3+} \ln y_Y{}^{3+} + y_Zr{}^{4+} \ln y_Zr{}^{4+}] + {}^{E}G^L_m$$

The excess Gibbs energy ${}^{E}G^L_m$ is defined as below:

$${}^{E}G^L_m = y_Y{}^{3+}\, y_Zr{}^{4+}\, y_O{}^{2-} \sum_{i=0}^{n} {}^{i}L_{Y^{3+},Zr^{4+}:O^{2-}} (y_Y{}^{3+} - y_Zr{}^{4+})^i$$

The ionic liquid was considered as sub-sub-regular solution (i=2) in the database by Chen et al. [56].

Generally, the liquid phase is stable at high temperatures. In order to model an amorphous phase in the CALPHAD approach, one method is to extrapolate the liquid model to lower temperatures. In fact, the amorphous phase is considered as a supercooled liquid. Although the structure and physical state of supercooled liquid is different from amorphous phase and some minor errors are expected in this simulation, but they are still very similar and the results are close to reality.

4.3.4. Gibbs energy calculation for nano particles

The surface area becomes significant and plays an effective role in the Gibbs energy in nano particles. Consequently, the Gibbs energy equation will be as shown below for nano particles:

$$\Delta G_{total} = \Delta G_{bulk} + \gamma A = \Delta H_{bulk} - T\Delta S_{bulk} + \gamma A \qquad (2)$$

in which γ is specific surface energy and A is surface area of the nano particles. Therefore, in order to calculate the total Gibbs energy for nano particles, specific surface energy of

each phase and the surface area are needed. The experimental data for the specific surface energy of n-YSZ polymorphs provided by Drazin and Castro [81] at room temperature were applied in this study to calculate surface energy. The particles were also assumed to be spherical to enhance surface area calculation.

4.4. Results and discussion

Figure 12 shows the calculated Gibbs energy of bulk YSZ vs. composition (mole fraction of Y_2O_3) for the four phases i.e. monoclinic, tetragonal, cubic, and amorphous (supercooled liquid), at room temperature. The yttria mole fraction is between 0 and 0.2 since the zirconia rich side has important applications as mentioned in section 1.

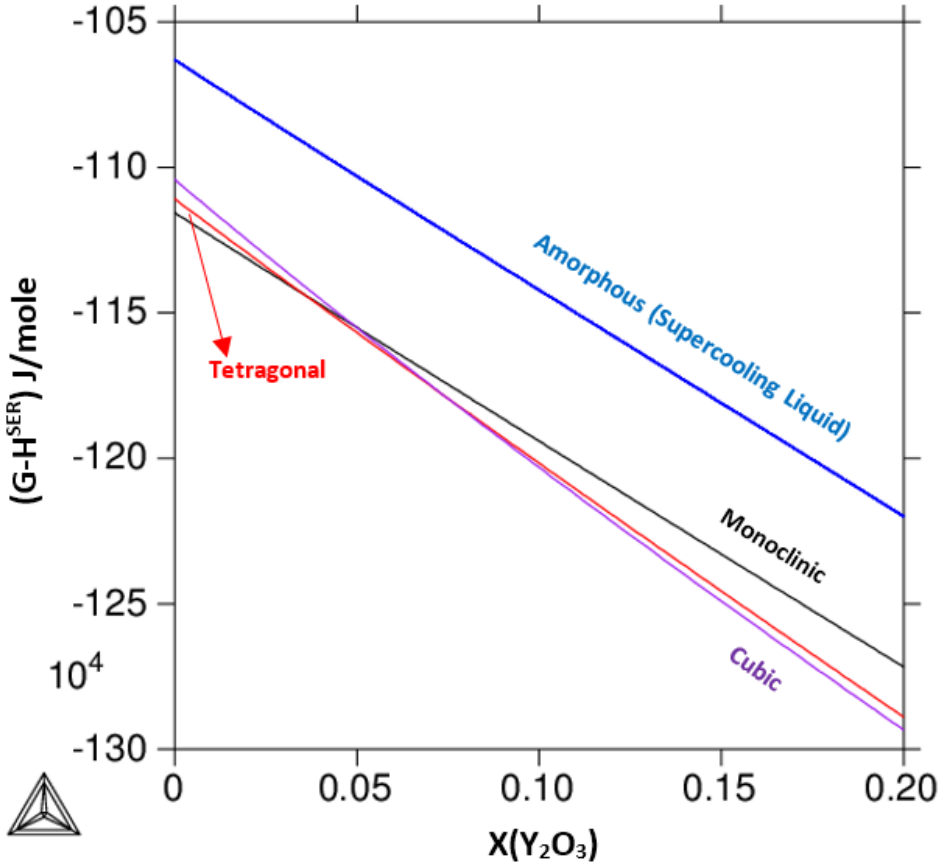

Figure 12. The Gibbs energy of monoclinic, tetragonal, cubic, and amorphous (supercooling liquid) phases vs. yttria mole fraction at room temperature for the bulk YSZ.

Based on the experimental results followed by statistical analyses, the equations below from Drazin and Castro represent the specific surface energy of each n-YSZ polymorph [81]:

$$\gamma_m = (1.9278)-(9.68)x \quad (3)$$

$$\gamma_t = (1.565)-(4.61)x \quad (4)$$

$$\gamma_c = (1.1756)-(3.36)x+(7.77)x^2 \quad (5)$$

$$\gamma_a = (0.8174)-(0.11)x \quad (6)$$

In all these equations, x is the yttria mole fraction and γ_m, γ_t, γ_c, and γ_a are specific surface energies of monoclinic, tetragonal, cubic, and amorphous phases, respectively.

For solids, the specific surface energy depends on the particle size ($d\gamma/dA \neq 0$) [84] in addition to the composition. However, for the particles with radii greater than the critical radius ($R \geq R_c$), the specific surface energy is constant at a determined temperature and does not change with particle size [85]. Based on the results of previous studies on the molecular systems, R_c is between 0.5 and 1 nm [85], which is less than almost the whole particle size range studied in the current work. Therefore, the specific surface energies are dependent only on the yttria mole fraction in this study as it is indicated in the equations 3, 4, 5, and 6.

The total Gibbs energy of n-YSZ system is predicted as shown in Figure 13 for particle size (the spherical particle diameter) of 0.1 nm, 1 nm, 10 nm, and 100 nm at room temperature.

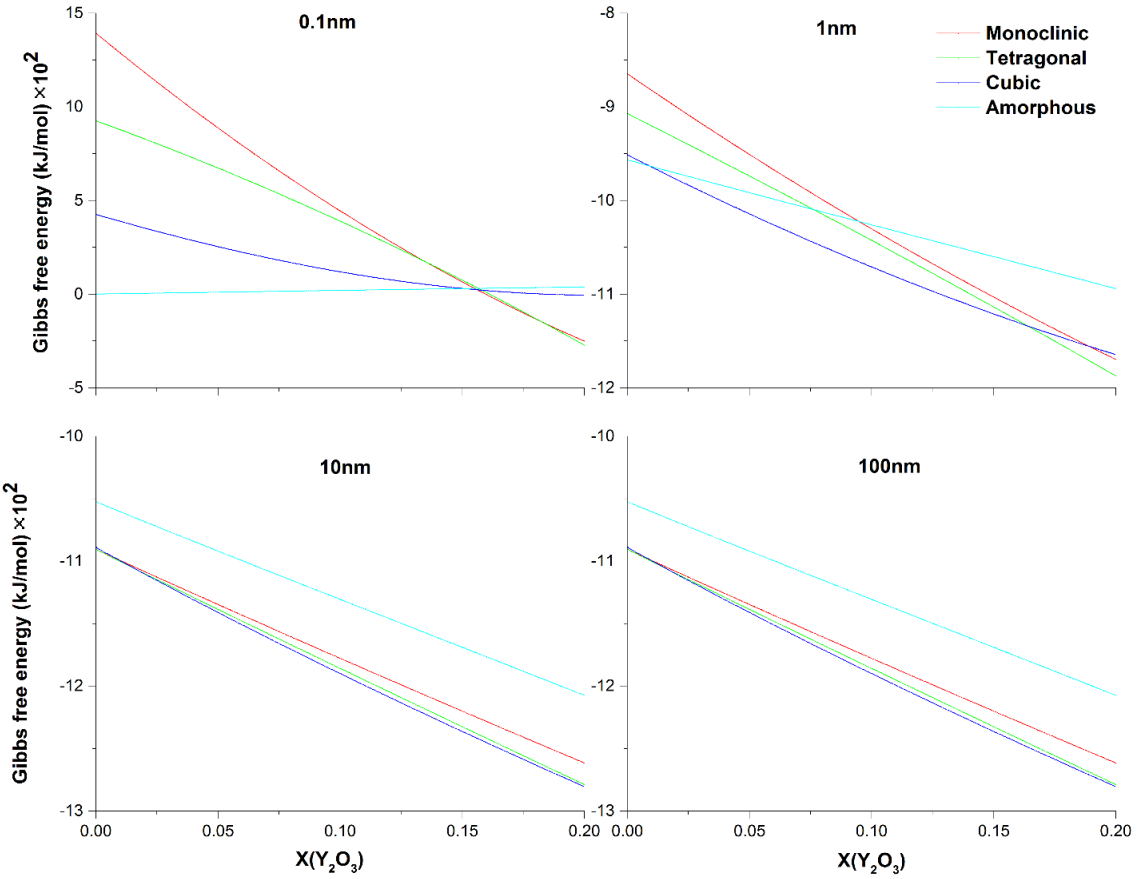

Figure 13. The Gibbs energy vs. yttria mole fraction at room temperature for n-YSZ with different particle sizes.

As it is shown in Figure 13, the intersection between Gibbs energy of different phases is changing with particle size. When the particle size is 10 or 100 nm, amorphous phase is not stable. If the particle size decreases to 1 nm, the amorphous phase starts to be stable and its stability composition range increases by decreasing the particle size (Figure 13). As the stability of each phase is determined by the Gibbs energy of that phase, for a specific phase to be stable, its Gibbs energy needs to be less than that of the other involved phases. The Gibbs energy of amorphous phase is less than cubic, tetragonal, and monoclinic phases only when the size of particles are very small. When the particle size decreases, the effect of surface energy increases which causes the Gibbs energy of all involved phases to be

changed and leads to stability of amorphous phase rather than cubic, tetragonal and monoclinic phases.

The intersection points indicate that the Gibbs energies of the two phases related to each intersecting curve are equal at a certain composition. These intersection points for each two adjacent phases represent T_0 temperature line which was discussed in section 3.2. Using T-zero method, n-YSZ phase diagram at room temperature was plotted as indicated in Figure 14. In this figure, each curve indicates the boundary between phases by which the stability range of each polymorph vs. particle size and composition (mole fraction of Y_2O_3) is detected at room temperature. The Y axis in Figure 14 is in logarithmic scale.

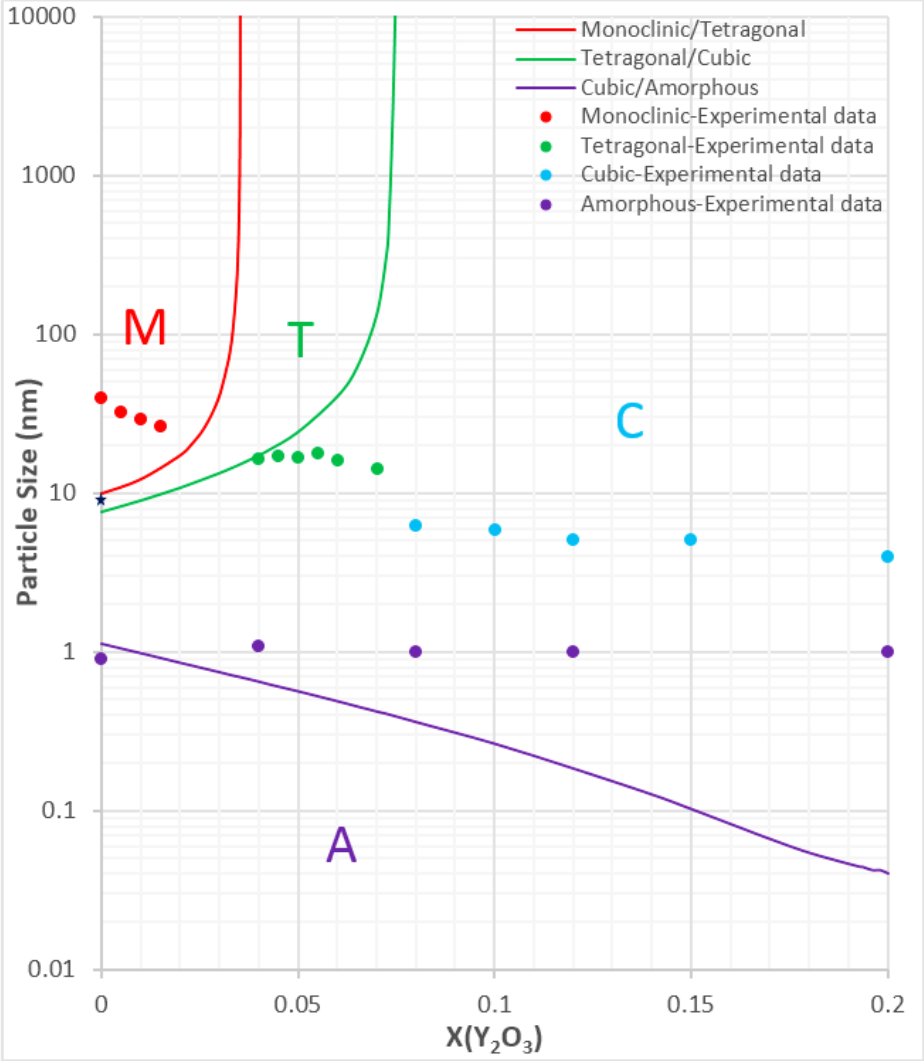

Figure 14. The phase diagram for n-YSZ system at room temperature in comparison with the experimental data which represent experimentally measured crystal structure by Drazin and Castro [17]. ★ sign indicates the largest tetragonal pure zirconia particle size experimentally observed [17]. (M: Monoclinic, T: Tetragonal, C: Cubic, A: Amorphous)

The largest tetragonal pure zirconia particle size experimentally observed was around 9 nm [81] which is compatible with the diagram in Figure 14. Due to simplifications as discussed in section 3.3, the errors are expected for the amorphous phase in the current study. However, the results for amorphous phase clearly indicate the ability of predicting the amorphous stability range by the CALPHAD approach along with its critical role to predict the Gibbs energy of other phases. The discrepancy between tetragonal phase region and

the related superimposed experimental data shown in Figure 14 can be an indication that the thermodynamic database for bulk YSZ provided by Chen et al. [56] needs to be improved in tetragonal+cubic/cubic phase boundary. It is found there were no experimental data for the T'_0 line shown in Figure 16 at the time of thermodynamic database assessment, while enough experimental data were available for T_0 temperature line [56]. Then, it is highly possible that the T'_0 line is not accurate and needs to be shifted toward right side of the graph which will then provide better agreement between tetragonal/cubic (T/C) curve and related experimental data.

It is worth noting that in Figure 14, the role of bulk Gibbs energy is of great importance. The phase stability regions will greatly change if the bulk Gibbs energy is not calculated correctly. For example, the $\Delta H_{M/T}$ and $\Delta H_{T/C}$ calculated with oxide melt drop solution calorimetry method by Drazin and Castro are 10.304 and 13.351 (kJ/mol) respectively [81], while $\Delta H_{M/T}$ and $\Delta H_{T/C}$ is 6 and 7.5 (kJ/mol) respectively based on the thermodynamic database from Chen et al. by the CALPHAD approach [56]. It is highly possible these large differences are due to the stability state of the samples which experimentally investigated. If the examining sample does not reach the final equilibrium, which is highly possible in YSZ system due to its extremely slow kinetics, the measured enthalpy of this sample will be different with that of the same sample in its final equilibrium state.

Since the CALPHAD approach was applied in this study, the Gibbs energy of bulk YSZ is predictable in a wide range of temperature. Therefore, the Gibbs energy of bulk YSZ for each phase was predicted with the CALPHAD approach at different temperatures between 25 to 500˚C. By considering the effect of surface energy, the n-YSZ phase diagram at various temperatures is predicted as shown in Figure 15. The specific surface energy of a

crystal structure depends on the temperature [86]. Accordingly, the specific surface energy at a determined particle size and composition will change with temperature. In this study, the changes of specific surface energy by increasing the temperature up to 500˚C was assumed to be small and negligible.

Comparing the four diagrams in Figure 15, the c-ZrO_2 region is enlarged with the increase of temperature. The stability range of m-ZrO_2 shrinks and the T/C curve shifts toward left side of the graph and also moves up when temperature increases. The changes in stability range of phases with temperature clearly show how the crystal structure and as a result, material properties change. For example, based on Figure 15, a 10n-0.01YSZ system (YSZ with yttria mole fraction of 0.01 and particle size of 10 nm) is tetragonal at room temperature which changes to cubic at temperatures around 500˚C. This phase transition can affect the material properties which is directly linked to the crystal structure.

One may argue that a phase diagram for nano particles at high temperatures is not applicable because nano particles will encounter coarsening at high temperatures. However, the phase diagram for nano particles can clearly reveal the effect of temperature increase and coarsening on the phase transition.

Interestingly according to Figure 15, the cubic/amorphous (C/A) curve is predicted not to change considerably by increasing temperature. This prediction is due to the effect of surface energy which is greatly dominant rather than the bulk Gibbs energy since the particle size in the amorphous region is extremely small (Eq. 2). Since the specific surface energy was assumed to be constant with temperature changes, the surface energy does not change with temperature and this causes the C/A curve be approximately fixed with temperature changes.

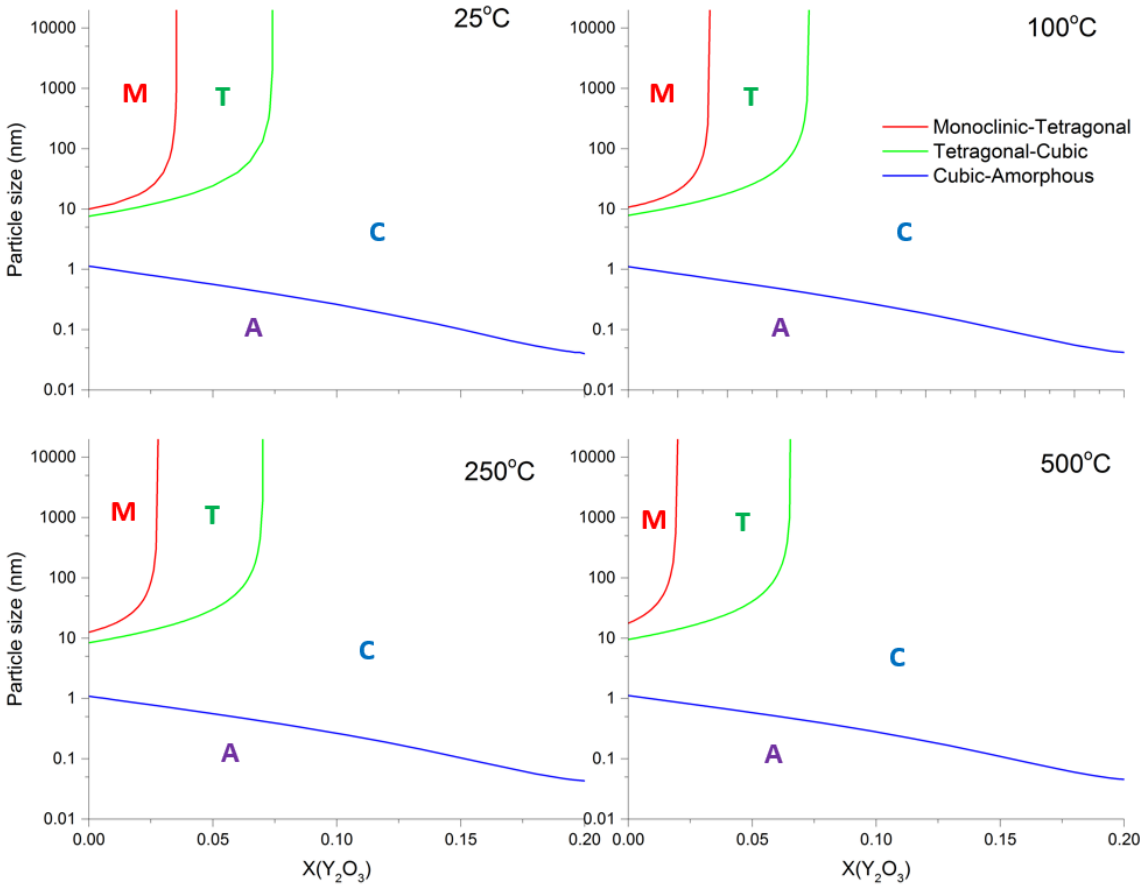

Figure 15. The phase diagram for n-YSZ system at 25, 100, 250, and 500˚C. (M: Monoclinic, T: Tetragonal, C: Cubic, A: Amorphous)

The shift of T/C curve vs. temperature is less than that of monoclinic/tetragonal (M/T) curve as can be seen in Figure 15. According to Figure 16, in the temperature range of 25 to 500˚C, the slope of T'_0 line is sharper than that of T_0 temperature line. This slope difference is the reason for milder shift of T/C curve rather than M/T curve vs. temperature changes. As an example of the shifting amount of each curve vs. temperature, Figure 17 shows the shifting behavior of M/T, T/C, and C/A curves when temperature increases for n-0. 01YSZ.

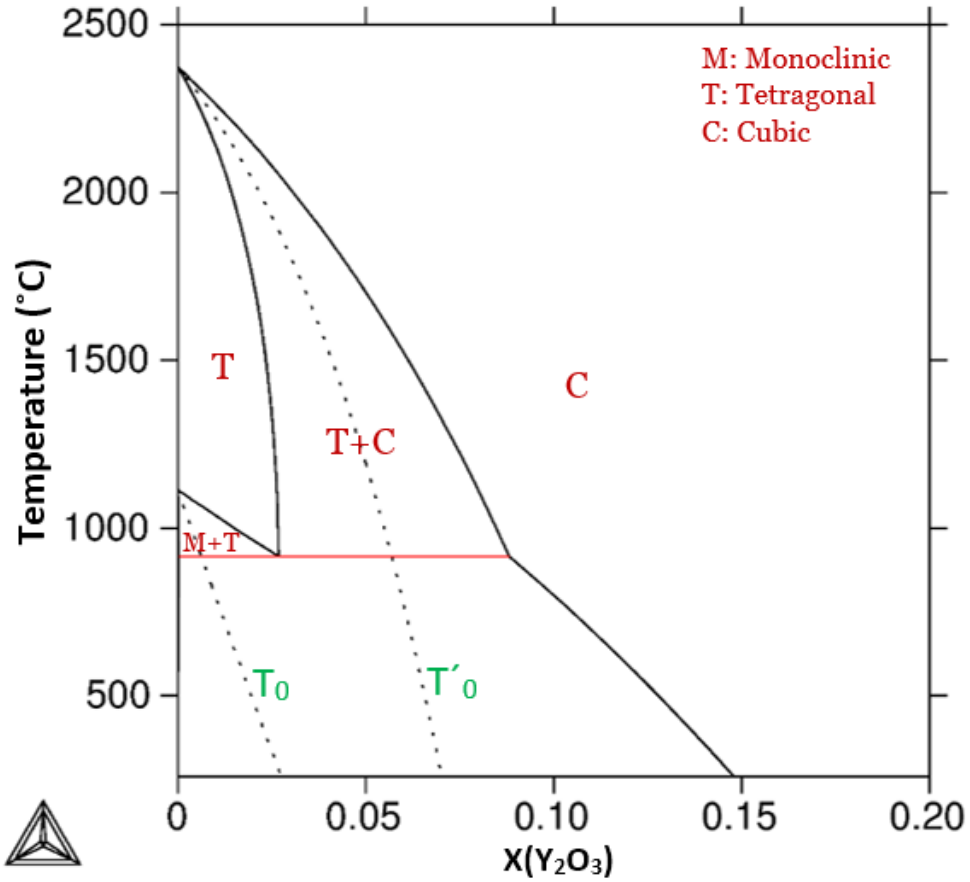

Figure 16. T_0 and T'_0 temperature lines related to bulk YSZ. (T_0 is M/T T-zero temperature line and T'_0 is T/C T-zero temperature line).

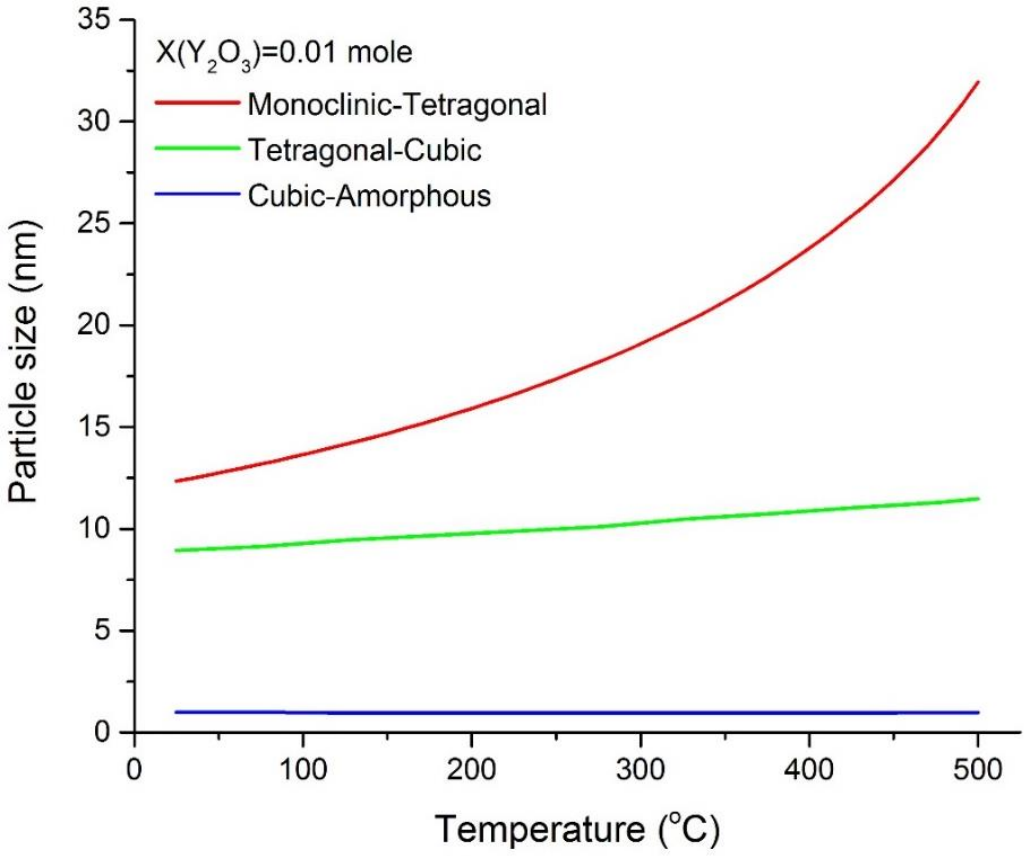

Figure 17. The changes of particle size vs. temperature for each boundary curve of n-0. 01YSZ (Nano YSZ with 0. 01 mole fraction of Y_2O_3).

By combining the phase diagrams at different temperatures, a 3-D phase diagram was achieved in which the phase regions are predicted based on the particle size, mole fraction of yttria and temperature. Figure 18 indicates the 3-D phase diagram for n-YSZ system from different angles.

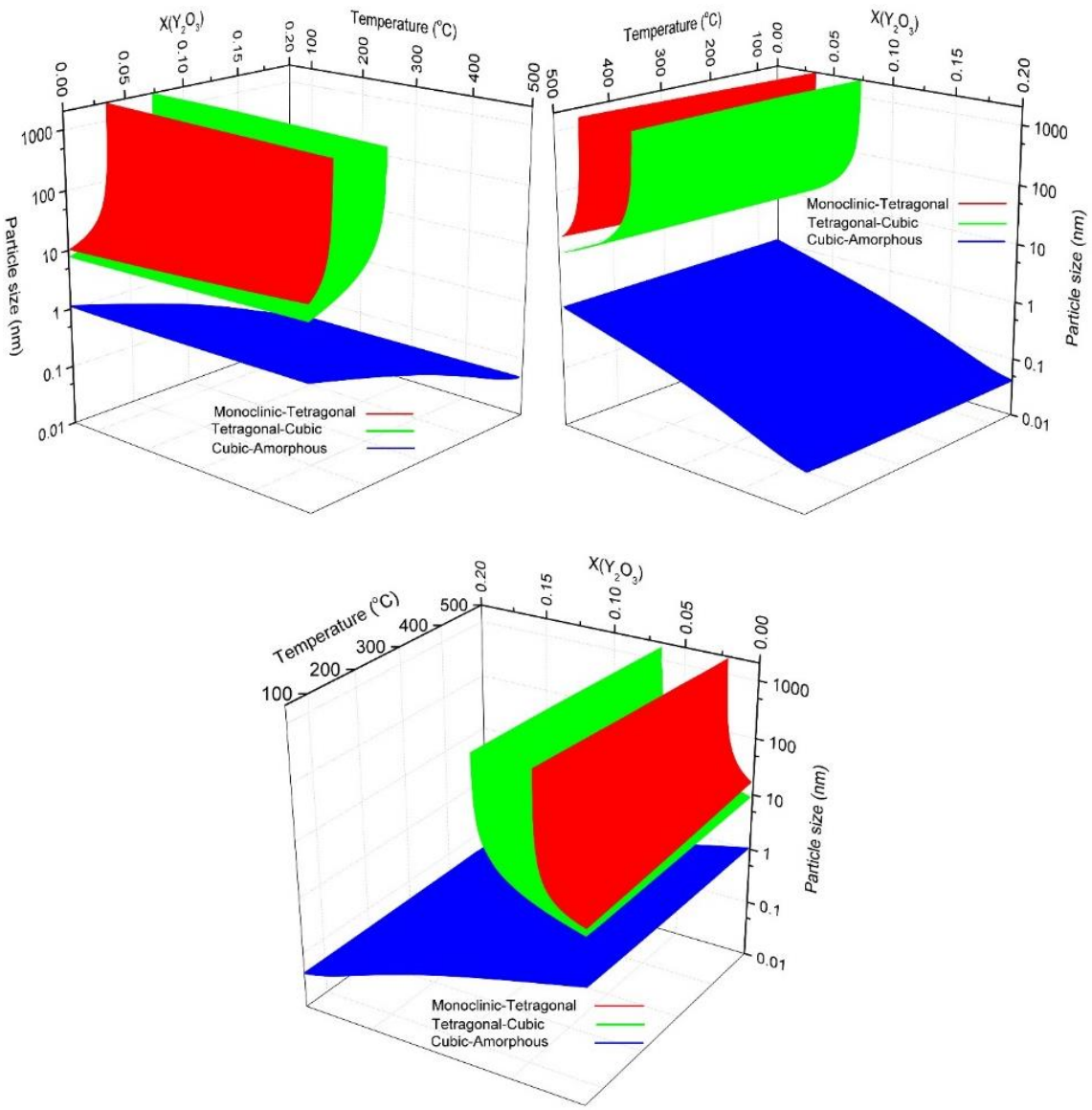

Figure 18. The 3-D phase diagram for n-YSZ system from different angles.

4.5. Conclusion

The phase diagram for n-YSZ system at room temperature was developed with the bulk Gibbs energies from the CALPHAD approach and specific surface energies of each crystal structure. By the advantage of the CALPHAD approach characteristics, the total Gibbs energy of n-YSZ system at higher temperatures was predicted and the 3-D diagram for zirconia rich side was developed at temperatures up to 500˚C for the first time, by which

the stability range of each phase in n-YSZ system is predicted based on particle size, composition, and temperature. Based on the 3-D diagram, the c-ZrO_2 and t-ZrO_2 regions become more stable and wider when temperature increases while the m-ZrO_2 region shrinks. It was shown that the CALPHAD approach plays a pivotal role to design a predictive phase diagram for nano particles. It was indicated that the CALPHAD approach is capable to be used for predicting the Gibbs energy of amorphous phases by considering few assumptions.

CHAPTER 5: RE-EVALUATION OF THE THERMODYNAMIC EQUILIBRIA ON THE ZIRCONIA-RICH SIDE OF THE ZRO_2-$YO_{1.5}$ SYSTEM

5.1. Introduction

Because of the disruptive monoclinic-tetragonal phase transformation in the pure zirconia (ZrO_2), it has limited applications [22]. Pure ZrO_2 undergoes a phase transformation from monoclinic, which is stable at room temperature, to tetragonal at about 1170˚C and then to cubic at about 2370˚C [23-25]. During monoclinic-tetragonal phase transformation in pure ZrO_2, a large volume change happens [22, 24], which can cause cracks in the sample. In addition, cubic phase in pure ZrO_2 is only stable at very high temperatures [24], which restricts its applications. However, Ruff and Ebert [26] found that the phase transformations in the pure ZrO_2 can be suppressed by doping the specific concentrations of MgO, CaO, Sc_2O_3, Y_2O_3, or CeO_2 into the pure ZrO_2. Therefore, a metastable tetragonal or cubic solid solution can be achieved at low temperatures, which makes their various applications possible. Among the abovementioned dopants to stabilize ZrO_2, Y_2O_3 is of particular interest, due to the specific properties of ZrO_2-Y_2O_3 (YSZ) system [32]. When the appropriate amount of Y_2O_3 is applied to dope ZrO_2, fully stabilized zirconia (FSZ) with cubic fluorite structure is produced. If the ZrO_2 is doped with the smaller concentrations of Y_2O_3, partially stabilized zirconia (PSZ) with tetragonal structure is produced. Tetragonal polymorph is considered as advanced structural ceramic due to its high toughness, high melting point, low thermal conductivity, and high chemical stability [1-3, 27, 28]. Cubic fluorite polymorph is applied in oxygen sensors and solid oxide fuel cells (SOFCs) as an electrolyte due to its high ionic conductivity [4-6, 29-31].

Because of critical applications of YSZ system, understanding the phase regions, especially

the ones on the ZrO_2-rich side of the system, at different temperatures and compositions and also knowing the exact temperature and composition at which the phase transformation happens are of special importance. Extensive studies have been carried out to understand the YSZ system phase equilibria and develop a precise phase diagram for this system [34, 35, 56, 76-78, 87-90]. However, there are still various contradictions and discrepancies in the phase diagram of this system [77, 87, 88, 91-102]. In other words, the behavior of phases, particularly on the ZrO_2-rich side of the system, has become a mystery. Yashima et al. [25] evaluated several versions of ZrO_2-rich side of the YSZ phase diagram proposed by different researchers. It was claimed that the tetragonal/tetragonal+cubic and tetragonal+cubic/cubic phase boundaries should be significantly different from the traditional understanding. More importantly, in a nano-YSZ phase diagram developed in 2016 [16], clear discrepancies were observed between the calculated tetragonal/cubic phase boundary and the superimposed experimental data, which echoed the conclusion from Yashima et al. [25] that the previous understandings (both modeling and experiments) on the ZrO_2-rich side are incompatible with the real conditions. Therefore, the thermodynamic re-evaluation of the ZrO_2-Y_2O_3 system is critically necessary in order to clarify the dominant thermodynamic equilibria in the ZrO_2-rich side, which would provide reliable guidance for their aforementioned critical applications.

In this paper, the experimental phase equilibria and thermodynamic data related to the YSZ system were collected and evaluated carefully. The most accurate ones based on the procedure of experiment and results interpretation were then selected to be applied in the optimization of Gibbs energy definition of each phase. The database re-assessment was carried out by the CALPHAD (CALculation of PHAse Diagrams) approach, in which both

phase equilibria and thermodynamic data are assessed together to obtain the Gibbs energy definition of a phase. The Optimization process was carried out by the PARROT module of Thermo-Calc® [103], a program developed by KTH royal institute of technology [9]. In this study, discussions are performed on ZrO_2-$YO_{1.5}$ system in order to direct comparison of obtained results with the previously published data.

5.2. The recent discovery from the nano-YSZ phase diagram

In chapter 4, the CALPHAD approach along with the thermodynamic database by Chen et al. [56] was applied to predict the Gibbs energy of the bulk ZrO_2-rich phases of the YSZ system. The surface energy of the nano particles of each phase was then added to the predicted bulk Gibbs energy to develop the total Gibbs energy of nano-YSZ system. In the developed nano-YSZ phase diagram, the points at which the Gibbs energies of two adjacent phases are equal were collected to plot the curves (T_0 lines) as the boundaries between monoclinic zirconia (m-ZrO_2), tetragonal zirconia (t-ZrO_2), cubic zirconia (c-ZrO_2), and amorphous phases. The calculated boundary between m-ZrO_2 and t-ZrO_2 phases showed good agreement with the experimental observations. It was discussed that the boundary between c-ZrO_2 and amorphous phases was also acceptable due to assumptions and simplifications made during modeling. However, considerable discrepancy was observed between the calculated t-ZrO_2/c-ZrO_2 phase boundary and the superimposed experimental data. The authors discussed that the discrepancy is related to the bulk YSZ database and suggested re-assessment of this database, specifically at the ZrO_2-rich side of the YSZ system.

5.3. Experimental data in the ZrO_2-$YO_{1.5}$ system

The ZrO_2-$YO_{1.5}$ quasi-binary system has been extensively studied experimentally [56, 76-

78, 87, 91, 104, 105]. At the ZrO_2-rich side, m-ZrO_2, t-ZrO_2, and c-ZrO_2 phases are stable. One intermediary phase, $Zr_3Y_4O_{12}$, has been confirmed with an ordered fluorite structure. A stoichiometric phase, i.e. $Zr_4Y_2O_{11}$, has also been reported by ab initio calculations at about 19.7 mole% $YO_{1.5}$ that has not been observed experimentally [106]. The $YO_{1.5}$-rich side of the system consists of α-Y_2O_3 and β-Y_2O_3 phases. Rühle et al. [107] and Sakuma [108] studied the equilibrium and metastable phase transformations in ZrO_2-rich side of YSZ system. Also Stubican et al. [89], Yagi et al. [109], and Yoshikawa et al. [110] tried to capture the phase boundaries between cubic and tetragonal regions. It was reported that below about 4 mole% $YO_{1.5}$, t-ZrO_2 transforms to m-ZrO_2 on cooling and reverse transformation on heating, both martensitically with a hysteresis. It was also reported that in the range of 4 to 13 mole% $YO_{1.5}$, a quickly cooled c-ZrO_2 transforms to a metastable t-ZrO_2, which is usually called t′-ZrO_2. By increasing the $YO_{1.5}$ content, the tetragonality was reported to be decreased, which leads to a metastable t-ZrO_2 phase with cubic lattice parameters and tetragonal symmetry, called t′′-ZrO_2. It was suggested that the c-ZrO_2 with more than 15 mole% $YO_{1.5}$ is stabilized and does not transform to other phases. $Zr_3Y_4O_{12}$ was reported by Ray and Stubican [111] and Scott [88], and later, Pascual and Duran [87], Stubican et al. [89], and Jayaratna et al. [112] confirmed its existence. Pascual and Duran [87] by using XRD, and Suzuki and Kohzaki [33, 35] by applying electrical conductivity measurement determined the phase boundaries of c-ZrO_2+$Zr_3Y_4O_{12}$ two-phase region. The boundaries of c-ZrO_2+α-Y_2O_3 and $Zr_3Y_4O_{12}$+α-Y_2O_3 two-phase regions were also determined by several groups [5, 87-89, 112-116]. The eutectoid and melting reactions were evaluated by Srivastava et al. [114], Pascual and Duran [87], Srikanth and Subbarao [117], Stubican et al. [89], Rouanet [118], and many others [35, 105, 119, 120].

5.4. Thermodynamics and kinetics of ZrO_2-rich side and experimental data evaluation

Numerous experimental studies have been carried out on the thermodynamic equilibria of the ZrO_2-rich side of YSZ system. However, significant discrepancies have been observed between the experimental results of various groups, as mentioned before. In this regard, Yashima et al. [25] have carried out a comprehensive literature review of the available experimental data and pointed out the sluggish kinetics of ZrO_2-rich side of the YSZ system. They discussed the martensitic and massive transformations that might happen in this system. The authors also compared different phase diagrams of ZrO_2-rich side of the YSZ system plotted by various researchers and discussed the differences between them. They mentioned that the most experimental results were interpreted inaccurately, specifically at low temperatures. The inaccurate interpretations of the experimental data led to the imprecise YSZ phase diagrams, which are not able to determine the phase regions properly.

According to Yashima et al. [25], the equilibrium phase boundaries can be established only above about 1200˚C by the conventional heat treatments because of slow diffusion of cations below this temperature. For example, at the temperature of 1100˚C, cations need about 70 years to diffuse 3 μm [25]. Therefore, metastable states are usual in the phases of the ZrO_2-rich side due to sluggish kinetics in addition to the diffusionless phase transformations, which make the structural changes of the system complicated. The thermal history, grain size, and particle size of the material can strongly affect the phase transformations in this area [107, 108, 121, 122].

The equilibrium phase boundaries of ZrO_2-rich side of the ZrO_2-$YO_{1.5}$ system have been investigated extensively [25, 87, 88, 91, 94, 95, 104, 107, 109, 112-114, 118, 123-130]. According to the sluggish kinetics, it is critical to set up the experiments wisely and carefully, especially at low temperatures, and choose the proper techniques for heat treatments. Therefore, the experimental results must be selected based on the accuracy of the process of experiment, appropriateness of the type of applied technique, and the results interpretation. Following these criteria carefully can lead to a precise and reliable thermodynamic database. Thus, the reliable experimental data along with the discussions on the evaluation process are presented in continue.

Due to the low cation mobility in ZrO_2-rich side of the system, it is expected that the phase transformations are detected with hysteresis during the experiments. This means during the heating and cooling experiments, the phase transformation temperatures are captured with a delay, i.e. the real phase transformation temperature would be lower in the heating experiment and higher in the cooling experiment than what is being captured. The aforementioned hysteresis becomes more at lower temperatures.

According to the abovementioned explanations regarding the very slow kinetics at low temperatures (below 1200˚C), the experimental data were categorized based on the temperature range, in which the experiment has been performed. At low temperatures, it is required to apply the experimental techniques by which the diffusion is accelerated. A suggested method to accelerate the diffusion is using a solvent along with YSZ sample [89, 131-135]. However, it is important that the solvent does not change the final product. Therefore, the experimental data at low temperatures, which were obtained by traditional heat treatments, were not considered in this work. Instead, the data by Stubican et al. [89]

and Nakamura et al. [127] obtained under hydrothermal conditions were utilized since this technique can accelerate the kinetics at low temperatures [25].

At high temperatures (higher than 1200˚C), it is important to consider the experimental data with accurate heat treatment procedure. For example, the XRD results on a quenched YSZ sample at room temperature can give the spectrum of m´-ZrO_2, t´-ZrO_2, or t´´-ZrO_2 metastable phases, which misleads the interpretation of the m-ZrO_2+t-ZrO_2/t-ZrO_2 or t-ZrO_2+c-ZrO_2/c-ZrO_2 phase boundaries. Hence, giving enough time to the sample to reach equilibrium during heat treatment is of great importance and applying in situ characterizations are preferred. Otherwise, it is highly possible to interpret the phase boundaries incorrectly, especially at lower temperatures.

At 1995, Suzuki studied the phase transition of cubic YSZ containing 15 to 60 mole% $YO_{1.5}$ by analyzing the electrical conductance data [35]. In order to enhance equilibrium during the cooling process, Suzuki employed 10˚C and half an hour intervals at high temperatures, while the temperature intervals decreased and time intervals increased by reducing the temperature [35]. Suzuki [34] also studied the phase transition of YSZ solid solutions with the $YO_{1.5}$ content of 4.7 to 11 mole% by the method of conductivity measurement, in which a special cooling schedule similar to the abovementioned one was applied. Suzuki and Kohzaki [33] at 1993 studied the electrical conduction changes of YSZ with 18 and 46 mole% $YO_{1.5}$ and correlated the results to the phase transformation.

Scott [88] employed XRD at room temperature to determine the crystal structure of prepared YSZ samples containing 3 to about 25 mole% $YO_{1.5}$. Cautious heat treatment was applied to ensure obtaining the equilibrium state of the phases during sample preparation. The synthesized samples were heat-treated for four weeks at 1400˚C, one week at 1600˚C,

two days at 1700˚C, and 2 hours at 2000˚C. The heat-treated samples were then quenched to freeze the equilibrium state in order to perform the XRD analysis at ambient temperature. Although the cooling rate was reported to be very fast (1000˚C/s at high temperatures and 100˚C/s at lower temperatures), the author was still aware and mentioned about the possible diffusionless phase transformations during quenching process.

Stubican et al. [89] studied the c-ZrO_2 phase transformation by applying the high temperature XRD. Annealing time of up to 24 weeks was used to reach equilibrium state. Jayaratna et al. [112] reported that the lower limits of c-ZrO_2 were found to be 16, 14, and 12.5 mole% of $YO_{1.5}$ at 1300, 1450, and 1600˚C, respectively. However, it should be mentioned that the annealing times were relatively short, which may cause the samples not to reach equilibrium state.

5.5. Thermodynamic Modeling

The CALPHAD approach is based on the modeling of the Gibbs energies of individual phases in the system. The phase equilibria data and thermochemical data are usually combined together to construct the Gibbs energies. This characteristic state function is of particular importance because under constant temperature and pressure, the Gibbs energy is minimized at equilibrium. The two variables of temperature and pressure are typically controlled in the experiments. The thermodynamic databases based on the Gibbs energies are then constructed using experimental data and software programs [9, 13].

In the current work, the phase models used by Chen et al. [56] were utilized. Based on that, the two solid solutions including m-ZrO_2 and t-ZrO_2 are modeled by $(Y^{3+},Zr^{4+})_1(O^{2-},Va)_2$ and the other two solid solutions including c-ZrO_2 and β-Y_2O_3 are modeled by $(Y,Y^{3+},Zr,Zr^{4+})_1(O^{2-},Va)_2$. In these models, the first sublattice is occupied by Y^{3+} and Zr^{4+}

ions and the second one is occupied by O^{2-} ion and vacancy. The presence of Y and Zr elements in the model of c-ZrO_2 and β-Y_2O_3 is due to considering the possible ionization or recombination at extreme conditions. Therefore, the models are mainly controlled by the ions along with vacancy at the regular conditions. The α-Y_2O_3 is modeled by $(Y,Y^{3+},Zr^{4+})_2(O^{2-},Va)_3(O^{2-},Va)_1$, in which three sublattices have been considered.

According to the chosen model for each solid solution, the Gibbs energy of the m-ZrO_2 and t-ZrO_2 phases are given by Eq. 1,

$$G_m = y_{Y^{3+}}\, y_{O^{2-}}\, {}^{\circ}G_{Y^{3+}:O^{2-}} + y_{Zr^{4+}}\, y_{O^{2-}}\, {}^{\circ}G_{Zr^{4+}:O^{2-}} + y_{Y^{3+}}\, y_{Va}\, {}^{\circ}G_{Y^{3+}:Va} + y_{Zr^{4+}}\, y_{Va}\, {}^{\circ}G_{Zr^{4+}:Va} + RT[y_{Y^{3+}} \ln y_{Y^{3+}} + y_{Zr^{4+}} \ln y_{Zr^{4+}} + 2(y_{O^{2-}} \ln y_{O^{2-}} + y_{Va} \ln y_{Va})] + {}^{E}G_m \quad (1)$$

and the Gibbs energy of the c-ZrO_2 and β-Y_2O_3 phases is given by Eq. 2,

$$G'_m = y_{Y^{3+}}\, y_{O^{2-}}\, {}^{\circ}G_{Y^{3+}:O^{2-}} + y_{Zr^{4+}}\, y_{O^{2-}}\, {}^{\circ}G_{Zr^{4+}:O^{2-}} + y_{Y^{3+}}\, y_{Va}\, {}^{\circ}G_{Y^{3+}:Va} + y_{Zr^{4+}}\, y_{Va}\, {}^{\circ}G_{Zr^{4+}:Va} + y_Y\, y_{O^{2-}}\, {}^{\circ}G_{Y:O^{2-}} + y_{Zr}\, y_{O^{2-}}\, {}^{\circ}G_{Zr:O^{2-}} + y_Y\, y_{Va}\, {}^{\circ}G_{Y:Va} + y_{Zr}\, y_{Va}\, {}^{\circ}G_{Zr:Va} + RT[y_Y \ln y_Y + y_{Y^{3+}} \ln y_{Y^{3+}} + y_{Zr} \ln y_{Zr} + y_{Zr^{4+}} \ln y_{Zr^{4+}} + 2(y_{O^{2-}} \ln y_{O^{2-}} + y_{Va} \ln y_{Va})] + {}^{E}G'_m \quad (2)$$

where y_j is site fraction of specie j in a particular sublattice. The excess Gibbs energy ${}^{E}G_m$ is defined as Eq. 3,

$${}^{E}G_m = y_{Y^{3+}}\, y_{Zr^{4+}}\, y_{O^{2-}} \sum_{i=0}^{n} {}^{i}L_{Y^{3+},\, Zr^{4+}:O^{2-}} (y_{Y^{3+}} - y_{Zr^{4+}})^i + y_{Y^{3+}}\, y_{Zr^{4+}}\, y_{Va} \sum_{i=0}^{n} {}^{i}L_{Y^{3+},\, Zr^{4+}:Va} (y_{Y^{3+}} - y_{Zr^{4+}})^i \quad (3)$$

and the excess Gibbs energy ${}^{E}G'_m$ is defined as Eq. 4,

$${}^{E}G'_m = y_{Y^{3+}}\, y_{Zr^{4+}}\, y_{O^{2-}} \sum_{i=0}^{n} {}^{i}L_{Y^{3+},\, Zr^{4+}:O^{2-}} (y_{Y^{3+}} - y_{Zr^{4+}})^i + y_{Y^{3+}}\, y_{Zr^{4+}}\, y_{Va} \sum_{i=0}^{n} {}^{i}L_{Y^{3+},\, Zr^{4+}:Va} (y_{Y^{3+}} - y_{Zr^{4+}})^i + y_{Zr}\, y_{Zr^{4+}}\, y_{O^{2-}} \sum_{i=0}^{n} {}^{i}L_{Zr,\, Zr^{4+}:O^{2-}} (y_{Zr} - y_{Zr^{4+}})^i + y_{Zr}\, y_{Zr^{4+}}\, y_{Va} \sum_{i=0}^{n} {}^{i}L_{Zr,\, Zr^{4+}:Va} (y_{Zr} - y_{Zr^{4+}})^i \quad (4)$$

where ${}^{i}L$ is the interaction parameter with the form of A+BT. If i=0, the solution is regular, if i=1, the solution is sub-regular, and if i=2, the solution is sub-sub-regular. It is worth mentioning that if no excess Gibbs energy is defined, the solution is ideal.

Chen et al. [56] modeled the Gibbs description of m-ZrO_2 phase as an ideal solution. However, I updated it from an ideal solution to a regular solution in the current work to better control the relative Gibbs energies. Therefore, the ${}^{0}L$ interaction parameter was considered to define an excess Gibbs energy for the m-ZrO_2 phase, which can change its stability. t-ZrO_2 phase was also considered as a regular solution and c-ZrO_2 and β-Y_2O_3 phases were treated as sub-regular solutions in this work. The Gibbs energy of the α-Y_2O_3 phase, which was treated as a regular solution in this work, is given by Eq. 5, in which y_1 and y_2 denote the second and third sublattices, respectively.

$$G''_m = y_{Y^{3+}} y_{1O^{2-}} y_{2Va} {}^{\circ}G_{Y^{3+}:O^{2-}:Va} + y_{Y^{3+}} y_{1O^{2-}} y_{2O^{2-}} {}^{\circ}G_{Y^{3+}:O^{2-}:O^{2-}} + y_{Y^{3+}} y_{1Va^{2-}} y_{2O^{2-}} {}^{\circ}G_{Y^{3+}:Va:O^{2-}} + y_{Y^{3+}} y_{1Va} y_{2Va} {}^{\circ}G_{Y^{3+}:Va:Va} + y_{Zr^{4+}} y_{1O^{2-}} y_{2Va} {}^{\circ}G_{Zr^{4+}:O^{2-}:Va} + y_{Zr^{4+}} y_{1O^{2-}} y_{2O^{2-}} {}^{\circ}G_{Zr^{4+}:O^{2-}:O^{2-}} + y_{Zr^{4+}} y_{1Va^{2-}} y_{2O^{2-}} {}^{\circ}G_{Zr^{4+}:Va:O^{2-}} + y_{Zr^{4+}} y_{1Va} y_{2Va} {}^{\circ}G_{Zr^{4+}:Va:Va} + y_Y y_{1O^{2-}} y_{2Va} {}^{\circ}G_{Y:O^{2-}:Va} + y_Y y_{1O^{2-}} y_{2O^{2-}} {}^{\circ}G_{Y:O^{2-}:O^{2-}} + y_Y y_{1Va^{2-}} y_{2O^{2-}} {}^{\circ}G_{Y:Va:O^{2-}} + y_Y y_{1Va} y_{2Va} {}^{\circ}G_{Y:Va:Va} + RT[2(y_Y \ln y_Y + y_{Y^{3+}} \ln y_{Y^{3+}} + y_{Zr^{4+}} \ln y_{Zr^{4+}}) + 3(y_{1O^{2-}} \ln y_{1O^{2-}} + y_{1Va} \ln y_{1Va}) + (y_{2O^{2-}} \ln y_{2O^{2-}} + y_{2Va} \ln y_{2Va})] + {}^{E}G''_m \quad (5)$$

The excess Gibbs energy ${}^{E}G''_m$ is defined as Eq. 6:

$${}^{E}G''_m = y_{Y^{3+}} y_{Zr^{4+}} y^2_{O^{2-}} \sum_{i=0}^{n} {}^{i}L_{Y^{3+},Zr^{4+}:O^{2-}:O^{2-}} (y_{Y^{3+}} - y_{Zr^{4+}})^i + y_{Y^{3+}} y_{Zr^{4+}} y_{O^{2-}} y_{Va} \sum_{i=0}^{n} {}^{i}L_{Y^{3+},Zr^{4+}:O^{2-}:Va} (y_{Y^{3+}} - y_{Zr^{4+}})^i + y_{Y^{3+}} y_{Zr^{4+}} y_{Va} y_{O^{2-}} \sum_{i=0}^{n} {}^{i}L_{Y^{3+},Zr^{4+}:Va:O^{2-}} (y_{Y^{3+}} - y_{Zr^{4+}})^i + y_{Y^{3+}} y_{Zr^{4+}} y^2_{Va} \sum_{i=0}^{n} {}^{i}L_{Y^{3+},Zr^{4+}:Va:Va} (y_{Y^{3+}} - y_{Zr^{4+}})^i \quad (6)$$

The ordered phase $Zr_3Y_4O_{12}$ is modeled as $(Zr^{4+})_3(Y^{3+})_4(O^{2-})_{12}$ and its Gibbs energy definition is given by Eq. 7:

$$G'''_m = y_{Zr^{4+}}\, y_{Y^{3+}}\, y_{O^{2-}}\, {}^{\circ}G_{Zr^{4+}:Y^{3+}:O^{2-}} \quad (7)$$

For the liquid phase, the model $(Y^{3+},Zr^{4+})_p(O^{2-},Va^{q-})_q$ was utilized, in which $p=2y_{O^{2-}}+qy_{Va^{q-}}$ and $q=3y_{Y^{3+}}+4y_{Zr^{4+}}$. The Gibbs energy of liquid is defined by Eq. 8:

$$G^L_m = y_{Y^{3+}}\, y_{O^{2-}}\, {}^{\circ}G^L_{Y^{3+}:O^{2-}} + y_{Y^{3+}}\, y_{Va^{q-}}\, {}^{\circ}G^L_{Y^{3+}:Va^{q-}} + y_{Zr^{4+}}\, y_{O^{2-}}\, {}^{\circ}G^L_{Zr^{4+}:O^{2-}} + y_{Zr^{4+}}\, y_{Va^{q-}}\, {}^{\circ}G^L_{Zr^{4+}:Va^{q-}} + RT[p(y_{Y^{3+}} \ln y_{Y^{3+}} + y_{Zr^{4+}} \ln y_{Zr^{4+}}) + q(y_{O^{2-}} \ln y_{O^{2-}} + y_{Va^{q-}} \ln y_{Va^{q-}})] + {}^{E}G^L_m \quad (8)$$

The excess Gibbs energy ${}^{E}G^L_m$ is given by Eq. 9:

$${}^{E}G^L_m = y_{Y^{3+}}\, y_{O^{2-}}\, y_{Va^{q-}} \sum_{i=0}^{n} {}^{i}L_{Y^{3+}:O^{2-}:Va^{q-}} (y_{O^{2-}} - y_{Va^{q-}})^i + y_{Zr^{4+}}\, y_{O^{2-}}\, y_{Va^{q-}} \sum_{i=0}^{n} {}^{i}L_{Zr^{4+}:O^{2-}:Va^{q-}} (y_{O^{2-}} - y_{Va^{q-}})^i + y_{Y^{3+}}\, y_{Zr^{4+}}\, y_{O^{2-}} \sum_{i=0}^{n} {}^{i}L_{Y^{3+},Zr^{4+}:O^{2-}} (y_{Y^{3+}} - y_{Zr^{4+}})^i + y_{Y^{3+}}\, y_{Zr^{4+}}\, y_{Va^{q-}} \sum_{i=0}^{n} {}^{i}L_{Y^{3+},Zr^{4+}:Va^{q-}} (y_{Y^{3+}} - y_{Zr^{4+}})^i \quad (9)$$

The liquid phase was modeled as a sub-sub-regular solution (i.e. ${}^{2}L$).

5.6. Parameters optimization procedure and discussion of results

In this section, the subsystems of the ZrO_2-$YO_{1.5}$ quasi-binary system are explained and the optimization procedure of the thermodynamic parameters are also described. The results of our developed database are then presented and compared with the related experimental data and previous calculated results.

In the current work, the thermodynamic description of ZrO_2-$YO_{1.5}$ system provided by Chen et al. [56] was used as a starting point and mainly the interaction parameters related to the liquid phase and solid solutions including α-Y_2O_3, β-Y_2O_3, c-ZrO_2, t-ZrO_2, and m-ZrO_2 of the ZrO_2-$YO_{1.5}$ quasi-binary system were optimized. The Parrot module [9] of Thermo-Calc® [103] was applied to evaluate the interaction parameters of each abovementioned phase. The selected experimental data were entered into this module and each one was given a certain weight based upon the selected data uncertainties specified in the literature and also upon the authors' judgement by examining all the experimental data

simultaneously. The main target during optimization was providing the best agreement of the calculated t-ZrO_2/t-ZrO_2+c-ZrO_2 and t-ZrO_2+c-ZrO_2/c-ZrO_2 phase boundaries with the selected experimental data. Therefore, the Gibbs energies of the t-ZrO_2 and c-ZrO_2 phases were changed, while trying to maintain the $YO_{1.5}$-rich side and the nature of invariant reactions of the system unchanged. In addition, the Gibbs energy of the liquid phase was slightly tuned to provide a better agreement with the more reliable experimental data.

The optimized thermodynamic description of the ZrO_2-$YO_{1.5}$ quasi-binary system is presented in Table 1. The reference state of each individual phase is the enthalpies of the pure elements in their stable states at 298 K, which is called Standard Element Reference (SER).

Table 1. Thermodynamic descriptions of the optimized phases in ZrO_2-$YO_{1.5}$ system

Cubic ZrO_2 (and β-Y_2O_3) **$(Y,Y^{3+},Zr,Zr^{4+})_1(O^{2-},Va)_2$**
${}^{\circ}G_{Y:O^{2-}} - \mathbf{H_Y^{SER}} - 2\mathbf{H_O^{SER}}$ = GHSERYY + 2 GHSEROO + 122800
${}^{\circ}G_{Y:Va} - \mathbf{H_Y^{SER}}$ = GHSERYY + 122800
${}^{\circ}G_{Y^{3+}:O^{2-}} - \mathbf{H_Y^{SER}} - 2\mathbf{H_O^{SER}}$ = GHHYO15 + 0.5 GHSEROO + 9.3511 T
${}^{\circ}G_{Y^{3+}:Va} - \mathbf{H_Y^{SER}}$ = GHHYO15 - 1.5 GHSEROO + 9.3511 T
${}^{\circ}G_{Zr:O^{2-}} - \mathbf{H_{Zr}^{SER}} - 2\mathbf{H_O^{SER}}$ = GHSERZR + 2 GHSEROO + 100000
${}^{\circ}G_{Zr:Va} - \mathbf{H_{Zr}^{SER}}$ = GHSERZR + 100000
${}^{\circ}G_{Zr^{4+}:O^{2-}} - \mathbf{H_{Zr}^{SER}} - 2\mathbf{H_O^{SER}}$ = GFFZRO2
${}^{\circ}G_{Zr^{4+}:Va} - \mathbf{H_{Zr}^{SER}}$ = GFFZRO2 – 2 GHSEROO
${}^{\circ}L_{Y^{3+},Zr^{4+}:O^{2-}} = {}^{\circ}L_{Y^{3+},Zr^{4+}:Va}$ = -71804 + 35 T
${}^{1}L_{Y^{3+},Zr^{4+}:O^{2-}} = {}^{1}L_{Y^{3+},Zr^{4+}:Va}$ = 17443 - 6.4 T
${}^{\circ}L_{Zr,Zr^{4+}:O^{2-}} = {}^{\circ}L_{Zr,Zr^{4+}:Va}$ = -66519 - 1.6 T
${}^{1}L_{Zr,Zr^{4+}:O^{2-}} = {}^{1}L_{Zr,Zr^{4+}:Va}$ = -20014 - 42 T
Tetragonal ZrO_2 **$(Y^{3+},Zr^{4+})_1(O^{2-},Va)_2$**
${}^{\circ}G_{Y^{3+}:O^{2-}} - \mathbf{H_Y^{SER}} - 2\mathbf{H_O^{SER}}$ = GMTYO15 + 0.5 GHSEROO + 9.3511 T
${}^{\circ}G_{Y^{3+}:Va} - \mathbf{H_Y^{SER}}$ = GMTYO15 - 1.5 GHSEROO + 9.3511 T
${}^{\circ}G_{Zr^{4+}:O^{2-}} - \mathbf{H_{Zr}^{SER}} - 2\mathbf{H_O^{SER}}$ = GTTZRO2
${}^{\circ}G_{Zr^{4+}:Va} - \mathbf{H_{Zr}^{SER}}$ = GTTZRO2 – 2 GHSEROO
${}^{\circ}L_{Y^{3+},Zr^{4+}:O^{2-}} = {}^{\circ}L_{Y^{3+},Zr^{4+}:Va}$ = -42191 + 25.1 T

Monoclinic ZrO_2 **$(Y^{3+},Zr^{4+})_1(O^{2-},Va)_2$**	
${}^{\circ}G_{Y^{3+}:O^{2-}} - \mathbf{H_Y^{SER}} - 2\mathbf{H_O^{SER}}$ = GMMYO15 + 0.5 GHSEROO + 9.3511 T	
${}^{\circ}G_{Y^{3+}:Va} - \mathbf{H_Y^{SER}}$ = GMMYO15 - 1.5 GHSEROO + 9.3511 T	
${}^{\circ}G_{Zr^{4+}:O^{2-}} - \mathbf{H_{Zr}^{SER}} - 2\mathbf{H_O^{SER}}$ = GMMZRO2	
${}^{\circ}G_{Zr^{4+}:Va} - \mathbf{H_{Zr}^{SER}}$ = GMMZRO2 – 2 GHSEROO	
${}^{\circ}L_{Y^{3+},Zr^{4+}:O^{2-}} = {}^{\circ}L_{Y^{3+},Zr^{4+}:Va}$ = 11000	
α-Y_2O_3 **$(Y,Y^{3+},Zr^{4+})_2(O^{2-},Va)_3(O^{2-},Va)_1$**	
${}^{\circ}G_{Y:O^{2-}:O^{2-}} - \mathbf{2H_Y^{SER}} - 4\mathbf{H_O^{SER}}$ = 2 GHSERYY + 4 GHSEROO + 345600 + 15.8769 T	
${}^{\circ}G_{Y:O^{2-}:Va} - \mathbf{2H_Y^{SER}} - 3\mathbf{H_O^{SER}}$ = 2 GHSERYY + 3 GHSEROO + 245600	
${}^{\circ}G_{Y:Va:O^{2-}} - \mathbf{2H_Y^{SER}} - \mathbf{H_O^{SER}}$ = 2 GHSERYY + GHSEROO + 345600 + 15.8769 T	
${}^{\circ}G_{Y:Va:Va} - \mathbf{2H_Y^{SER}}$ = 2 GHSERYY + 245600	
${}^{\circ}G_{Y^{3+}:O^{2-}:O^{2-}} - \mathbf{2H_Y^{SER}} - 4\mathbf{H_O^{SER}}$ = 2 GCCYO15 + GHSEROO + 100000 + 15.8769 T	
${}^{\circ}G_{Y^{3+}:O^{2-}:Va} - \mathbf{2H_Y^{SER}} - 3\mathbf{H_O^{SER}}$ = 2 GCCYO15	
${}^{\circ}G_{Y^{3+}:Va:O^{2-}} - \mathbf{2H_Y^{SER}} - \mathbf{H_O^{SER}}$ = 2 GCCYO15 – 2 GHSEROO + 100000 + 15.8769 T	
${}^{\circ}G_{Y^{3+}:Va:Va} - \mathbf{2H_Y^{SER}}$ = 2 GCCYO15 – 3 GHSEROO	
${}^{\circ}G_{Zr^{4+}:O^{2-}:O^{2-}} - \mathbf{2H_{Zr}^{SER}} - 4\mathbf{H_O^{SER}}$ = 2 GMCZRO2	
${}^{\circ}G_{Zr^{4+}:O^{2-}:Va} - \mathbf{2H_{Zr}^{SER}} - 3\mathbf{H_O^{SER}}$ = 2 GMCZRO2 – GHSEROO – 100000 – 15.8769 T	
${}^{\circ}G_{Zr^{4+}:Va:O^{2-}} - \mathbf{2H_{Zr}^{SER}} - \mathbf{H_O^{SER}}$ = 2 GMCZRO2 – 3 GHSEROO	
${}^{\circ}G_{Zr^{4+}:Va:Va} - \mathbf{2H_{Zr}^{SER}}$ = 2 GMCZRO2 – 4 GHSEROO – 100000 – 15.8769 T	
${}^{\circ}L_{Y^{3+},Zr^{4+}:O^{2-}:O^{2-}} = {}^{\circ}L_{Y^{3+},Zr^{4+}:O^{2-}:Va} = {}^{\circ}L_{Y^{3+},Zr^{4+}:Va:O^{2-}} = {}^{\circ}L_{Y^{3+},Zr^{4+}:Va:Va}$ = -74000 + 13.5 T	
$Zr_3Y_4O_{12}$ **$(Zr^{4+})_3(Y^{3+})_4(O^{2-})_{12}$**	
${}^{\circ}G_{Zr^{4+}:Y^{3+}:O^{2-}} - \mathbf{3H_{Zr}^{SER}} - \mathbf{4H_Y^{SER}} - 12\mathbf{H_O^{SER}}$ = 7 GZYO	
Liquid **$(Y^{3+},Zr^{4+})_p(O^{2-},Va^{q-})_q$** **$p=2y_{O^{2-}}+qy_{Va^{q-}}$, $q=3y_{Y^{3+}}+4y_{Zr^{4+}}$**	
${}^{\circ}G_{Y^{3+}:O^{2-}} - \mathbf{2H_Y^{SER}} - 3\mathbf{H_O^{SER}}$ = 2 GYYLIQ + 3 GHSEROO – 1824330 + 245.9 T	
${}^{\circ}G_{Y^{3+}:Va} - \mathbf{H_Y^{SER}}$ = GYYLIQ	
${}^{\circ}G_{Zr^{4+}:O^{2-}} - 2\mathbf{H_{Zr}^{SER}} - 4\mathbf{H_O^{SER}}$ = 2 GZRO2LIQ	
${}^{\circ}G_{Zr^{4+}:Va} - \mathbf{H_{Zr}^{SER}}$ = GZRLIQ	
${}^{\circ}L_{Y^{3+}:O^{2-},Va}$ = +6900	${}^{\circ}L_{Y^{3+},Zr^{4+}:O^{2-}}$ = +32000
${}^{1}L_{Y^{3+}:O^{2-},Va}$ = -17000	${}^{1}L_{Y^{3+},Zr^{4+}:O^{2-}}$ = -20000
${}^{\circ}L_{Zr^{4+}:O^{2-},Va}$ = -26500	${}^{2}L_{Y^{3+},Zr^{4+}:O^{2-}}$ = -24000
${}^{1}L_{Zr^{4+}:O^{2-},Va}$ = +50000	${}^{\circ}L_{Y^{3+},Zr^{4+}:Va}$ = +24000
${}^{2}L_{Zr^{4+}:O^{2-},Va}$ = +72000	${}^{1}L_{Y^{3+},Zr^{4+}:Va}$ = +3000
Functions	
GHSEROO = -3480.87-25.503038 T-11.136 T lnT-0.005098888 T^2+6.61846 × 10^{-7} T^3-38365 T^{-1} (298.15<T<1000) -6568.763+12.65988 T-16.8138 T lnT-5.95798 × 10^{-4} T^2+6.781 × 10^{-9} T^3+	

262905 T^{-1} (1000<T<3300) -13986.728+31.259625 T-18.9536 T lnT-4.25243 × 10^{-4} T^2+1.0721 × 10^{-8} T^3+ 4383200 T^{-1} (3300<T<6000)
GHSERYY = -8011.09379+128.572856 T-25.6656992 T lnT-0.00175716414 T^2- 4.17561786 × 10^{-7} T^3+26911.509 T^{-1} (100<T<1000) -7179.74574+114.497104 T-23.4941827 T lnT-0.0038211802 T^2-8.2534534 × 10^{-8} T^3 (1000<T<1795.15) -67480.7761+382.124727 T-56.9527111 T lnT+0.00231774379 T^2-7.22513088 × 10^{-8} T^3+18077162.6 T^{-1} (1795.15<T<3700)
GCCYO15 = -990900+381.86 T-62.85 T lnT-0.0025 T^2+1172000 T^{-1}-5.9 × 10^7 T^{-2}
GHHYO15 = GCCYO15+20000-8.1 T
GHSERZR = -7827.595+125.64905 T-24.1618 T lnT-4.37791 × 10^{-3} T^2+ 34971 T^{-1} (130<T<2128) -26085.921+262.724183 T-42.144 T lnT-1342.896 × 10^{28} T^{-9} (2128<T<6000)
GMMZRO2 = -1125300+416.9 T-68.4 T lnT-0.00335 T^2+586000 T^{-1}
GFFZRO2 = GMMZRO2+13500-7.159 T
GMTYO15 = GCCYO15+15000
GTTZRO2 = GMMZRO2+6000-4.326 T
GMMYO15 = GCCYO15+32700+20 T
GMCZRO2 = GFFZRO2+45000
GYYLIQ = 2098.50738+119.41873 T-24.6467508 T lnT-0.00347023463 T^2- 8.12981167 × 10^{-7} T^3+23713.7332 T^{-1} (100<T<1000) 7386.44846+19.4520171 T-9.0681627 T lnT-0.0189533369 T^2+1.7595327 × 10^{-6} T^3 (1000<T<1795.15) -12976.5957+257.400783 T-43.0952 T lnT (1795.15<T<3700)
GZRO2LIQ = -1077400+561.1 T-90 T lnT
GZRLIQ = GHSERZR+18147.69-9.080812 T+1.6275 × 10^{-22} T^7 (130<T<2128) -8281.26+253.812609 T-42.144 T lnT (2128<T<6000)
GZYO = 0.4286 GFFZRO2+0.5714 GCCYO15-15900+1 T

As it is presented in Table 1, we have considered an interaction parameter in the Gibbs energy description of m-ZrO_2 phase as a regular solution. The optimized amount of ˚L is 11000, which increases the Gibbs energy of m-ZrO_2 phase and makes it less stable. In other words, the respective stability of m-ZrO_2 phase decreases and as a result, the m-ZrO_2 phase region shrinks in the ZrO_2-$YO_{1.5}$ phase diagram.

Table 2 shows the interaction parameters optimized in this work in comparison with the ones from Chen et al. [56].

Table 2. Optimized interaction parameters in comparison with the work by Chen et al [56].

Phase	Interaction parameter	This work	Chen et al. [56]
Cubic ZrO_2 (and β-Y_2O_3)	${}^{\circ}L_{Y^{3+},Zr^{4+}:O^{2-}} = {}^{\circ}L_{Y^{3+},Zr^{4+}:Va}$	-71804 + 35 T	-76000 + 31.7 T
	${}^{1}L_{Y^{3+},Zr^{4+}:O^{2-}} = {}^{1}L_{Y^{3+},Zr^{4+}:Va}$	17443 - 6.4 T	+34200 - 8.6 T
	${}^{\circ}L_{Zr,Zr^{4+}:O^{2-}} = {}^{\circ}L_{Zr,Zr^{4+}:Va}$	-66519 - 1.6 T	-66500 - 1.6 T
	${}^{1}L_{Zr,Zr^{4+}:O^{2-}} = {}^{1}L_{Zr,Zr^{4+}:Va}$	20014 - 42 T	-20000 - 42 T
Tetragonal ZrO_2	${}^{\circ}L_{Y^{3+},Zr^{4+}:O^{2-}} = {}^{\circ}L_{Y^{3+},Zr^{4+}:Va}$	-42191 + 25.1 T	-48800 + 18.4 T
Monoclinic ZrO_2	${}^{\circ}L_{Y^{3+},Zr^{4+}:O^{2-}} = {}^{\circ}L_{Y^{3+},Zr^{4+}:Va}$	11000	0
α- Y_2O_3	${}^{\circ}L_{Y^{3+},Zr^{4+}:O^{2-}:O^{2-}} = {}^{\circ}L_{Y^{3+},Zr^{4+}:O^{2-}:Va} = {}^{\circ}L_{Y^{3+},Zr^{4+}:Va:O^{2-}} = {}^{\circ}L_{Y^{3+},Zr^{4+}:Va:Va}$	-74000 + 13.5 T	-88700 + 13 T
Liquid	${}^{\circ}L_{Y^{3+},Zr^{4+}:O^{2-}}$	+32000	+20100
	${}^{1}L_{Y^{3+},Zr^{4+}:O^{2-}}$	-20000	-13000
	${}^{2}L_{Y^{3+},Zr^{4+}:O^{2-}}$	-24000	-40000

5.6.1. ZrO_2-$YO_{1.5}$ Phase diagram

The phase diagram of ZrO_2-$YO_{1.5}$ system has been plotted and shown in Figure 19 based on the newly optimized database. The experimental data from different groups have also been superimposed on the diagram for comparison. As the differences between the diagram by Chen et al. [56] in dash line and the diagram calculated in this work in solid line show in Figure 19(A), mainly the t-ZrO_2/t-ZrO_2+c-ZrO_2, t-ZrO_2+c-ZrO_2/c-ZrO_2, m-ZrO_2+c-ZrO_2/c-ZrO_2, c-ZrO_2/c-ZrO_2+$Zr_3Y_4O_{12}$, and liquidus curves have changed. The invariant equilibrium temperature of t-ZrO_2, m-ZrO_2, and c-ZrO_2 has also changed. It is shown that

the c-ZrO_2 phase is less stable in the current work, while the liquid and tetragonal phases are more stable than the work by Chen et al. [56]. The ZrO_2-rich side of the system is also shown in Figure 19(B) while compared with the one by Chen et al. [56].

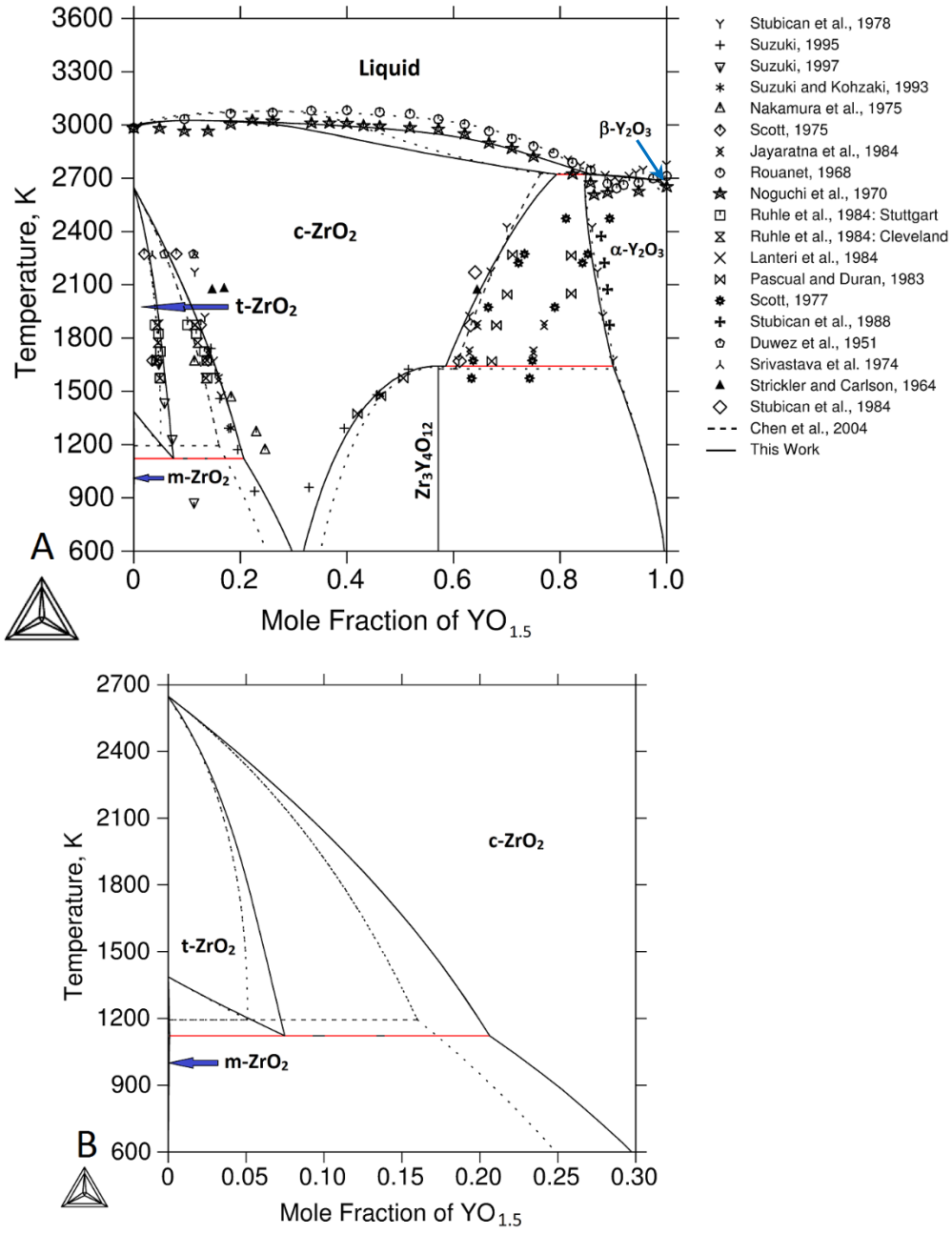

Figure 19. A) The ZrO_2-$YO_{1.5}$ quasi-binary phase diagram together with the experimental data from various groups. The phase diagram by Chen et al. [56] is shown in dash line. B) The ZrO_2-rich side comparing with the work by Chen et al. [56].

As it is seen in Figure 19, the calculated phase diagram in this work shows much better agreement with the experimental data, particularly on the ZrO_2-rich side of the diagram. As mentioned earlier, the experimental data were evaluated based on the determined criteria and selected carefully to assure the accuracy of the resultant database. The new phase diagram plotted in Figure 19 is in good agreement with the proposed diagram by Yashima et al. [25]. In addition, for the liquidus curve of YSZ system, Noguchi et al. [105] applied the specular reflection method [136] to measure the freezing points of various compositions in YSZ system in a full range of 0 to 100 mole% $YO_{1.5}$. The authors claimed that the true temperature of freezing point can be calculated by this method, in which the freezing point brightness temperature along with the spectral reflectivity of the samples are obtained. As it is seen in Figure 19, the liquidus curve in this work shows much better agreement with the data by Noguchi et al. [105] in comparison to the diagram by Chen et al. [56]. Moreover, as discussed before, the phase transformations are observed with delay during experiments. Therefore, since the typical approach of the selected experiments was observing the phase transformation during cooling process, it is expected that the real transformation temperature to be slightly more than what reported, especially at lower temperatures. Accordingly, the database was optimized in a way to consider this phenomenon in the t-ZrO_2/t-ZrO_2+c-ZrO_2 and t-ZrO_2+c-ZrO_2/c-ZrO_2 boundaries, as shown in Figure 19(A).

Table 3. Temperatures and compositions of invariant equilibria.

(a) $t\text{-}ZrO_2 \leftrightarrow m\text{-}ZrO_2 + c\text{-}ZrO_2$				
Reference	**Temperature, K**	***x*($YO_{1.5}$)**		
		$t\text{-}ZrO_2$	**$m\text{-}ZrO_2$**	**$c\text{-}ZrO_2$**
Srivastava et al. [114]	~838	~0.075		
Pascual and Duran [87]	763	0.086		
Srikanth and Subbarao [117]	843			
Suzuki [35]	~872			
Du et al. [77]	1279	0.058	~0	0.189
Chen et al. [56]	1194	0.051	0.0006	0.160
This work	1122	0.0748	0.0008	0.2062
(b) $c\text{-}ZrO_2 \leftrightarrow Zr_3Y_4O_{12} + \alpha\text{-}Y_2O_3$				
Reference	**Temperature, K**	***x*($YO_{1.5}$)**		
		$c\text{-}ZrO_2$	**$\alpha\text{-}Y_2O_3$**	
Scott [119]	1573	0.63		
Stubican et al. [31]	1650			
Du et al. [77]	1623	0.617	0.899	
Chen et al. [56]	1627	0.603	0.904	
This work	1641	0.5855	0.8995	
(c) Liquid $\leftrightarrow \alpha\text{-}Y_2O_3 + \beta\text{-}Y_2O_3$				
Reference	**Temperature, K**	***x*($YO_{1.5}$)**		
		Liquid	**$\alpha\text{-}Y_2O_3$**	**$\beta\text{-}Y_2O_3$**
Rouanet [118]	2653	0.904		
Noguchi et al. [105]	2603	0.864		
Stubican et al. [89]	2633	0.907		
Du et al. [77]	2679	0.902	0.897	0.955
Chen et al. [56]	2692	0.973	0.967	0.983
This work	2691	0.980	0.975	0.984
(d) $c\text{-}ZrO_2$ + Liquid $\leftrightarrow \alpha\text{-}Y_2O_3$				
Reference	**Temperature, K**	***x*($YO_{1.5}$)**		
		$\alpha\text{-}Y_2O_3$	**$c\text{-}ZrO_2$**	**Liquid**
Skaggs et al. [120]	2756	0.857	0.734	0.901
Stubican et al. [89]		0.864		
Du et al. [77]	2682	0.807	0.701	0.879
Chen et al. [56]	2725	0.844	0.764	0.864
This work	2721	0.836	0.779	0.849

(e) $Zr_3Y_4O_{12}$ ↔ c-ZrO_2		
Reference	**Temperature, K**	
Ray and Stubican [111]	1523	
Scott [119]	1643	
Stubican et al. [89]	1523	
Pascual and Duran [87]	1648	
Stubican et al. [31]	1655	
Du et al. [77]	1659	
Chen et al. [56]	1639	
This work	1642	

5.6.2. T_0 method for the diffusionless phase transformation

T-zero temperature method in the CALPHAD approach is under the partial equilibrium method, in which the compositions with equal Gibbs energies of the two adjacent phases at each temperature are calculated [16]. Therefore, a set of points in a two-phase region are calculated, which construct the T_0 line. In the ZrO_2-rich side of YSZ system, three major T_0 lines exist. T_0^{m-t} line is plotted between m-ZrO_2 and t-ZrO_2 phases, indicating the points at which the Gibbs energy of these two phases are equal at each determined temperature. Similarly, T_0^{m-c} and T_0^{t-c} lines are plotted between m-ZrO_2 and c-ZrO_2 phases, and t-ZrO_2 and c-ZrO_2 phases, respectively. The schematic diagram of the Gibbs energies of m-ZrO_2, t-ZrO_2, and c-ZrO_2 is shown in Figure 20. The T_0 points, global equilibrium, and metastable states are clearly shown in this diagram.

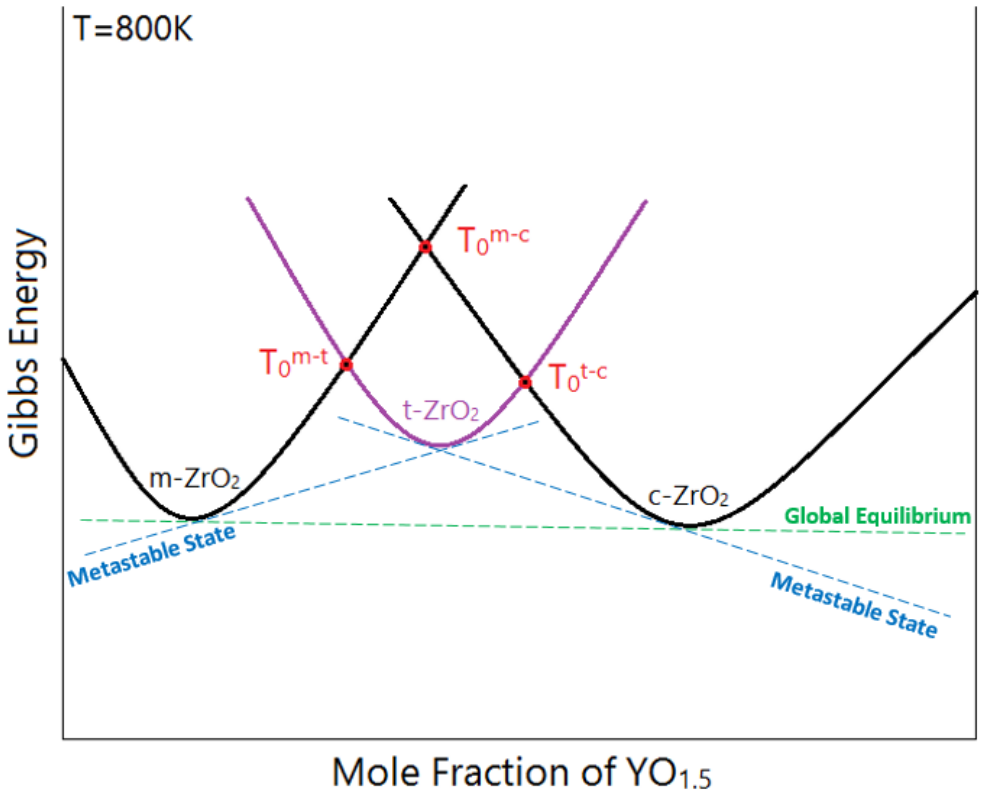

Figure 20. Schematic Gibbs energy diagram for the phases in ZrO_2-rich side of YSZ system.

It is known that the transition of m-ZrO_2 to t-ZrO_2 and vice versa occur martensitically [96]. Due to very slow kinetics, the transition is observed with a considerable delay. Therefore, capturing the exact phase transformation temperature is not possible. Kaufman and Cohen [83] suggested that the equilibrium temperature (T_0^{m-t}) can be calculated by taking an average of the starting transition temperature of m-ZrO_2 to t-ZrO_2 during heating and that of t-ZrO_2 to m-ZrO_2 during cooling. Based on this method, the T_0^{m-t} line can be captured experimentally.

The calculated T_0^{m-t} line along with the related experimental data is shown in Figure 21. The result of this work is also compared with that of Chen et al. [56].

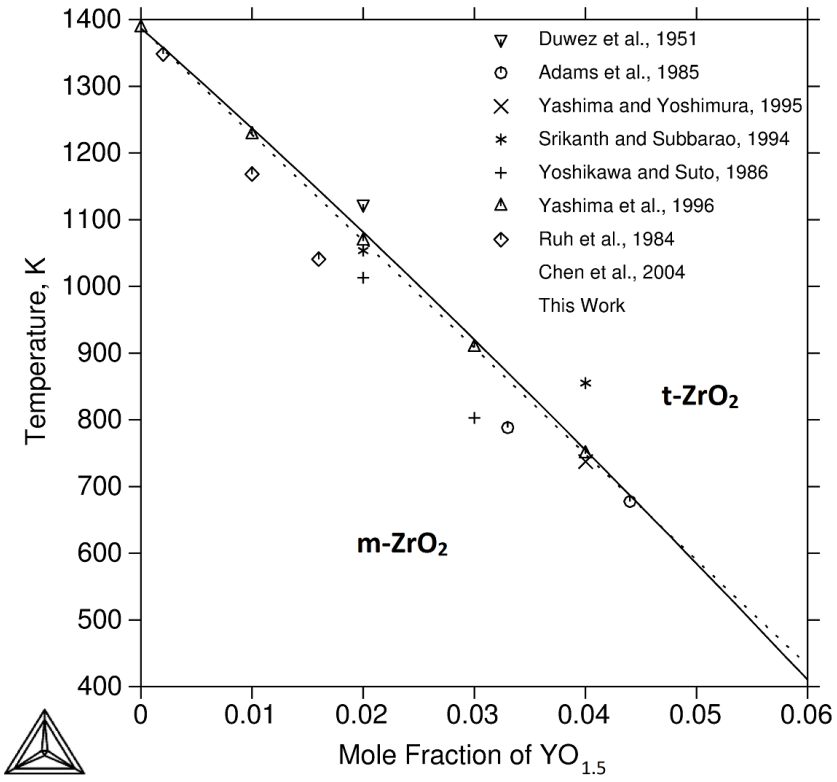

Figure 21. The calculated T_0^{m-t} line compared with the one calculated by Chen et al. [56] along with the experimental data.

According to Figure 21, it is seen that the T_0^{m-t} line calculated in this work has good agreement with the related experimental data, while it is almost compatible with the one from Chen et al. [56].

The T_0^{t-c} line calculated in this work along with the one from Chen et al. [56] is seen in Figure 22.

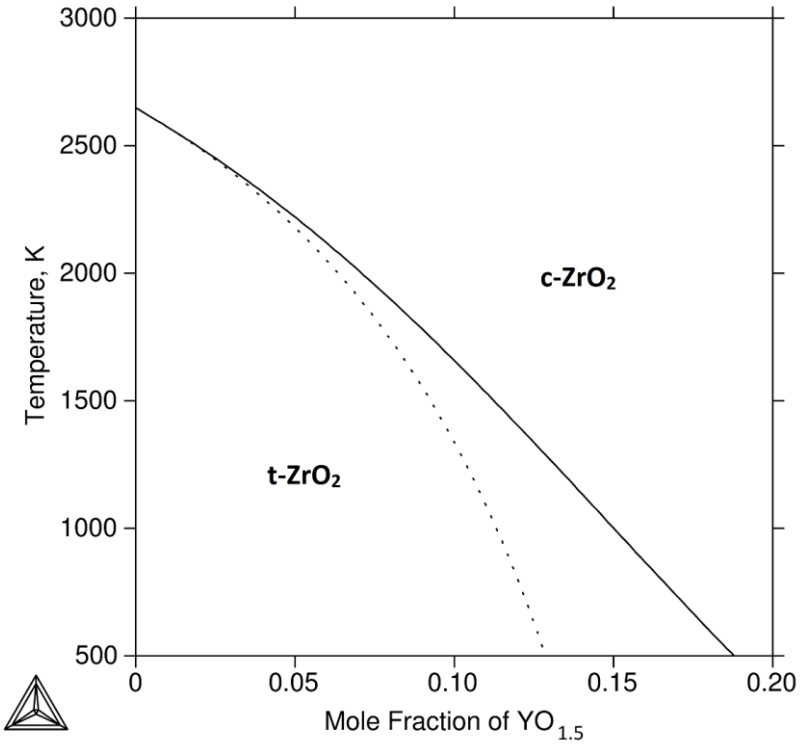

Figure 22. The calculated T_0^{t-c} line compared with the one calculated by Chen et al. [56] in dash line.

As it is seen in Figure 22, the calculated T_0^{t-c} line in this work shows considerable difference with the one from Chen et al. [56]. This difference becomes more significant while the temperature reduces, which is due to the extension of tetragonal region and shrinkage of cubic area. The comparison of phase diagrams calculated in the current work and by Chen et al. [56] in Figure 19 clearly shows the differences.

Figure 23 is the comparison of the calculated T_0^{m-c} line in this work with the one by Chen et al. [56]. Due to the expansion of the m-ZrO_2+c-ZrO_2 two-phase region in the current work because of decreasing the relative stability of the c-ZrO_2 phase, it is seen that the T_0^{m-c} line has been shifted slightly towards right side.

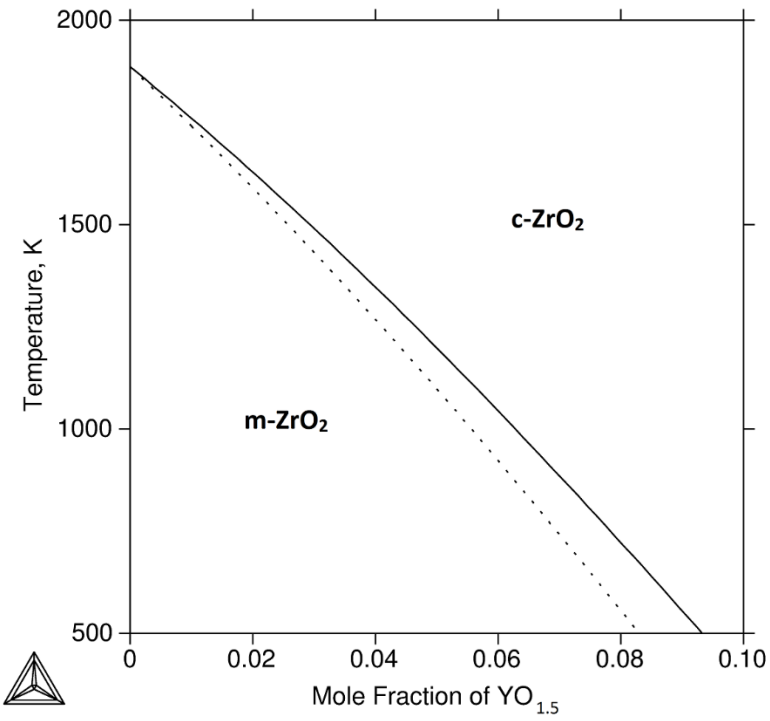

Figure 23- The calculated T_0^{m-c} line compared with the one calculated by Chen et al [56] in dash line.

As mentioned before, the Gibbs energies of the two adjacent phases are equal on the T_0 line. Therefore, it is concluded that in the region from T_0 line to the boundary of each phase, the Gibbs energy of that phase is less. Based on this conclusion, theoretically, the c-ZrO_2 is stable above T_0 line in Figure 22 and Figure 23, while the t-ZrO_2 and m-ZrO_2 are stable below T_0 line in Figure 22 and Figure 23, respectively. In Figure 21, theoretically, the t-ZrO_2 and m-ZrO_2 are stable above and below T_0 line, respectively. Therefore, the YSZ with 8 mole% Y_2O_3 is cubic in all temperature ranges, because due to the invariant equilibrium temperature in ZrO_2-rich side, the T_0 line in Figure 22 dominates above 1120 K and the T0 line in Figure 23 dominates below 1120 K.

5.6.3. Thermodynamic properties

Figure 24 shows the activity of ZrO_2 in the cubic phase at 2773 K. The experimental data are from Belov and Semenov [137]. As it is seen in this diagram, comparing with the result from Chen et al. [56], the calculated activity in the current work has better agreement with experimental data at the ZrO_2-rich side of the system, while the $YO_{1.5}$-rich side of the system has less agreement. It should be mentioned that c-ZrO_2 is metastable at $YO_{1.5}$-rich side of the system. Therefore, the experimental results of the ZrO_2 activity in the c-ZrO_2 phase at the $YO_{1.5}$-rich side might not be accurate, which was also confirmed in the assessment by Chen et al. [56].

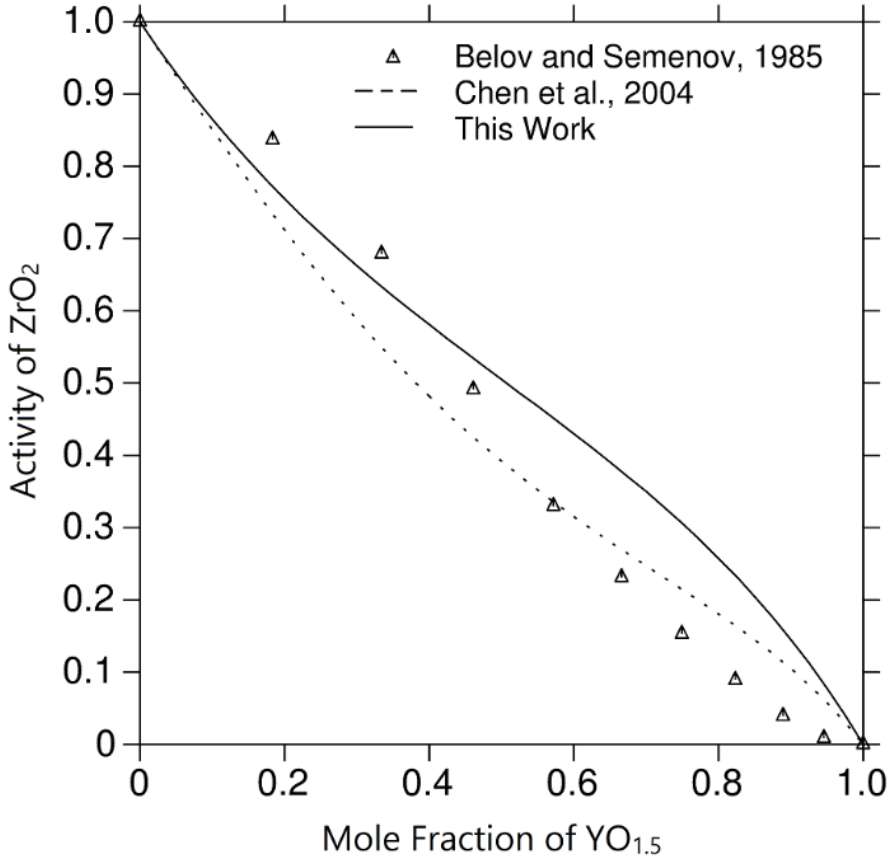

Figure 24.The activity of ZrO_2 in the c-ZrO_2 phase at 2773 K.

The relative chemical potential of ZrO_2 in c-ZrO_2 phase at 1273 K is shown in Figure 25. The superimposed experimental data are from Zaitseva and Dobrokhotova [138]. Since the optimized database in this work has a relatively less stable c-ZrO_2 phase in comparison to the one from Chen et al. [56], a slight difference is seen between the two calculated relative chemical potentials.

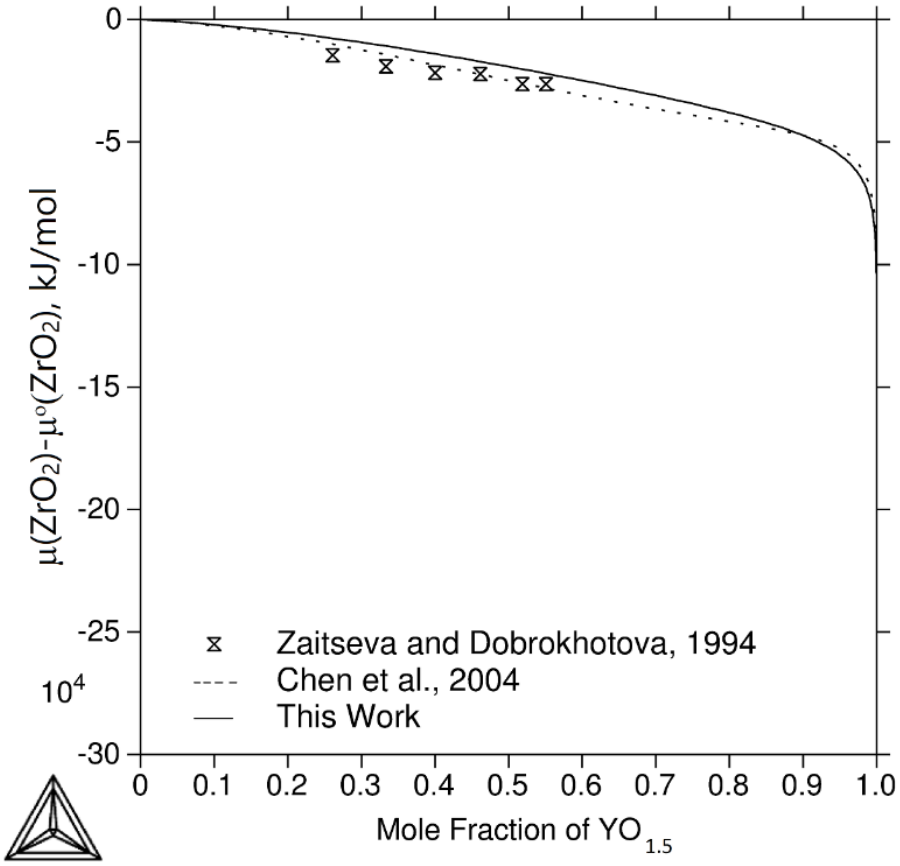

Figure 25. The relative chemical potential of ZrO_2 in the c-ZrO_2 phase at 1273 K.

The heat capacity (C_p) of c-ZrO_2 versus temperature with the $YO_{1.5}$ mole fractions of 0.2039 and 0.182 is plotted in Figure 26. There is no difference between the calculated C_p of this work with that from Chen et al. [56].

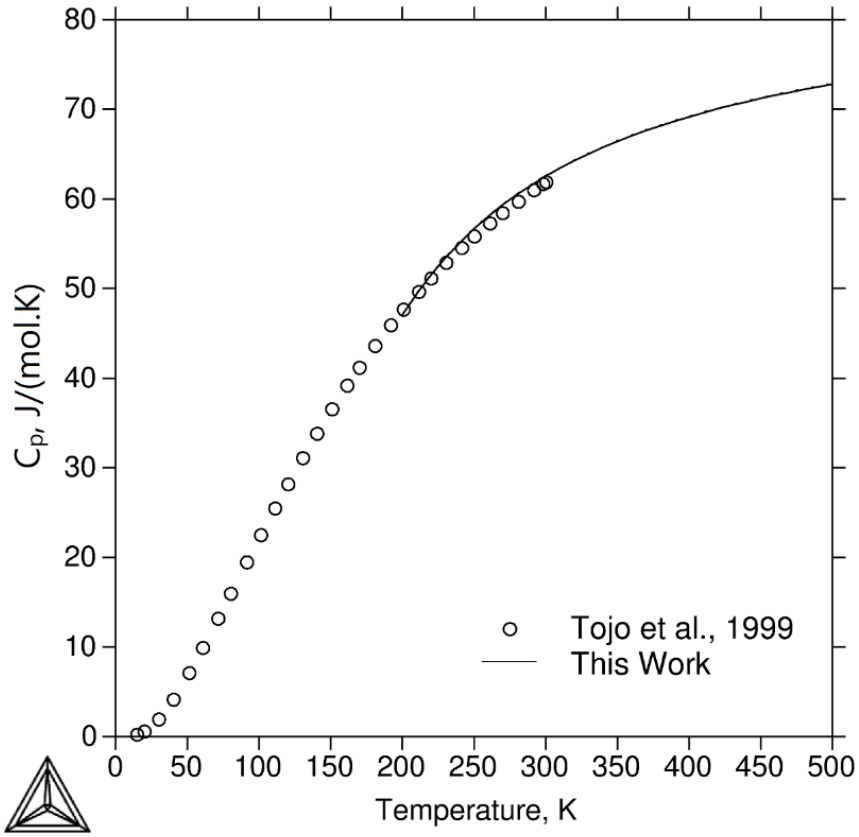

Figure 26. The heat capacity of c-ZrO_2 vs. temperature for $YO_{1.5}$ mole fraction of 0.2039. The C_p results calculated by the database from Chen et al. [56] are exactly the same as this work.

5.7. Summary

With the careful literature review of the previous experimental investigation on the phase equilibria on the ZrO_2-rich side and also the observation from our latest nano phase diagram for YSZ system, it is believed that the previous YSZ thermodynamic databases has overestimated the stabilities of the cubic ZrO_2 phase. In this work, an optimized thermodynamic database of the ZrO_2-$YO_{1.5}$ system has been provided. Due to sluggish kinetics of the system and several martensitic phase transformations, the experimental data were carefully selected based on their procedures, applied techniques, and result interpretations. The parameters of solid solution and liquid phases were then optimized in accordance with the selected experimental data, by applying the PARROT module of

Thermo-Calc. The new Gibbs energy description of each phase was provided based on the optimized parameters. Finally, several thermodynamic parameters were calculated using the optimized database and compared with the previous results. According to the calculated phase diagram by applying the optimized database, it was shown that the ZrO_2-rich side of the system has much better agreement with the related experimental data. An accurate database can lead to a more accurate material design and application. Furthermore, the metastable phase transformation boundaries (T_0^{m-c},T_0^{m-t}, $and\ T_0^{t-c}$) were plotted and discussed. These boundaries might be experimentally verified and could be an important benchmark to recognize the phase transformation in ZrO_2-rich side of YSZ system, which has a sluggish kinetics.

CHAPTER 6: SUMMARY AND FUTURE WORKS

6.1. The contributions of this dissertation

The summary of contributions in the current dissertation are as below:

It is important to understand the ionic conductivity of c-YSZ at different temperatures and compositions, due to the application of c-YSZ as an electrolyte in SOFCs. The oxygen vacancy concentration and oxygen ion mobility play pivotal roles in the ionic conductivity of c-YSZ. In this dissertation, the oxygen vacancy concentration was determined quantitatively in a range of temperature and YSZ composition for the first time by applying the CALPHAD approach. Moreover, the quantitative oxygen ion mobility diagrams at different temperatures and YSZ compositions were developed by the help of carefully selected experimental data. Therefore, the ionic conductivity of c-YSZ single crystals was predicted in a rage of temperature and Y_2O_3 concentration, by knowing the oxygen vacancy concentration and oxygen ion mobility. In addition, the activation energy and pre-exponential factor, both versus Y_2O_3 concentration, were predicted. It is worth mentioning that the conductivity of c-YSZ single crystals with low Y_2O_3 concentration was predicted as one of the important contributions of the current work, since sample preparation of c-YSZ single crystals with low Y_2O_3 concentration is not easily feasible due to the cubic-tetragonal phase transformation.

The stability regions for YSZ nano particles can be significantly different from that of the bulk YSZ. Due to the critical applications of zirconia-rich YSZ nano particles in the gas sensors and other devices, it is important to know the phase transformations and stability regions to be able to provide accurate designs. During this dissertation, the phase diagram for n-YSZ system at room temperature was developed with the bulk Gibbs energies from

the CALPHAD approach and specific surface energies of each crystal structure from the results of microcalorimetry experiments. The developed n-YSZ phase diagram at room temperature, which presents the phase stability regions based on the n-YSZ particle size and yttria concentration, was then extended to higher temperatures by the advantage of the CALPHAD approach. Therefore, a 3-D phase diagram for the zirconia-rich side of n-YSZ system was developed at temperatures up to 500˚C for the first time, by which the stability range of each phase in n-YSZ system is predicted based on particle size, composition, and temperature.

The accuracy of the phase diagrams, and more importantly the thermodynamic database is extremely critical to design various applications. In this dissertation, an optimized thermodynamic database of the ZrO_2-$YO_{1.5}$ system, as the most accurate version, has been provided. The optimization process was carried out based on the carefully selected experimental data, considering the sluggish kinetics of the system and existence of several martensitic phase transformations. In the newly optimized database, mainly the interaction parameters related to the liquid phase and solid solutions including α-Y_2O_3, β-Y_2O_3, c-ZrO_2, t-ZrO_2, and m-ZrO_2 of the ZrO_2-$YO_{1.5}$ quasi-binary system were optimized. The new Gibbs energy description of each phase was then provided based on the optimized interaction parameters. The thermodynamic database optimized during this dissertation can be applied to design more accurate applications. Furthermore, the metastable phase transformation boundaries (T_0^{m-c},T_0^{m-t}, $and\ T_0^{t-c}$) were plotted and discussed. These boundaries might be experimentally verified and could be an important benchmark to recognize the phase transformation in ZrO_2-rich side of YSZ system, which has a sluggish kinetics.

6.2. The future works

The outcomes of this dissertation have paved the way for further studies on the YSZ and other materials by applying the CALPHAD approach.

The predictions related to the oxygen vacancy concentration, ionic mobility, and ionic conductivity of c-YSZ single crystals in this work can be treated as the baseline to be applied in the future conductivity predictions for polycrystalline c-YSZ. In addition, the approach utilized in this work can be applied as a successful method to study the conductivity of calcia, magnesia, ceria, or alumina-stabilized zirconia.

The applied approach to develop the phase stability diagram of n-YSZ particles can be utilized for preparing the phase diagram of other nano materials such as calcia, magnesia, ceria, or alumina-stabilized zirconia nano particles. A lot of applications can be potentially designed for the nano particles of these composite ceramics based on their properties in different conditions. Moreover, the n-YSZ phase diagram can be updated by determining and considering the changes of specific surface energy by increasing the temperature. The predictions on the amorphous phase can also be improved by performing the appropriate modifications in the modeling of amorphous phases in the CALPHAD approach.

Lithium strontium manganite (LSM) is typically applied as the cathode in SOFCs. The reactions between cathode (LSM) and electrolyte (YSZ), in which the Mn ions migrate from the cathode and precipitate in the electrolyte, result in the device degradation. Therefore, improving the accuracy of Mn-Y-Zr-O quaternary thermodynamic database can lead to more accurate predictions to control the functionality of SOFCs in different conditions.

LIST OF REFERENCES

1. Chevalier, J., et al., *The tetragonal-monoclinic transformation in zirconia: Lessons learned and future trends.* Journal of the American Ceramic Society, 2009. **92**(9): p. 1901-1920.

2. Kelly, J.R. and I. Denry, *Stabilized zirconia as a structural ceramic: An overview.* Dental Materials, 2008. **24**(3): p. 289-298.

3. Wang, C.-H., et al., *Phase transformation and nanocrystallite growth behavior of 2 mol% yttria-partially stabilized zirconia (2Y-PSZ) powders.* Ceramics International, 2013. **39**(5): p. 5165-5174.

4. Nakamura, A. and J.B. Wagner, *Defect structure, ionic conductivity, and diffusion in yttria stabilized zirconia and related oxide electrolytes with fluorite structure.* Journal of the Electrochemical Society, 1986. **133**(8): p. 1542-1548.

5. Strickler, D.W. and W.G. Carlson, *Ionic conductivity of cubic solid solutions in the system CaO-Y_2O_3-ZrO_2.* Journal of the American Ceramic Society, 1964. **47**(3): p. 122-127.

6. Li, Y., et al., *Electrical conductivity of zirconia stabilized with yttria and calcia.* Journal of Materials Science Letters, 1999. **18**(6): p. 443-444.

7. Mahapatra, M.K., et al., *Electrical conductivity of manganese doped yttria (8mol%) stabilized zirconia.* Solid State Ionics, 2013. **253**: p. 223-226.

8. Saunders, N. and A.P. Miodownik, *CALPHAD (calculation of phase diagrams): a comprehensive guide*. Vol. 1. 1998: Elsevier.

9. Jansson, B., *Trita-Mac-0234.* Royal Institute of Technology, Stockholm, Sweden, 1984.

10. Lopez-Gándara, C., F.M. Ramos, and A. Cirera, *YSZ-based oxygen sensors and the use of nanomaterials: A review from classical models to current trends.* Journal of Sensors, 2009. **2009**.

11. Van Laar, J., *Melting or solidification curves in binary system.* Z Phys Chem, 1908. **63**: p. 216.

12. Kaufman, L. and H. Bernstein, *Computer calculation of phase diagrams. With special reference to refractory metals*. 1970, New York: Academic Press Inc.

13. Bale, C.W., et al., *FactSage thermochemical software and databases — recent developments.* Calphad, 2009. **33**(2): p. 295-311.

14. Asadikiya, M., et al., *Thermodynamic modeling and investigation of the oxygen effect on the sintering of B_4C.* Journal of Alloys and Compounds, 2017. **699**: p. 1022-1029.

15. Asadikiya, M., et al., *The role of CALPHAD approach in the sintering of B_4C with SiC as a sintering aid by spark plasma sintering technique.* Additive Manufacturing and Strategic Technologies in Advanced Ceramics: Ceramic Transactions, 2016. **258**: p. 185-191.

16. Asadikiya, M., et al., *Phase diagram for a nano-yttria-stabilized zirconia system.* RSC Advances, 2016. **6**(21): p. 17438-17445.

17. Asadikiya, M., et al., *The effect of sintering parameters on spark plasma sintering of B_4C.* Ceramics International, 2017. **43**(14): p. 11182-11188.

18. Darvish, S., et al., *Thermodynamic prediction of the effect of CO_2 to the stability of $(La_{0.8}Sr_{0.2})_{0.98}MnO_{3\pm\delta}$ system.* International Journal of Hydrogen Energy, 2016. **41**(24): p. 10239-10248.

19. Dinsdale, A.T., *SGTE DATA FOR PURE ELEMENTS.* Calphad-Computer Coupling of Phase Diagrams and Thermochemistry, 1991. **15**(4): p. 317-425.

20. Ansara, I. and B. Sundman. *Computer handling and dissemination of data*. in *Proc. of the Tenth CODATA Conf., Ottawa, Canada, Ed. Ph. S. Glaeser*. 1987.

21. Liu, Z.-K. and Y. Wang, *Computational thermodynamics of materials*. 2016: Cambridge University Press.

22. Garvie, R.C., R.H. Hannink, and R.T. Pascoe, *Ceramic steel?* Nature, 1975. **258**(5537): p. 703-704.

23. Adams, J.W. and H.H. Nakamura, *Thermal expansion behaviour of single-crystal zirconia.* Journal of the American Ceramic Society, 1985: p. 228-231.

24. Basu, B. and K. Balani, *Advanced structural ceramics*. 2011: John Wiley & Sons.

25. Yashima, M., M. Kakihana, and M. Yoshimura, *Metastable-stable phase diagrams in the zirconia-containing systems utilized in solid-oxide fuel cell application.* Solid State Ionics, 1996. **86-88**(PART 2): p. 1131-1149.

26. Ruff, O. and F. Ebert, *Beiträge zur Keramik hochfeuerfester Stoffe. l. Die Formen des Zirkondioxyds.* Zeitschrift fur Anorganische und Allgemeine Chemie, 1929. **180**(1): p. 19-41.

27. Padture, N.P., M. Gell, and E.H. Jordan, *Thermal barrier coatings for gas-turbine engine applications.* Science, 2002. **296**(5566): p. 280-284.

28. Vassen, R., et al., *Zirconates as new materials for thermal barrier coatings.* Journal of the American Ceramic Society, 2000. **83**(8): p. 2023-2028.

29. Etsell, T. and S.N. Flengas, *Electrical properties of solid oxide electrolytes.* Chemical Reviews, 1970. **70**(3): p. 339-376.

30. Ramamoorthy, R., P. Dutta, and S. Akbar, *Oxygen sensors: materials, methods, designs and applications.* Journal of materials science, 2003. **38**(21): p. 4271-4282.

31. Subbarao, E. and H. Maiti, *Solid electrolytes with oxygen ion conduction.* Solid State Ionics, 1984. **11**(4): p. 317-338.

32. Wagner, C., *Über den mechanismus der elektrischen stromleitung im nernststift.* Naturwissenschaften, 1943. **31**(23): p. 265-268.

33. Suzuki, Y. and T. Kohzaki, *Electrical conduction behavior and phase transition of Y_2O_3-stabilized ZrO_2.* Solid State Ionics, 1993. **59**(3): p. 307-312.

34. Suzuki, Y., *Phase transition temperature of ZrO_2-Y_2O_3 solid solutions (2.4-6 mol% Y_2O_3).* Solid State Ionics, 1997. **95**(3-4): p. 227-230.

35. Suzuki, Y., *Phase transition temperature of fluorite-type ZrO_2-Y_2O_3 solid solutions containing 8-44 mol% Y_2O_3.* Solid State Ionics, 1995. **81**(3): p. 211-216.

36. Pimenov, A., et al., *Ionic conductivity and relaxations in ZrO_2-Y_2O_3 solid solutions.* Solid State Ionics, 1998. **109**(1): p. 111-118.

37. Kwon, O.H. and G.M. Choi, *Electrical conductivity of thick film YSZ.* Solid State Ionics, 2006. **177**(35): p. 3057-3062.

38. Luo, J., D.P. Almond, and R. Stevens, *Ionic mobilities and association energies from an analysis of electrical impedance of ZrO_2-Y_2O_3 alloys.* Journal of the American Ceramic Society, 2000. **83**(7): p. 1703-1708.

39. Park, J.H. and R.N. Blumenthal, *Electronic Transport in 8 Mole Percent Y_2O_3-ZrO_2.* Journal of the Electrochemical Society, 1989. **136**(10): p. 2867-2876.

40. Ikeda, S., et al., *Electrical conductivity of yttria-stabilized zirconia single crystals.* Journal of materials science, 1985. **20**(12): p. 4593-4600.

41. Asadikiya, M., et al., *Integrated investigation of the $Li_4Ti_5O_{12}$ phase stability.* Ionics, 2017: p. 1-7.

42. Lee, E., F.B. Prinz, and W. Cai, *Enhancing ionic conductivity of bulk single-crystal yttria-stabilized zirconia by tailoring dopant distribution.* Physical Review B, 2011. **83**(5): p. 052301.

43. Lee, E., F.B. Prinz, and W. Cai, *Ab initio kinetic Monte Carlo model of ionic conduction in bulk yttria-stabilized zirconia.* Modelling and Simulation in Materials Science and Engineering, 2012. **20**(6): p. 065006.

44. Meyer, M., N. Nicoloso, and V. Jaenisch, *Percolation model for the anomalous conductivity of fluorite-related oxides.* Physical Review B, 1997. **56**(10): p. 5961.

45. Pornprasertsuk, R., et al., *Predicting ionic conductivity of solid oxide fuel cell electrolyte from first principles.* Journal of applied physics, 2005. **98**(10): p. 103513.

46. Devanathan, R., et al., *Computer simulation of defects and oxygen transport in yttria-stabilized zirconia.* Solid State Ionics, 2006. **177**(15): p. 1251-1258.

47. Huang, C., W. Wei, and C. Chen, *Simulation of atomic-scale defects in the clustering and oxygen jumping process of 8 mol% yttria-stabilised zirconia.* Journal of Ceramic Processing Research, 2010. **11**(6): p. 641-647.

48. Huang, H.C., et al., *Molecular dynamics simulation of oxygen ion diffusion in yttria stabilized zirconia single crystals and bicrystals.* Fuel Cells, 2014. **14**(4): p. 574-580.

49. Darvish, S., et al., *Quantitative Defect Chemistry Analysis and Electronic Conductivity Prediction of $La_{0.8}Sr_{0.2}MnO_{3\pm\delta}$ Perovskite.* Journal of The Electrochemical Society, 2015. **162**(9): p. E134-E140.

50. Darvish, S., S.K. Saxena, and Y. Zhong. *Quantitative Analysis of $(La_{0.8}Sr_{0.2})_{0.98}MnO_{3\pm\delta}$ Electronic Conductivity Using CALPHAD Approach*. in *Developments in Strategic Ceramic Materials: A Collection of Papers Presented at the 39th International Conference on Advanced Ceramics and Composites*. 2015. Wiley Online Library.

51. Barsoum, M., *Fundamentals of ceramics*. 2002: CRC press.

52. Casselton, R., *Low field DC conduction in yttria-stabilized zirconia.* physica status solidi (a), 1970. **2**(3): p. 571-585.

53. Zhang, C., et al., *Ionic conductivity and its temperature dependence of atmospheric plasma-sprayed yttria stabilized zirconia electrolyte.* Materials Science and Engineering: B, 2007. **137**(1): p. 24-30.

54. Kilner, J.A. and B.C.H. Steele, *Nonstoichiometric Oxides*. 1981, New York: Academic Press.

55. Sabarou, H., et al., *Thermodynamic assessment of the chemical stability of $(La_{0.8}Sr_{0.2})_{0.98}Cr_x\ Fe_{1-x}O_{3\pm\delta}$ under oxygen transport membrane fabrication and operation conditions.* Solid State Ionics, 2017. **310**: p. 1-9.

56. Chen, M., B. Hallstedt, and L.J. Gauckler, *Thermodynamic modeling of the ZrO_2-$YO_{1.5}$ system.* Solid State Ionics, 2004. **170**(3): p. 255-274.

57. Guo, X. and J. Maier, *Grain boundary blocking effect in zirconia: a Schottky barrier analysis.* Journal of the Electrochemical Society, 2001. **148**(3): p. E121-E126.

58. Liou, S. and W. Worrell, *Electrical properties of novel mixed-conducting oxides.* Applied Physics A: Materials Science & Processing, 1989. **49**(1): p. 25-31.

59. Ramamoorthy, R., D. Sundararaman, and S. Ramasamy, *Ionic conductivity studies of ultrafine-grained yttria stabilized zirconia polymorphs.* Solid State Ionics, 1999. **123**(1): p. 271-278.

60. Badwal, S.P.S. and M.V. Swain, *ZrO_2-Y_2O_3: electrical conductivity of some fully and partially stabilized single grains.* Journal of materials science letters, 1985. **4**(4): p. 487-489.

61. Abelard, P. and J. Baumard, *Study of the dc and ac electrical properties of an yttria-stabilized zirconia single crystal $[(ZrO_2)_{0.88}$-$(Y_2O_3)_{0.12}]$*. Physical Review B, 1982. **26**(2): p. 1005.

62. Goodenough, J.B., *Oxide-ion electrolytes.* Annual review of materials research, 2003. **33**(1): p. 91-128.

63. Kawada, T., et al., *Reaction between solid oxide fuel cell materials.* Solid State Ionics, 1992. **50**(3-4): p. 189-196.

64. Kröger, F., *Electronic conductivity of calcia-stabilized zirconia.* Journal of the American Ceramic Society, 1966. **49**(4): p. 215-218.

65. Tien, T. and E. Subbarao, *X-ray and electrical conductivity study of the fluorite phase in the system ZrO_2–CaO.* The Journal of Chemical Physics, 1963. **39**(4): p. 1041-1047.

66. Ioffe, A., D. Rutman, and S. Karpachov, *On the nature of the conductivity maximum in zirconia-based solid electrolytes.* Electrochimica Acta, 1978. **23**(2): p. 141-142.

67. Schmalzried, H., *On correlation effects of vacancies in ionic crystals.* Zeitschrift für Physikalische Chemie, 1977. **105**(1-2): p. 47-62.

68. Zhu, J., et al., *Probing local electrochemical activity within yttria-stabilized-zirconia via in situ high-temperature atomic force microscopy.* Journal of Materials Research, 2015. **30**(03): p. 357-363.

69. Sawaguchi, N. and H. Ogawa, *Simulated diffusion of oxide ions in $YO_{1.5}$–ZrO_2 at high temperature.* Solid State Ionics, 2000. **128**(1): p. 183-189.

70. Krishnamurthy, R., et al., *Oxygen diffusion in yttria-stabilized zirconia: A new simulation model.* Journal of the American Ceramic Society, 2004. **87**(10): p. 1821-1830.

71. Brog, J.-P., et al., *Polymorphism, what it is and how to identify it: a systematic review.* RSC Advances, 2013. **3**(38): p. 16905-16931.

72. Gross, R. and A. Marx, *Festkörperphysik*. 2014: Walter de Gruyter GmbH & Co KG.

73. Castro, R.H.R., *On the thermodynamic stability of nanocrystalline ceramics.* Materials Letters, 2013. **96**: p. 45-56.

74. Garvie, R., *The occurrence of metastable tetragonal zirconia as a crystallite size effect.* The journal of physical chemistry, 1965. **147**(1950): p. 1238-1243.

75. Garvie, R. and P. Nicholson, *Phase analysis in zirconia systems.* Journal of the American Ceramic Society, 1972(June): p. 303-305.

76. Ding, H., A.V. Virkar, and F. Liu, *Defect configuration and phase stability of cubic versus tetragonal yttria-stabilized zirconia.* Solid State Ionics, 2012. **215**: p. 16-23.

77. Du, Y., Z.P. Jin, and P.Y. Huang, *Thermodynamic assessment of the ZrO_2-$YO_{1.5}$ system.* Journal of the American Ceramic Society, 1991. **74**(7): p. 1569-1577.

78. Jacobson, N.S., et al., *Thermodynamic modeling of the $YO_{1.5}$-ZrO_2 system.* Journal of the American Ceramic Society, 2004. **1566**: p. 1559-1566.

79. Krogstad, J.a., et al., *Effect of yttria content on the zirconia unit cell parameters.* Journal of the American Ceramic Society, 2011. **94**(12): p. 4548-4555.

80. Suresh, A., M.J. Mayo, and W.D. Porter, *Thermodynamics for nanosystems: Grain and particle-size dependent phase diagrams.* Reviews on Advanced Materials Science, 2003. **5**(2): p. 100-109.

81. Drazin, J.W. and R.H.R. Castro, *Phase stability in nanocrystals: A predictive diagram for yttria-zirconia.* Journal of the American Ceramic Society, 2015. **98**(4): p. 1377-1384.

82. Drazin, J.W. and R.H.R. Castro, *Water adsorption microcalorimetry model: Deciphering surface energies and water chemical potentials of nanocrystalline oxides.* Journal of Physical Chemistry C, 2014. **118**(19): p. 10131-10142.

83. Kaufman, L. and M. Cohen, *Thermodynamics and kinetics of martensitic transformations.* Progress in Metal Physics, 1958. **7**: p. 165-246.

84. Porter, D.A., K.E. Easterling, and M. Sherif, *Phase transformations in metals and alloys, (Revised Reprint)*. 2009: CRC press.

85. Samsonov, V.M., a.N. Bazulev, and N.Y. Sdobnyakov, *On applicability of Gibbs thermodynamics to nanoparticles.* Central European Journal of Physics, 2003. **1**(3): p. 474-484.

86. Frolov, T. and Y. Mishin, *Temperature dependence of the surface free energy and surface stress: An atomistic calculation for Cu(110).* Physical Review B, 2009. **79**(4): p. 1-10.

87. Pascual, C. and P. Duran, *Subsolidus phase-equilibria and ordering in the system ZrO_2-Y_2O_3.* Journal of the American Ceramic Society, 1983. **66**(1): p. 23-27.

88. Scott, H.G., *Phase relationships in the zirconia-yttria system.* Journal of Materials Science, 1975. **10**(9): p. 1527-1535.

89. Stubican, V.S., R.C. Hink, and S.P. Ray, *Phase-equilibria and ordering in system ZrO_2-Y_2O_3.* Journal of the American Ceramic Society, 1978. **61**(1-2): p. 17-21.

90. Popov, V.V., et al., *Stabilization of the fluorite phase in the ZrO_2–Y_2O_3 system.* Russian Metallurgy (Metally), 2017. **2016**(9): p. 869-874.

91. Chaim, R., A.H. Heuer, and D.G. Brandon, *Phase equilibration in ZrO_2-Y_2O_3 alloys by liquid-film migration.* Journal of the American Ceramic Society, 1986. **69**(3): p. 243-248.

92. Degtyarev, S.A. and G.F. Voronin, *Solution of ill-posed problems in thermodynamics of phase-equilibria. The ZrO_2-Y_2O_3 system.* Calphad-Computer Coupling of Phase Diagrams and Thermochemistry, 1988. **12**(1): p. 73-82.

93. Hillert, M. and T. Sakuma, *Thermodynamic modeling of the C-T transformation in ZrO_2 alloys.* Acta Metallurgica Et Materialia, 1991. **39**(6): p. 1111-1115.

94. Ruh, R., et al., *Phase-relations in the system ZrO_2-Y_2O_3 at low Y_2O_3 contents.* Journal of the American Ceramic Society, 1984. **67**(9): p. C190-C192.

95. Yoshikawa, N. and H. Suto, *Transformation behavior of Y_2O_3-PSZ investigated by thermal dilatometry.* Journal of the Japan Institute of Metals, 1986. **50**(1): p. 108-113.

96. Yoshimura, M., *Phase-stability of zirconia.* American Ceramic Society Bulletin, 1988. **67**(12): p. 1950-1955.

97. Ikuma, Y., Y. Tsubaki, and T. Masaki, *Oxygen diffusion in Y_2O_3-containing tetragonal zirconia polycrystals with different grain sizes.* Nippon Seramikkusu Kyokai Gakujutsu Ronbunshi-Journal of the Ceramic Society of Japan, 1991. **99**(1): p. 101-103.

98. Magunov, R.L., G.L. Shklyar, and V.F. Katridi, *Phase diagram of the $ZrO_2(HfO_2)$-Sc_2O_3 System.* Inorganic Materials, 1989. **25**(7): p. 1035-1037.

99. Ruh, R., et al., *System zirconia-scandia.* Journal of the American Ceramic Society, 1977. **60**(9-10): p. 399-403.

100. Sakka, Y., Y. Oishi, and K. Ando, *Zr-Hf inter-diffusion in polycrystalline Y_2O_3-$(Zr+Hf)O_2$.* Journal of Materials Science, 1982. **17**(11): p. 3101-3105.

101. Sheu, T.S., J. Xu, and T.Y. Tien, *Phase-relationships in the ZrO_2-Sc_2O_3 and ZrO_2-In_2O_3 systems.* Journal of the American Ceramic Society, 1993. **76**(8): p. 2027-2032.

102. Shevchenko, A.V., I.M. Maister, and L.M. Lopato, *Reactions in the HfO_2-Sc_2O_3 and ZrO_2-Sc_2O_3 systems at high-temperatures.* Inorganic Materials, 1987. **23**(8): p. 1169-1173.

103. Andersson, J.-O., et al., *Thermo-Calc & DICTRA, computational tools for materials science.* Calphad, 2002. **26**(2): p. 273-312.

104. Lefèvre, J., *Some structural modifications of fluorite-type phases in systems based on zirconia or hafnium oxide.* Ann. Chim.(Paris), 1963. **8**(1-2): p. 117-149.

105. Noguchi, T., M. Mizuno, and T. Yamada, *The liquidus curve of the ZrO_2-Y_2O_3 system as measured by a solar furnace.* Bulletin of the Chemical Society of Japan, 1970. **43**(8): p. 2614-2616.

106. Predith, A., et al., *Ab initio prediction of ordered ground-state structures in ZrO_2-Y_2O_3.* Physical Review B, 2008. **77**(14): p. 144104.

107. Rühle, M., N. Claussen, and A.H. Heuer, *Science and technology of zirconia II*, ed. N. Claussen, M. Rühle, and A.H. Heuer. Vol. 12. 1984, Columbus, OH: American Ceramic Society.

108. Sakuma, T., *Microstructural aspects on the cubic-tetragonal transformation in zirconia.* Key Engineering Materials, 1998. **153-154**: p. 75-96.

109. Yagi, T., et al., *Analytical electron microscopy of yttria partitioning in the yttria-partially-stabilized zirconia crystal.* Journal of the American Ceramic Society, 1986. **69**(1): p. C3-C4.

110. Yoshikawa, N., H. Eda, and H. Suto, *On the cubic tetragonal phase-equilibrium of the ZrO_2-Y_2O_3 system.* Journal of the Japan Institute of Metals, 1986. **50**(1): p. 113-118.

111. Ray, S.P. and V.S. Stubican, *Fluorite related ordered compounds in ZrO_2-CaO and ZrO_2-Y_2O_3 systems.* Materials Research Bulletin, 1977. **12**(5): p. 549-556.

112. Jayaratna, M., M. Yoshimura, and S. Somiya, *Subsolidus phase-relations in the pseudoternary system ZrO_2-$YO_{1.5}$-$CrO_{1.5}$ in air*. Journal of the American Ceramic Society, 1984. **67**(11): p. C240-C242.

113. Duwez, P., F.H. Brown, and F. Odell, *The zirconia-yttria system.* Journal of the electrochemical society, 1951. **98**(9): p. 356-362.

114. Srivastava, K., et al., *Revised phase diagram of the system ZrO_2-$YO_{1.5}$.* Transactions and Journal of the British Ceramic Society, 1974. **73**(3): p. 85-91.

115. Baldinozzi, G., et al., *Segregation and site selectivity in Zr-doped Y_2O_3.* Journal of Physics: Condensed Matter, 1997. **9**(45): p. 9731-9744.

116. Calderon-Moreno, J.M. and M. Yoshimura, *Characterization by Raman spectroscopy of solid solutions in the yttria-rich side of the zirconia-yttria system.* Solid State Ionics, 2002. **154-155**: p. 125-133.

117. Srikanth, V. and E.C. Subbarao, *Acoustic-emission study of phase-relations in low-Y_2O_3 portion of ZrO_2-Y_2O_3 system.* Journal of Materials Science, 1994. **29**(12): p. 3363-3371.

118. Rouanet, A., *High temperature solidification and phase diagrams of the ZrO_2-Er_2O_3, ZrO_2-Y_2O_3 and ZrO_2-Yb_2O_3 systems.* CR Seances Acad. Sci., Ser. C, 1968. **267**(23): p. 1581-1584.

119. Scott, H.G., *Phase relationships in the yttira-rich part of the yttria-zirconia system.* Journal of Materials Science, 1977. **12**: p. 311-316.

120. Skaggs, S. and L. NELSON. *ZrO_2-Y_2O_2 system above 2000˚C*. in *American Ceramic Society Bulletin*. 1972. Amer Ceramic Soc 735 Ceramic Place, Po Box 6136, Westerville, Oh 43081-6136.

121. Ono, A., *Phase transformation in the system ZrO_2-CeO_2.* Mineralogical Journal, 1972. **7**(1): p. 66-76.

122. Yashima, M., et al., *Effects of noncompositional inhomogeneity on t→ m phase transformation during grinding of various rare-earth-doped zirconias.* Journal of the American Ceramic Society, 1991. **74**(12): p. 3011-3016.

123. Lange, F.F., *Transformation-toughened ZrO_2-correlations between grain-size control and composition in the system ZrO_2-Y_2O_3.* Journal of the American Ceramic Society, 1986. **69**(3): p. 240-242.

124. Hund, F., *Anomale mischkristalle im system ZrO_2-Y_2O_3 kristallbau der Nernst-Stifte.* Berichte der Bunsengesellschaft für physikalische Chemie, 1951. **55**(5): p. 363-366.

125. Dixon, J., et al., *Electrical resistivity of stabilized zirconia at elevated temperatures.* Journal of the Electrochemical Society, 1963. **110**(4): p. 276-280.

126. Mazdiyasni, K., C. Lynch, and J.S. II, *Cubic phase stabilization of translucent yttria-zirconia at very low temperatures.* Journal of the American Ceramic Society, 1967. **50**(10): p. 532-537.

127. Nakamura, K., S. Hirano, and S. Somiya, *The system ZrO_2-Y_2O_3 under hydrothermal condition at 1000 kg/cm^2.* Yogyo Kyokasishi, 1975. **83**: p. 570-574.

128. Fabrichnaya, O. and F. Aldinger, *Assessment of thermodynamic parameters in the system ZrO_2-Y_2O_3-Al_2O_3.* Zeitschrift Fur Metallkunde, 2004. **95**(1): p. 27-39.

129. Fabrichnaya, O., et al., *Phase equilibria and thermodynamic properties of the ZrO_2-$GdO_{1.5}$-$YO_{1.5}$ system.* Journal of phase equilibria and diffusion, 2005. **26**(6): p. 591-604.

130. Wang, K., et al., *Thermodynamic modeling of the ZrO_2-$YO_{1.5}$-TiO_2 system.* Metallurgical and Materials Transactions A, 2010. **41**(13): p. 3525-3534.

131. Romberger, K., C. Baes, and H. Stone, *Phase equilibrium studies in the UO_2-ZrO_2 system.* Journal of Inorganic and Nuclear Chemistry, 1967. **29**(7): p. 1619-1626.

132. Stubican, V.S. and S.P. Ray, *Phase-equilibria and ordering in system ZrO_2-CaO.* Journal of the American Ceramic Society, 1977. **60**(11-1): p. 534-537.

133. Tani, E., M. Yoshimura, and S. Somiya, *Revised phase diagram of the system ZrO_2-CeO_2 below 1400˚C.* Journal of the American Ceramic Society, 1983. **66**(7): p. 506-510.

134. Yashima, M., et al., *Low temperature phase equilibria by the flux method and the metastable-mtable phase diagram in the ZrO_2-CeO_2 system.* Journal of the American Ceramic Society, 1994. **77**(7): p. 1869-1874.

135. Yoshimura, M., E. Tani, and S. Somiya, *The confirmation of phase-equilibria in the system ZrO_2-CeO_2 below 1400˚C.* Solid State Ionics, 1981. **3-4**(AUG): p. 477-481.

136. Noguchi, T. and T. Kozuka, *Temperature and emissivity measurement at 0.65 μ with a solar furnace.* Solar Energy, 1966. **10**(3): p. 125-131.

137. Belov, A. and G. Semenov, *Thermodynamics of binary solid solutions of zirconium, hafnium and yttrium oxides from high temperature mass spectrometry data.* Zhurnal Fizicheskoj Khimii, 1985. **59**(3): p. 589-592.

138. Zaitseva, I.A. and Z.V. Dobrokhotova, *Thermodynamic functions of zirconia in fluorite solid solutions of the ZrO_2-Y_2O_3 system.* Inorganic Materials, 1994. **30**(7): p. 886-888.

APPENDICES

Appendix A

The ZrO_2-$YO_{1.5}$ quasi-binary database

```
ELEMENT /-   ELECTRON_GAS              0.0000E+00  0.0000E+00  0.0000E+00!
ELEMENT VA   VACUUM                    0.0000E+00  0.0000E+00  0.0000E+00!
ELEMENT O    1/2_MOLE_O2(G)            1.5999E+01  4.3410E+03  1.0252E+02!
ELEMENT Y    HCP_A3                    8.8906E+01  5.9664E+03  4.4434E+01!
ELEMENT ZR   HCP_A3                    9.1224E+01  5.5663E+03  3.9181E+01!
SPECIES O-2                 O1/-2!
SPECIES O2                  O2!
SPECIES O3                  O3!
SPECIES Y+3                 Y1/+3!
SPECIES Y2O                 O1Y2!
SPECIES Y2O2                O2Y2!
SPECIES Y2O3                O3Y2!
SPECIES Y2ZR2O7             O7Y2ZR2!
SPECIES YO                  O1Y1!
SPECIES YO15                O1.5Y1!
SPECIES YO2                 O2Y1!
SPECIES ZR+4                ZR1/+4!
SPECIES ZR2                 ZR2!
SPECIES ZRO                 O1ZR1!
SPECIES ZRO2                O2ZR1!
```

FUNCTION GHSEROO 298.15 -3480.87-25.503038*T-11.136*T*LN(T)
-0.005098888*T**2+6.61846E-07*T**3-38365*T**(-1); 1000 Y
-6568.763+12.65988*T-16.8138*T*LN(T)-5.95798E-04*T**2+6.781E-09*T**3
+262905*T**(-1); 3300 Y
-13986.728+31.259625*T-18.9536*T*LN(T)-4.25243E-04*T**2
+1.0721E-08*T**3+4383200*T**(-1); 6000 N !

FUNCTION GZRGAS 298.15 +586876.841+74.4171195*T-38.69111*T*LN(T)
+0.01152846*T**2-1.693255E-06*T**3+270638.8*T**(-1); 700 Y
+595990.293-26.0530509*T-24.06106*T*LN(T)+0.001743641*T**2
-5.94312333E-07*T**3-748947.5*T**(-1); 1300 Y
+593841.673-46.0204551*T-20.46361*T*LN(T)-0.002961084*T**2
+1.08391433E-07*T**3+526352.5*T**(-1); 2700 Y
+630745.052-161.965371*T-6.647343*T*LN(T)-0.0046738955*T**2
+1.06833583E-07*T**3-15872340*T**(-1); 6600 Y
+504260.272+131.813821*T-40.68801*T*LN(T)-6.38357E-04*T**2
+1.79125333E-08*T**3+71496950*T**(-1); 10000 N !

FUNCTION GYYLIQ 100 +2098.50738+119.41873*T-24.6467508*T*LN(T)
-0.00347023463*T**2-8.12981167E-07*T**3+23713.7332*T**(-1); 1000 Y
+7386.44846+19.4520171*T-9.0681627*T*LN(T)-0.0189533369*T**2
+1.7595327E-06*T**3; 1795.15 Y
-12976.5957+257.400783*T-43.0952*T*LN(T); 3700 N !

FUNCTION GZRO2LIQ 298.15 -1077400+561.1*T-90*T*LN(T); 6000 N !

FUNCTION GHSERZR 130 -7827.595+125.64905*T-24.1618*T*LN(T)
-0.00437791*T**2+34971*T**(-1); 2128 Y
-26085.921+262.724183*T-42.144*T*LN(T)-1.342896E+31*T**(-9); 6000 N !

FUNCTION GZRLIQ 130 +18147.69-9.080812*T+GHSERZR#
+1.6275E-22*T**7; 2128 Y
-8281.26+253.812609*T-42.144*T*LN(T); 6000 N !

FUNCTION GHSERYY 100 -8011.09379+128.572856*T-25.6656992*T*LN(T)
-0.00175716414*T**2-4.17561786E-07*T**3+26911.509*T**(-1); 1000 Y
-7179.74574+114.497104*T-23.4941827*T*LN(T)-0.0038211802*T**2
-8.2534534E-08*T**3; 1795.15 Y
-67480.7761+382.124727*T-56.9527111*T*LN(T)+0.00231774379*T**2
-7.22513088E-08*T**3+18077162.6*T**(-1); 3700 N !

FUNCTION GCCYO15 298.15 -990900+381.86*T-62.85*T*LN(T)-0.0025*T**2
+1172000*T**(-1)-59000000*T**(-2); 6000 N !

FUNCTION GMMZRO2 298.15 -1125300+416.9*T-68.4*T*LN(T)-0.00335*T**2
+586000*T**(-1); 6000 N !

```
FUNCTION GFFZRO2     298.15 +GMMZRO2#+13500-7.159*T; 6000 N !

FUNCTION GMCZRO2   298.15 +GFFZRO2#+45000; 6000 N !

FUNCTION GHHYO15    298.15 +GCCYO15#+20000-8.1*T; 6000 N !

FUNCTION GMMYO15   298.15 +GCCYO15#+32700+20*T; 6000 N !

FUNCTION GMTYO15    298.15 +GCCYO15#+15000; 6000 N !

FUNCTION GTTZRO2     298.15 +GMMZRO2#+6000-4.326*T; 6000 N !

FUNCTION GZYO          298.15 +0.4286*GFFZRO2#+0.5714*GCCYO15#
     -1.2873512E+04+1.0268864*T; 6000 N !

FUNCTION RTLNP         298.15 +8.31451*T*LN(1E-05*P); 6000 N !

$ Y(g):
FUNCTION F14722T   298.15  +413926.156+43.942359*T-34.19791*T*LN(T)
     +0.0122297*T**2-2.14534333E-06*T**3+97071.5*T**(-1);
     700.00  Y  +417505.307-13.2762864*T-25.29082*T*LN(T)
     +0.002768476*T**2-3.169895E-07*T**3-157006.6*T**(-1);
     2000.00  Y  +439627.78-100.082079*T-14.64876*T*LN(T)
     +0.001182233*T**2-3.39037833E-07*T**3-7693105*T**(-1);
     3300.00  Y  +656873.926-957.210194*T+92.15071*T*LN(T)
     -0.022050485*T**2+6.04918167E-07*T**3-90137500*T**(-1);
     5500.00  Y  -81672.0087+877.446829*T-122.4532*T*LN(T)
     +0.005666115*T**2-6.61492667E-08*T**3+3.865857E+08*T**(-1); 10000.00  N !

$ Y2O(g):
FUNCTION F12945T   298.15  -18834.6011+47.2728187*T-49.14357*T*LN(T)
     -0.007582635*T**2+1.2067E-06*T**3+211591.55*T**(-1);
     900.00  Y  -23590.8983+106.946886*T-58.08361*T*LN(T)
     -2.2921245E-05*T**2+7.790445E-10*T**3+695520*T**(-1);          6000.00  N !

$ YO(g):
FUNCTION F12929T   298.15  -55980.1334-24.7804591*T-30.58571*T*LN(T)
     -0.005797885*T**2+9.044075E-07*T**3+92955.75*T**(-1);
     900.00  Y  -62402.7508+43.7949244*T-40.60318*T*LN(T)
     +0.0014897095*T**2-1.41268333E-07*T**3+896318.5*T**(-1);
     3100.00  Y  +22970.3078-236.507016*T-6.632106*T*LN(T)
     -0.004295709*T**2+3.30261667E-08*T**3-38281150*T**(-1);
     5900.00  Y  +78439.9263-450.3653*T+19.37683*T*LN(T)
     -0.00859432*T**2+1.53217517E-07*T**3-45013010*T**(-1);
     9600.00  Y  -949291.433+1103.17067*T-151.1803*T*LN(T)
     +0.004000447*T**2-2.13031E-08*T**3+1.118062E+09*T**(-1);     10000.00  N !
```

```
$ Y2O2(g):
FUNCTION F13270T   298.15  -575737.712+51.4042333*T-49.55549*T*LN(T)
     -0.030210885*T**2+5.27799667E-06*T**3+255509.3*T**(-1);
     700.00  Y  -591679.029+265.724012*T-82.06371*T*LN(T)
     -2.6169375E-04*T**2+1.0952625E-08*T**3+1742125.5*T**(-1);
     4500.00  Y  -594803.763+277.512452*T-83.52789*T*LN(T)
     +4.9195245E-05*T**2-1.17628333E-09*T**3+3139224*T**(-1);      6000.00  N !

$ YO2(g):
FUNCTION F13266T   298.15  -453353.172+38.0172466*T-44.87379*T*LN(T)
     -0.011836705*T**2+2.00650833E-06*T**3+281931.45*T**(-1);
     800.00  Y  -459941.788+124.969156*T-58.0167*T*LN(T)
     -3.724498E-05*T**2+1.29613517E-09*T**3+910973.5*T**(-1);      6000.00  N !

$ Gas Zr2 (ssub)
FUNCTION F15702T   298.15  +892794.963-14.4120751*T-37.13672*T*LN(T)
     -3.2039655E-04*T**2-4.30605167E-09*T**3+85422.15*T**(-1);
     3600.00  Y  +874148.858+9.34917918*T-39.33356*T*LN(T)
     -0.001019669*T**2+6.09799667E-08*T**3+14065805*T**(-1);      6000.00  N !

$ Gas ZrO (ssub)
FUNCTION F12964T   298.15  +84650.2479-322.816859*T+21.98592*T*LN(T)
     -0.10713165*T**2+2.81704E-05*T**3-333363.35*T**(-1);
     500.00  Y  +42648.3264+404.464721*T-93.37933*T*LN(T)
     +0.03332466*T**2-3.80849833E-06*T**3+2526299*T**(-1);
     1100.00  Y  +84838.707+11.527709*T-37.46259*T*LN(T)
     +9.16682E-05*T**2-7.005105E-08*T**3-3491878*T**(-1);
     4100.00  Y  +106867.647-98.6658671*T-23.49987*T*LN(T)
     -0.00315689*T**2+5.93994E-08*T**3-6661880*T**(-1);
     9600.00  Y  +255442.536-262.961955*T-6.281221*T*LN(T)
     -0.0038787795*T**2+6.18786667E-08*T**3-2.2466925E+08*T**(-1);
     10000.00  N !

$ Gas ZrO2 (ssub)
FUNCTION F13281T   298.15  -332610.845+3.22325893*T-38.10718*T*LN(T)
     -0.01852473*T**2+3.29626E-06*T**3+218721.05*T**(-1);
     700.00  Y  -342836.09+140.579945*T-58.93983*T*LN(T)
     +6.65405E-04*T**2-8.11812167E-08*T**3+1173742*T**(-1);
     2600.00  Y  -272800.105-96.5265444*T-30.24766*T*LN(T)
     -0.0038011495*T**2-1.83201667E-11*T**3-28436635*T**(-1);
     4900.00  Y  -36436.1523-803.246487*T+54.45089*T*LN(T)
     -0.017172935*T**2+3.92562833E-07*T**3-1.509956E+08*T**(-1);    6000.00  N !

$ O(g) :
FUNCTION F7397T    298.15  +243206.529-42897.0876*T**(-1)-20.7513421*T
     -21.0155542*T*LN(T)+1.26870532E-04*T**2-1.23131285E-08*T**3;
```

```
    2950.00  Y  +252301.473-3973170.33*T**(-1)-51.974853*T
    -17.2118798*T*LN(T)-5.41356254E-04*T**2+7.64520703E-09*T**3; 6000.00  N !

$ O3(g) :
FUNCTION F7683T    298.15  +133772.042-11328.9959*T**(-1)-84.8602165*T
    -19.8314069*T*LN(T)-0.0392015696*T**2+7.90727187E-06*T**3;
    600.00  Y  +120765.524+997137.156*T**(-1)+120.113376*T
    -51.8410152*T*LN(T)-0.00353983136*T**2+3.20640143E-07*T**3;
    1500.00  Y  +115412.196+1878139.02*T**(-1)+164.679664*T
    -58.069736*T*LN(T)-2.84399032E-04*T**2+5.95650279E-10*T**3;   6000.00  N !

FUNCTION UN_ASS 298.15 +0; 300 N !

TYPE_DEFINITION % SEQ *!

DEFINE_SYSTEM_DEFAULT ELEMENT 2 !

DEFAULT_COMMAND DEF_SYS_ELEMENT VA /- !

PHASE GAS:G %  1  1.0  !
   CONSTITUENT GAS:G :O,O2,O3,Y,Y2O,Y2O2,YO,YO2,ZR,ZR2,ZRO,ZRO2 :  !
  PARAMETER G(GAS,O;0)        298.15 +F7397T#+RTLNP#; 6000 N            REF0 !
  PARAMETER G(GAS,O2;0)       298.15 +2*GHSEROO#+RTLNP#; 6000 N         REF0 !
  PARAMETER G(GAS,O3;0)       298.15 +F7683T#+RTLNP#; 6000 N            REF0 !
  PARAMETER G(GAS,Y;0)        298.15 +F14722T#+RTLNP#; 6000 N           REF0 !
  PARAMETER G(GAS,Y2O;0)      298.15 +F12945T#+RTLNP#; 6000 N           REF0 !
  PARAMETER G(GAS,Y2O2;0)     298.15 +F13270T#+RTLNP#; 6000 N           REF0 !
  PARAMETER G(GAS,YO;0)       298.15 +F12929T#+RTLNP#; 6000 N           REF0 !
  PARAMETER G(GAS,YO2;0)      298.15 +F13266T#+RTLNP#; 6000 N           REF0 !
  PARAMETER G(GAS,ZR;0)       298.15 +GZRGAS#+RTLNP#; 6000 N            REF0 !
  PARAMETER G(GAS,ZR2;0)      298.15 +F15702T#+RTLNP#; 6000 N           REF0 !
  PARAMETER G(GAS,ZRO;0)      298.15 +F12964T#+RTLNP#; 6000 N           REF0 !
  PARAMETER G(GAS,ZRO2;0)     298.15 +F13281T#+RTLNP#; 6000 N           REF0 !

PHASE IONIC_LIQUID:Y %  2 9   7 !
   CONSTITUENT IONIC_LIQUID:Y :Y+3,ZR+4 : O-2,VA :  !
  PARAMETER G(IONIC_LIQUID,Y+3:O-2;0)  298.15 +2*GYYLIQ#+3*GHSEROO#
  -1824330+245.9*T; 6000 N                                              REF0 !
  PARAMETER G(IONIC_LIQUID,ZR+4:O-2;0) 298.15 +2*GZRO2LIQ#;
  6000 N                                                                REF0 !
  PARAMETER G(IONIC_LIQUID,Y+3:VA;0)     298.15 +GYYLIQ#; 6000 N        REF0 !
  PARAMETER G(IONIC_LIQUID,ZR+4:VA;0)    298.15 +GZRLIQ#; 6000 N        REF0 !
  PARAMETER G(IONIC_LIQUID,Y+3,ZR+4:O-2;0) 298.15 32000; 6000 N         REF0 !
  PARAMETER G(IONIC_LIQUID,Y+3,ZR+4:O-2;1) 298.15 -20000; 6000 N        REF0 !
  PARAMETER G(IONIC_LIQUID,Y+3,ZR+4:O-2;2) 298.15 -24000; 6000 N        REF0 !
  PARAMETER G(IONIC_LIQUID,Y+3:O-2,VA;0) 298.15 +6900; 6000 N           REF0 !
```

```
  PARAMETER G(IONIC_LIQUID,Y+3:O-2,VA;1) 298.15 -17000; 6000 N       REF0 !
  PARAMETER G(IONIC_LIQUID,ZR+4:O-2,VA;0) 298.15 -26500; 6000 N      REF0 !
  PARAMETER G(IONIC_LIQUID,ZR+4:O-2,VA;1) 298.15 +50000; 6000 N      REF0 !
  PARAMETER G(IONIC_LIQUID,ZR+4:O-2,VA;2) 298.15 +72000; 6000 N      REF0 !
  PARAMETER G(IONIC_LIQUID,Y+3,ZR+4:VA;0) 298.15 +24000; 6000 N      REF0 !
  PARAMETER G(IONIC_LIQUID,Y+3,ZR+4:VA;1) 298.15 +3000; 6000 N       REF0 !

PHASE O2_GAS  %  1  1.0  !
   CONSTITUENT O2_GAS  :O2 :  !
  PARAMETER G(O2_GAS,O2;0)   298.15 +2*GHSEROO#+RTLNP#; 6000 N  REF0 !

PHASE Y2O3_CUB:I %  3 2   3   1 !
   CONSTITUENT Y2O3_CUB:I :Y,Y+3,ZR+4 : O-2,VA : O-2,VA :  !
  PARAMETER G(Y2O3_CUB,Y:O-2:O-2;0)       298.15 +2*GHSERYY#+245600
  +4*GHSEROO#+100000+15.87691*T; 6000 N                              REF0 !
  PARAMETER G(Y2O3_CUB,Y+3:O-2:O-2;0)   298.15 +2*GCCYO15#+GHSEROO#
  +15.87691*T+100000; 6000 N                                         REF0 !
  PARAMETER G(Y2O3_CUB,ZR+4:O-2:O-2;0) 298.15 +2*GMCZRO2#;
  6000 N                                                             REF0 !
  PARAMETER G(Y2O3_CUB,Y:VA:O-2;0)       298.15 +2*GHSERYY#+245600
  +GHSEROO#+100000+15.87691*T; 6000 N                                REF0 !
  PARAMETER G(Y2O3_CUB,Y+3:VA:O-2;0)    298.15 +2*GCCYO15#
  -2*GHSEROO#+15.87691*T+100000; 6000 N                              REF0 !
  PARAMETER G(Y2O3_CUB,ZR+4:VA:O-2;0)  298.15 +2*GMCZRO2#
  -3*GHSEROO#;   6000 N                                              REF0 !
  PARAMETER G(Y2O3_CUB,Y:O-2:VA;0)       298.15 +2*GHSERYY#+245600
  +3*GHSEROO#; 6000 N                                                REF0 !
  PARAMETER G(Y2O3_CUB,Y+3:O-2:VA;0)    298.15 +2*GCCYO15#;
  6000 N                                                             REF0 !
  PARAMETER G(Y2O3_CUB,ZR+4:O-2:VA;0)  298.15 +2*GMCZRO2#
  -GHSEROO#-100000-15.87691*T; 6000 N                                REF0 !
  PARAMETER G(Y2O3_CUB,Y:VA:VA;0)        298.15 +2*GHSERYY#+245600;
  6000 N                                                             REF0 !
  PARAMETER G(Y2O3_CUB,Y+3:VA:VA;0)     298.15 +2*GCCYO15#
  -3*GHSEROO#;   6000 N                                              REF0 !
  PARAMETER G(Y2O3_CUB,ZR+4:VA:VA;0)   298.15 +2*GMCZRO2#
  -4*GHSEROO#-100000-15.87691*T;  6000 N                             REF0 !
  PARAMETER G(Y2O3_CUB,Y+3,ZR+4:O-2:O-2;0) 298.15
  -74000+1.3531485E+01*T;  6000 N                                    REF0 !
  PARAMETER G(Y2O3_CUB,Y+3,ZR+4:VA:O-2;0) 298.15
  -74000+1.3531485E+01*T;  6000 N                                    REF0 !
  PARAMETER G(Y2O3_CUB,Y+3,ZR+4:O-2:VA;0) 298.15
  -74000+1.3531485E+01*T;  6000 N                                    REF0 !
  PARAMETER G(Y2O3_CUB,Y+3,ZR+4:VA:VA;0) 298.15
  -74000+1.3531485E+01*T;  6000 N                                    REF0 !
```

```
PHASE ZR3Y4O12  %  3 3   4   12 !
   CONSTITUENT ZR3Y4O12  :ZR+4 : Y+3 : O-2 :  !
  PARAMETER G(ZR3Y4O12,ZR+4:Y+3:O-2;0)   298.15 +7*GZYO#; 6000 N   REF0 !

PHASE ZRO2_CUB:I %  2 1   2 !
   CONSTITUENT ZRO2_CUB:I :Y,Y+3,ZR,ZR+4 : O-2,VA :  !
  PARAMETER G(ZRO2_CUB,Y:O-2;0)          298.15 +GHSERYY#+2*GHSEROO#
  +122800;    6000 N                                                REF0 !
  PARAMETER G(ZRO2_CUB,Y+3:O-2;0)       298.15 +GHHYO15#+0.5*GHSEROO#
 +9.3511*T; 6000 N                                                  REF0 !
  PARAMETER G(ZRO2_CUB,ZR:O-2;0)        298.15 +100000+GHSERZR#
  +2*GHSEROO#;    6000 N                                            REF0 !
  PARAMETER G(ZRO2_CUB,ZR+4:O-2;0)     298.15 +GFFZRO2#; 6000 N   REF0 !
  PARAMETER G(ZRO2_CUB,Y:VA;0)          298.15 +GHSERYY#+122800;
  6000 N                                                            REF0 !
  PARAMETER G(ZRO2_CUB,Y+3:VA;0)        298.15 +GHHYO15#-1.5*GHSEROO#
  +9.3511*T; 6000 N                                                 REF0 !
  PARAMETER G(ZRO2_CUB,ZR:VA;0)         298.15 +100000+GHSERZR#;
  6000 N                                                            REF0 !
  PARAMETER G(ZRO2_CUB,ZR+4:VA;0)      298.15 +GFFZRO2#-2*GHSEROO#;
  6000 N                                                            REF0 !
  PARAMETER G(ZRO2_CUB,Y+3,ZR+4:O-2;0)   298.15 -7.1804599E+04+35*T;
  6000 N                                                            REF0 !
  PARAMETER G(ZRO2_CUB,Y+3,ZR+4:O-2;1)   298.15 +1.7443419E+04-6.4*T;
  6000 N                                                            REF0 !
  PARAMETER G(ZRO2_CUB,ZR,ZR+4:O-2;0)     298.15 -6.6519951E+04
  -1.6012803*T;   6000 N                                            REF0 !
  PARAMETER G(ZRO2_CUB,ZR,ZR+4:O-2;1)    298.15 -2.0014001E+04-42.0084*T;
  6000 N                                                            REF0 !
  PARAMETER G(ZRO2_CUB,Y+3,ZR+4:VA;0)   298.15 -7.1804599E+04+35*T;
  6000 N                                                            REF0 !
  PARAMETER G(ZRO2_CUB,Y+3,ZR+4:VA;1)   298.15 +1.7443419E+04-6.4*T;
  6000 N                                                            REF0 !
  PARAMETER G(ZRO2_CUB,ZR,ZR+4:VA;0)     298.15 -6.6519951E+04
  -1.6012803*T;   6000 N                                            REF0 !
  PARAMETER G(ZRO2_CUB,ZR,ZR+4:VA;1)    298.15 -2.0014001E+04-42.0084*T;
  6000 N                                                            REF0 !

PHASE ZRO2_MONO:I %  2 1   2 !
   CONSTITUENT ZRO2_MONO:I :Y+3,ZR+4 : O-2,VA :  !
  PARAMETER G(ZRO2_MONO,Y+3:O-2;0)       298.15 +GMMYO15#
  +0.5*GHSEROO#+9.3511*T; 6000 N                                    REF0 !
  PARAMETER G(ZRO2_MONO,ZR+4:O-2;0)   298.15 +GMMZRO2#; 6000 N REF0 !
  PARAMETER G(ZRO2_MONO,Y+3:VA;0)   298.15 +GMMYO15#-1.5*GHSEROO#
  +9.3511*T; 6000 N                                                 REF0 !
```

```
  PARAMETER G(ZRO2_MONO,ZR+4:VA;0) 298.15 +GMMZRO2#-2*GHSEROO#;
  6000 N                                                          REF0 !
  PARAMETER G(ZRO2_MONO,Y+3,ZR+4:O-2;0)  298.15 +11000; 6000 N    REF0 !
  PARAMETER G(ZRO2_MONO,Y+3,ZR+4:VA;0)   298.15 +11000; 6000 N    REF0 !

PHASE ZRO2_TETR:I %  2 1   2 !
   CONSTITUENT ZRO2_TETR:I :Y+3,ZR+4 : O-2,VA :  !
  PARAMETER G(ZRO2_TETR,Y+3:O-2;0) 298.15 +GMTYO15#+0.5*GHSEROO#
  +9.3511*T; 6000 N                                               REF0 !
  PARAMETER G(ZRO2_TETR,ZR+4:O-2;0)     298.15 +GTTZRO2#; 6000 N  REF0 !
  PARAMETER G(ZRO2_TETR,Y+3:VA;0)      298.15 +GMTYO15#-1.5*GHSEROO#
  +9.3511*T; 6000 N                                               REF0 !
  PARAMETER G(ZRO2_TETR,ZR+4:VA;0)      298.15 +GTTZRO2#-2*GHSEROO#;
  6000 N                                                          REF0 !
  PARAMETER G(ZRO2_TETR,Y+3,ZR+4:O-2;0)  298.15 –4.2191226E+04
  +25.108568*T;  6000 N                                           REF0 !
  PARAMETER G(ZRO2_TETR,Y+3,ZR+4:VA;0)   298.15 -4.2191226E+04
  +25.108568*T;  6000 N                                           REF0 !

LIST_OF_REFERENCES

NUMBER  SOURCE

!
```

Appendix B

The POP file as an input file for Thermo-Calc

```
ENTER-SYMBOL CONSTANT R=8.31451

ENTER-SYMBOL CONSTANT P0=101325 FAR=96485.309 PAIR=21278

ENTER-SYMBOL CONSTANT P00=100000

ENTER-SYMBOL FUNCTION PHG=760*P/101325;

ENTER-SYMBOL FUNCTION PO2PA=100000*EXP(2*MUR(O)/R/T);

ENTER-SYMBOL FUNCTION LOGPO2=1/LOG(10)*2*MUR(O)/R/T;

ENTER-SYMBOL FUNCTION LOGP1=LOG10(P0*EXP(2*DGMR(O2_GAS)));

ENTER-SYMBOL FUNCTION LNFO=LOG(ACR(O)/X(O));

ENTER-SYMBOL FUNCTION DGOO=MUR(O)-R*T*LOG(100*X(O));

$

$ T0 LINE

$

CREATE-NEW 1, 1
$ T0 line from 1996Yas2
CHANGE-STATUS PHASE ZRO2_MONO=FIX 1
SET-CONDITION P=P00 MUR(O)=0
SET-REF O O2_GAS,, 1E5
SET-CONDITION Y(ZRO2_MONO,Y+3#1)=1e-7
SET-CONDITION T=1387.15
ENTER-SYMBO VAR GMMO=GM(ZRO2_MONO);
EVAL GMMO

$

CREATE-NEW 2, 1
$ T0 line from 1996Yas2
CHANGE-STATUS PHASE ZRO2_TETR=FIX 1
SET-CONDITION P=P00 MUR(O)=0
SET-REF O O2_GAS,, 1E5
SET-CONDITION Y(ZRO2_TETR,Y+3#1)=1e-7
SET-CONDITION T=1387.15
```

```
ENTER-SYMBO FUN DG=(GM(ZRO2_TETR)-GMMO);
EXPERIMENT DG=0:100

$

CREATE-NEW 3, 1
$ T0 line from 1996Yas2
CHANGE-STATUS PHASE ZRO2_MONO=FIX 1
SET-CONDITION P=P00 MUR(O)=0
SET-REF O O2_GAS,, 1E5
SET-CONDITION Y(ZRO2_MONO,Y+3#1)=0.01
SET-CONDITION T=1227.71
EVAL GMMO

$

CREATE-NEW 4, 1
$ T0 line from 1996Yas2
CHANGE-STATUS PHASE ZRO2_TETR=FIX 1
SET-CONDITION P=P00 MUR(O)=0
SET-REF O O2_GAS,, 1E5
SET-CONDITION Y(ZRO2_TETR,Y+3#1)=0.01
SET-CONDITION T=1227.71
EXPERIMENT DG=0:100

$

CREATE-NEW 5, 1
$ T0 line from 1996Yas2
CHANGE-STATUS PHASE ZRO2_MONO=FIX 1
SET-CONDITION P=P00 MUR(O)=0
SET-REF O O2_GAS,, 1E5
SET-CONDITION Y(ZRO2_MONO,Y+3#1)=0.02
SET-CONDITION T=1068.27
EVAL GMMO

$

CREATE-NEW 6, 1
$ T0 line from 1996Yas2
CHANGE-STATUS PHASE ZRO2_TETR=FIX 1
SET-CONDITION P=P00 MUR(O)=0
SET-REF O O2_GAS,, 1E5
SET-CONDITION Y(ZRO2_TETR,Y+3#1)=0.02
SET-CONDITION T=1068.27
EXPERIMENT DG=0:100
```

```
$

CREATE-NEW 7, 1
$ T0 line from 1996Yas2
CHANGE-STATUS PHASE ZRO2_MONO=FIX 1
SET-CONDITION P=P00 MUR(O)=0
SET-REF O O2_GAS,, 1E5
SET-CONDITION Y(ZRO2_MONO,Y+3#1)=0.03
SET-CONDITION T=908.83
EVAL GMMO

$

CREATE-NEW 8, 1
$ T0 line from 1996Yas2
CHANGE-STATUS PHASE ZRO2_TETR=FIX 1
SET-CONDITION P=P00 MUR(O)=0
SET-REF O O2_GAS,, 1E5
SET-CONDITION Y(ZRO2_TETR,Y+3#1)=0.03
SET-CONDITION T=908.83
EXPERIMENT DG=0:100

$

CREATE-NEW 9, 1
$ T0 line from 1996Yas2
CHANGE-STATUS PHASE ZRO2_MONO=FIX 1
SET-CONDITION P=P00 MUR(O)=0
SET-REF O O2_GAS,, 1E5
SET-CONDITION Y(ZRO2_MONO,Y+3#1)=0.04
SET-CONDITION T=749.39
EVAL GMMO

$

CREATE-NEW 10, 1
$ T0 line from 1996Yas2
CHANGE-STATUS PHASE ZRO2_TETR=FIX 1
SET-CONDITION P=P00 MUR(O)=0
SET-REF O O2_GAS,, 1E5
SET-CONDITION Y(ZRO2_TETR,Y+3#1)=0.04
SET-CONDITION T=749.39
EXPERIMENT DG=0:100

$
```

```
CREATE-NEW 11, 1
$ T0 line from 1995Yas
CHANGE-STATUS PHASE ZRO2_MONO=FIX 1
SET-CONDITION P=P00 MUR(O)=0
SET-REF O O2_GAS,, 1E5
SET-CONDITION Y(ZRO2_MONO,Y+3#1)=1e-7
SET-CONDITION T=1478.15
EVAL GMMO

$

CREATE-NEW 12, 1
$ T0 line from 1995Yas
CHANGE-STATUS PHASE ZRO2_TETR=FIX 1
SET-CONDITION P=P00 MUR(O)=0
SET-REF O O2_GAS,, 1E5
SET-CONDITION Y(ZRO2_TETR,Y+3#1)=1e-7
SET-CONDITION T=1478.15
EXPERIMENT DG=0:100

$

CREATE-NEW 13, 1
$ T0 line from 1995Yas
CHANGE-STATUS PHASE ZRO2_MONO=FIX 1
SET-CONDITION P=P00 MUR(O)=0
SET-REF O O2_GAS,, 1E5
SET-CONDITION Y(ZRO2_MONO,Y+3#1)=0.04
SET-CONDITION T=775
EVAL GMMO

$

CREATE-NEW 14, 1
$ T0 line from 1995Yas
CHANGE-STATUS PHASE ZRO2_TETR=FIX 1
SET-CONDITION P=P00 MUR(O)=0
SET-REF O O2_GAS,, 1E5
SET-CONDITION Y(ZRO2_TETR,Y+3#1)=0.04
SET-CONDITION T=775
EXPERIMENT DG=0:100

$

CREATE-NEW 15, 1
$ T0 line from 1984Ruh
```

```
CHANGE-STATUS PHASE ZRO2_MONO=FIX 1
SET-CONDITION P=P00 MUR(O)=0
SET-REF O O2_GAS,, 1E5
SET-CONDITION Y(ZRO2_MONO,Y+3#1)=0.002
SET-CONDITION T=1348.15
EVAL GMMO

$

CREATE-NEW 16, 1
$ T0 line from 1984Ruh
CHANGE-STATUS PHASE ZRO2_TETR=FIX 1
SET-CONDITION P=P00 MUR(O)=0
SET-REF O O2_GAS,, 1E5
SET-CONDITION Y(ZRO2_TETR,Y+3#1)=0.002
SET-CONDITION T=1348.15
EXPERIMENT DG=0:100

$

CREATE-NEW 17, 1
$ T0 line from 1984Ruh
CHANGE-STATUS PHASE ZRO2_MONO=FIX 1
SET-CONDITION P=P00 MUR(O)=0
SET-REF O O2_GAS,, 1E5
SET-CONDITION Y(ZRO2_MONO,Y+3#1)=0.01
SET-CONDITION T=1168.15
EVAL GMMO

$

CREATE-NEW 18, 1
$ T0 line from 1984Ruh
CHANGE-STATUS PHASE ZRO2_TETR=FIX 1
SET-CONDITION P=P00 MUR(O)=0
SET-REF O O2_GAS,, 1E5
SET-CONDITION Y(ZRO2_TETR,Y+3#1)=0.01
SET-CONDITION T=1168.15
EXPERIMENT DG=0:100

$

CREATE-NEW 19, 1
$ T0 line from 1984Ruh
CHANGE-STATUS PHASE ZRO2_MONO=FIX 1
SET-CONDITION P=P00 MUR(O)=0
```

```
SET-REF O O2_GAS,, 1E5
SET-CONDITION Y(ZRO2_MONO,Y+3#1)=0.016
SET-CONDITION T=1040.65
EVAL GMMO

$

CREATE-NEW 20, 1
$ T0 line from 1984Ruh
CHANGE-STATUS PHASE ZRO2_TETR=FIX 1
SET-CONDITION P=P00 MUR(O)=0
SET-REF O O2_GAS,, 1E5
SET-CONDITION Y(ZRO2_TETR,Y+3#1)=0.016
SET-CONDITION T=1040.65
EXPERIMENT DG=0:100

$

CREATE-NEW 21, 1
$ T0 line from 1993Yas
CHANGE-STATUS PHASE ZRO2_MONO=FIX 1
SET-CONDITION P=P00 MUR(O)=0
SET-REF O O2_GAS,, 1E5
SET-CONDITION Y(ZRO2_MONO,Y+3#1)=0.01
SET-CONDITION T=1260.65
EVAL GMMO

$

CREATE-NEW 22, 1
$ T0 line from 1993Yas
CHANGE-STATUS PHASE ZRO2_TETR=FIX 1
SET-CONDITION P=P00 MUR(O)=0
SET-REF O O2_GAS,, 1E5
SET-CONDITION Y(ZRO2_TETR,Y+3#1)=0.01
SET-CONDITION T=1260.65
EXPERIMENT DG=0:100

$

CREATE-NEW 23, 1
$ T0 line from 1993Yas
CHANGE-STATUS PHASE ZRO2_MONO=FIX 1
SET-CONDITION P=P00 MUR(O)=0
SET-REF O O2_GAS,, 1E5
SET-CONDITION Y(ZRO2_MONO,Y+3#1)=0.02
```

```
SET-CONDITION T=1103.15
EVAL GMMO

$

CREATE-NEW 24, 1
$ T0 line from 1993Yas
CHANGE-STATUS PHASE ZRO2_TETR=FIX 1
SET-CONDITION P=P00 MUR(O)=0
SET-REF O O2_GAS,, 1E5
SET-CONDITION Y(ZRO2_TETR,Y+3#1)=0.02
SET-CONDITION T=1103.15
EXPERIMENT DG=0:100

$

CREATE-NEW 25, 1
$ T0 line from 1993Yas
CHANGE-STATUS PHASE ZRO2_MONO=FIX 1
SET-CONDITION P=P00 MUR(O)=0
SET-REF O O2_GAS,, 1E5
SET-CONDITION Y(ZRO2_MONO,Y+3#1)=0.03
SET-CONDITION T=948.15
EVAL GMMO

$

CREATE-NEW 26, 1
$ T0 line from 1993Yas
CHANGE-STATUS PHASE ZRO2_TETR=FIX 1
SET-CONDITION P=P00 MUR(O)=0
SET-REF O O2_GAS,, 1E5
SET-CONDITION Y(ZRO2_TETR,Y+3#1)=0.03
SET-CONDITION T=948.15
EXPERIMENT DG=0:100

$

CREATE-NEW 27, 1
$ T0 line from 1951Duw
CHANGE-STATUS PHASE ZRO2_MONO=FIX 1
SET-CONDITION P=P00 MUR(O)=0
SET-REF O O2_GAS,, 1E5
SET-CONDITION Y(ZRO2_MONO,Y+3#1)=0.02
SET-CONDITION T=1123.15
EVAL GMMO
```

```
$

CREATE-NEW 28, 1
$ T0 line from 1951Duw
CHANGE-STATUS PHASE ZRO2_TETR=FIX 1
SET-CONDITION P=P00 MUR(O)=0
SET-REF O O2_GAS,, 1E5
SET-CONDITION Y(ZRO2_TETR,Y+3#1)=0.02
SET-CONDITION T=1123.15
EXPERIMENT DG=0:100

$

CREATE-NEW 29, 1
$ T0 line from 1986Yos
CHANGE-STATUS PHASE ZRO2_MONO=FIX 1
SET-CONDITION P=P00 MUR(O)=0
SET-REF O O2_GAS,, 1E5
SET-CONDITION Y(ZRO2_MONO,Y+3#1)=0.02
SET-CONDITION T=1013.15
EVAL GMMO

$

CREATE-NEW 30, 1
$ T0 line from 1986Yos
CHANGE-STATUS PHASE ZRO2_TETR=FIX 1
SET-CONDITION P=P00 MUR(O)=0
SET-REF O O2_GAS,, 1E5
SET-CONDITION Y(ZRO2_TETR,Y+3#1)=0.02
SET-CONDITION T=1013.15
EXPERIMENT DG=0:100

$

CREATE-NEW 31, 1
$ T0 line from 1986Yos
CHANGE-STATUS PHASE ZRO2_MONO=FIX 1
SET-CONDITION P=P00 MUR(O)=0
SET-REF O O2_GAS,, 1E5
SET-CONDITION Y(ZRO2_MONO,Y+3#1)=0.03
SET-CONDITION T=803.15
EVAL GMMO

$
```

```
CREATE-NEW 32, 1
$ T0 line from 1986Yos
CHANGE-STATUS PHASE ZRO2_TETR=FIX 1
SET-CONDITION P=P00 MUR(O)=0
SET-REF O O2_GAS,, 1E5
SET-CONDITION Y(ZRO2_TETR,Y+3#1)=0.03
SET-CONDITION T=803.15
EXPERIMENT DG=0:100

$

CREATE-NEW 33, 1
$ T0 line from 1994Sri
CHANGE-STATUS PHASE ZRO2_MONO=FIX 1
SET-CONDITION P=P00 MUR(O)=0
SET-REF O O2_GAS,, 1E5
SET-CONDITION Y(ZRO2_MONO,Y+3#1)=0.02
SET-CONDITION T=1053.15
EVAL GMMO

$

CREATE-NEW 34, 1
$ T0 line from 1994Sri
CHANGE-STATUS PHASE ZRO2_TETR=FIX 1
SET-CONDITION P=P00 MUR(O)=0
SET-REF O O2_GAS,, 1E5
SET-CONDITION Y(ZRO2_TETR,Y+3#1)=0.02
SET-CONDITION T=1053.15
EXPERIMENT DG=0:100

$

CREATE-NEW 35, 1
$ T0 line from 1994Sri
CHANGE-STATUS PHASE ZRO2_MONO=FIX 1
SET-CONDITION P=P00 MUR(O)=0
SET-REF O O2_GAS,, 1E5
SET-CONDITION Y(ZRO2_MONO,Y+3#1)=0.04
SET-CONDITION T=855
EVAL GMMO

$

CREATE-NEW 36, 1
$ T0 line from 1994Sri
```

```
CHANGE-STATUS PHASE ZRO2_TETR=FIX 1
SET-CONDITION P=P00 MUR(O)=0
SET-REF O O2_GAS,, 1E5
SET-CONDITION Y(ZRO2_TETR,Y+3#1)=0.04
SET-CONDITION T=855
EXPERIMENT DG=0:100

$

CREATE-NEW 37, 1
$ T0 line from 1995Yas2
CHANGE-STATUS PHASE ZRO2_MONO=FIX 1
SET-CONDITION P=P00 MUR(O)=0
SET-REF O O2_GAS,, 1E5
SET-CONDITION Y(ZRO2_MONO,Y+3#1)=0.04
SET-CONDITION T=737.5
EVAL GMMO

$

CREATE-NEW 38, 1
$ T0 line from 1995Yas2
CHANGE-STATUS PHASE ZRO2_TETR=FIX 1
SET-CONDITION P=P00 MUR(O)=0
SET-REF O O2_GAS,, 1E5
SET-CONDITION Y(ZRO2_TETR,Y+3#1)=0.04
SET-CONDITION T=737.5
EXPERIMENT DG=0:100

$

CREATE-NEW 39, 1
$ T0 line from 1985Ada
CHANGE-STATUS PHASE ZRO2_MONO=FIX 1
SET-CONDITION P=P00 MUR(O)=0
SET-REF O O2_GAS,, 1E5
SET-CONDITION Y(ZRO2_MONO,Y+3#1)=0.033
SET-CONDITION T=788.15
EVAL GMMO

$

CREATE-NEW 40, 1
$ T0 line from 1985Ada
CHANGE-STATUS PHASE ZRO2_TETR=FIX 1
SET-CONDITION P=P00 MUR(O)=0
```

```
SET-REF O O2_GAS,, 1E5
SET-CONDITION Y(ZRO2_TETR,Y+3#1)=0.033
SET-CONDITION T=788.15
EXPERIMENT DG=0:100

$

CREATE-NEW 41, 1
$ T0 line from 1985Ada
CHANGE-STATUS PHASE ZRO2_MONO=FIX 1
SET-CONDITION P=P00 MUR(O)=0
SET-REF O O2_GAS,, 1E5
SET-CONDITION Y(ZRO2_MONO,Y+3#1)=0.044
SET-CONDITION T=677.5
EVAL GMMO

$

CREATE-NEW 42, 1
$ T0 line from 1985Ada
CHANGE-STATUS PHASE ZRO2_TETR=FIX 1
SET-CONDITION P=P00 MUR(O)=0
SET-REF O O2_GAS,, 1E5
SET-CONDITION Y(ZRO2_TETR,Y+3#1)=0.044
SET-CONDITION T=677.5
EXPERIMENT DG=0:100

$

$ PHASE BOUNDARY

$

TABLE-HEAD 51
CREATE-NEW @@, 1
$ Phase boundary of ZRO2_TETRgonal\ZRO2_TETR+ZRO2_CUB
CHANGE-STATUS PHASE ZRO2_TETR ZRO2_CUB=FIX 1
SET-CONDITION P=P00 MUR(O)=0 T=@1
EXPERIMENT Y(ZRO2_TETR,Y+3#1)=@2:5%
TABLE-VALUES
$ Temp., K  Y(ZRO2_TETR,Y+3#1)
$ from 1984Rueh (Stuttgart)
1873.15      0.0397
1823.15      0.0463
1723.15      0.05
1673.15      0.043
```

```
1573.15      0.0497
$ from 1984Rueh (Cleveland)
1873.15      0.044
1773.15      0.0457
1673.15      0.043
1573.15      0.0497
$ from 1975Sco
2273         0.02
1673         0.035
$ from 1984Lan
1873.15      0.0446
$ from 1997Suz
1658.15      0.0469
1438.15      0.0582
1233.15      0.0723
876.15       0.1132
TABLE-END

$

TABLE-HEAD 71
CREATE-NEW @@, 1
$ Phase boundary of ZRO2_TETRgonal+ZRO2_CUB\ZRO2_CUB
CHANGE-STATUS PHASE ZRO2_TETR ZRO2_CUB=FIX 1
SET-CONDITION P=P00 MUR(O)=0 T=@1
EXPERIMENT Y(ZRO2_CUB,Y+3#1)=@2:5%
TABLE-VALUES
$ Temp., K  Y(ZRO2_CUB,Y+3#1)
$ from 1984Rueh (Stuttgart)
1873.15      0.101
1823.15      0.1174
1723.15      0.1325
1673.15      0.1374
1573.15      0.1377
$ from 1984Rueh (Cleveland)
1873.15      0.115
1773.15      0.1205
1673.15      0.1374
1573.15      0.1354
$ from 1975Sco
2273         0.08
1873         0.126
1673         0.14
$ from 1984Lan
1873.15      0.1146
```

```
$ from 1995Suz
936.15       0.2269504
1171.15      0.1949458
1290.15      0.1785064
1458.15      0.1617647
1599.15      0.1532779
1740.15      0.1447124
TABLE-END

$

TABLE-HEAD 111
CREATE-NEW @@, 1
$ Phase boundary of ZRO2_CUB/ZRO2_CUB+ZR3Y4O12
CHANGE-STATUS PHASE ZRO2_CUB ZR3Y4O12=FIX 1
SET-CONDITION P=P00 MUR(O)=0 T=@1
EXPERIMENT Y(ZRO2_CUB,Y+3#1)=@2:5%
TABLE-VALUES
$ Temp., K  Y(ZRO2_CUB,Y+3#1)
$ from 1983Pas
1373.15      0.4195
1473.15      0.4638
1573.15      0.5058
$ from 1995Suz
958.15       0.3291562
1292.15      0.3948636
1481.15      0.4567901
1623.15      0.515219
TABLE-END

$

TABLE-HEAD 121
CREATE-NEW @@, 1
$ Phase boundary of Liquid/ZRO2_CUB+Liquid
CHANGE-STATUS PHASE ZRO2_CUB IONIC_LIQUID=FIX 1
SET-CONDITION P=P00 MUR(O)=0 Y(IONIC_LIQUID,Y+3#1)=@2
EXPERIMENT T=@1:20
TABLE-VALUES
$ Temp., K          Y(IONIC_LIQUID,Y+3#1)
$ from 1968Rou
2983.15       0.00
3033.15       0.0952381
3063.15       0.1818182
3068.15       0.2608696
3080.15       0.3333333
```

```
3082.15      0.40
3072.15      0.4615385
3062.15      0.5185185
3031.15      0.5714286
3003.15      0.6206897
2964.15      0.6666667
2922.15      0.7096774
2879.15      0.75
2840.15      0.7878788
2787.15      0.8235294
2744.15      0.8571429
2669.15      0.8888889
2643.15      0.9059081
$ from 1970Nog
2979.15      0.00
2977.15      0.0487805
2963.15      0.0952381
2962.15      0.1395349
3001.15      0.1818182
3024.15      0.2222222
3019.15      0.2608696
3009.15      0.3333333
3008.15      0.3673469
3005.15      0.40
2993.15      0.4313725
2990.15      0.4615385
2981.15      0.5185185
2973.15      0.5714286
2948.15      0.6206897
2895.15      0.6666667
2865.15      0.7096774
2818.15      0.75
2722.15      0.8235294
2671.15      0.8571429
2603.15      0.8636364
$ from 1978Stu
2804.15      0.8144635
2771.15      0.837885
2755.15      0.8577955
2715.15      0.884551
2682.15      0.8950276
TABLE-END

$
```

```
TABLE-HEAD 171
CREATE-NEW @@, 1
$ Phase boundary of Liquid/Liquid+Y2O3_HEXagonal
CHANGE-STATUS PHASE IONIC_LIQUID Y2O3_HEX=FIX 1
SET-CONDITION P=P00 MUR(O)=0 Y(IONIC_LIQUID,Y+3#1)=@2
EXPERIMENT T=@1:20
TABLE-VALUES
$ Temp., K          Y(IONIC_LIQUID,Y+3#1)
$ from 1968Rou
2662.15       0.9189189
2674.15       0.9473684
2699.15       0.974359
2712.15       1.00
$ from 1970Nog
2615.15       0.8888889
2624.15       0.9473684
2649.15       1.00
$ from 1978Stu
2681.15       0.9100817
2711.15       0.9293362
2729.15       0.9423585
2747.15       0.9556136
2775.15       0.9994997
TABLE-END

$

TABLE-HEAD 191
CREATE-NEW @@, 1
$ ZRO2_CUB/ZRO2_CUB+Y2O3_CUB Phase Boundary
CHANGE-STATUS PHASE ZRO2_CUB Y2O3_CUB=FIX 1
SET-CONDITION P=P00 MUR(O)=0 T=@1
EXPERIMENT Y(ZRO2_CUB,Y+3#1)=@2:5%
TABLE-VALUES
$ Temp., K  Y(ZRO2_CUB,Y+3#1)
$ from 1977Sco
2473.15       0.811
2273.15       0.733
2223.15       0.722
1973.15       0.665
1673.15       0.637
1573.15       0.634
$ from 1984Jay
1723        0.63
1873        0.645
```

```
$ from 1978Stu
1673       0.61
1923       0.63
2173       0.67
2423       0.70
TABLE-END

$

TABLE-HEAD 211
CREATE-NEW @@, 1
$ ZRO2_CUB+Y2O3_CUB/Y2O3_CUB Phase Boundary
CHANGE-STATUS PHASE ZRO2_CUB Y2O3_CUB=FIX 1
SET-CONDITION P=P00 MUR(O)=0 T=@1
EXPERIMENT Y(Y2O3_CUB,Y+3#1)=@2:5%
TABLE-VALUES
$ Temp., K  Y(Y2O3_CUB,Y+3#1)
$ from 1977Sco
2473.15       0.893
2273.15       0.852
2223.15       0.842
1973.15       0.79
1673.15       0.748
1573.15       0.743
$ from 1984Jay
1723       0.75
1873       0.77
$ from 1978Stu
1673       0.90
1923       0.88
2173       0.87
2423       0.86
$ from 1988Stu
1873       0.893
2073       0.889
2223       0.883
2373       0.877
TABLE-END

$

$ENTROPY

$

$ Disordering temperature for ZR3Y4O12 from 1977Sco
```

```
CREATE-NEW 301, 1
CHANGE-STATUS PHASE ZRO2_CUB=FIX 1
CHANGE-STATUS PHASE ZR3Y4O12=FIX 0
SET-CONDITION P=P00 MUR(O)=0
SET-CONDITION Y(ZRO2_CUB,Y+3#1)=0.5714
SET-REF O O2_GAS,, 1E5
SET-ALL-START 1643 Y
EXPERIMENT T=1643:5

$

$ Entropy of Disordering for ZR3Y4O12 from Bengt, 20020528
CREATE-NEW 302, 1
CHANGE-STATUS PHASE ZRO2_CUB ZR3Y4O12=FIX 1
SET-CONDITION P=P00 MUR(O)=0
SET-CONDITION Y(ZRO2_CUB,Y+3#1)=0.5714
SET-REF O O2_GAS,, 1E5
ENTER-SYMBOL FUNCTION DS=(SM(ZRO2_CUB)-SM(ZR3Y4O12))*19;
EXPERIMENT DS=84:1

$

$ACTIVITY

$

CREATE-NEW 401, 1
$ ZrO2 activities in ZRO2_CUB phase from 1985Bel
CHANGE-STATUS PHASE ZRO2_CUB=FIX 1
SET-CONDITION P=P00 MUR(O)=0 T=2773 Y(ZRO2_CUB,Y+3#1)=1e-7
ENTER-SYMBOL VAR MZO00=MUR(ZR)+2*MUR(O);
EVAL MZO00

$

CREATE-NEW 402, 1
$ ZrO2 activities in ZRO2_CUB phase from 1985Bel
CHANGE-STATUS PHASE ZRO2_CUB=FIX 1
SET-CONDITION P=P00 MUR(O)=0 T=2773 Y(ZRO2_CUB,Y+3#1)=0.1818
ENTER-SYMBOL FUN AZR=EXP((MUR(ZR)+2*MUR(O)-MZO00)/8.314/2773);
EXPERIMENT AZR=0.837:10%

$

CREATE-NEW 403, 1
$ ZrO2 activities in ZRO2_CUB phase from 1985Bel
```

```
CHANGE-STATUS PHASE ZRO2_CUB=FIX 1
SET-CONDITION P=P00 MUR(O)=0 T=2773 Y(ZRO2_CUB,Y+3#1)=1e-7
EVAL MZO00

$

CREATE-NEW 404, 1
$ ZrO2 activities in ZRO2_CUB phase from 1985Bel
CHANGE-STATUS PHASE ZRO2_CUB=FIX 1
SET-CONDITION P=P00 MUR(O)=0 T=2773 Y(ZRO2_CUB,Y+3#1)=0.3333
EXPERIMENT AZR=0.68:10%

$

CREATE-NEW 405, 1
$ ZrO2 activities in ZRO2_CUB phase from 1985Bel
CHANGE-STATUS PHASE ZRO2_CUB=FIX 1
SET-CONDITION P=P00 MUR(O)=0 T=2773 Y(ZRO2_CUB,Y+3#1)=1e-7
EVAL MZO00

$

CREATE-NEW 406, 1
$ ZrO2 activities in ZRO2_CUB phase from 1985Bel
CHANGE-STATUS PHASE ZRO2_CUB=FIX 1
SET-CONDITION P=P00 MUR(O)=0 T=2773 Y(ZRO2_CUB,Y+3#1)=0.4615
EXPERIMENT AZR=0.49:10%

$

CREATE-NEW 407, 1
$ ZrO2 activities in ZRO2_CUB phase from 1985Bel
CHANGE-STATUS PHASE ZRO2_CUB=FIX 1
SET-CONDITION P=P00 MUR(O)=0 T=2773 Y(ZRO2_CUB,Y+3#1)=1e-7
EVAL MZO00

$

CREATE-NEW 408, 1
$ ZrO2 activities in ZRO2_CUB phase from 1985Bel
CHANGE-STATUS PHASE ZRO2_CUB=FIX 1
SET-CONDITION P=P00 MUR(O)=0 T=2773 Y(ZRO2_CUB,Y+3#1)=0.5714
EXPERIMENT AZR=0.33:10%

$

CREATE-NEW 409, 1
```

```
$ ZrO2 activities in ZRO2_CUB phase from 1985Bel
CHANGE-STATUS PHASE ZRO2_CUB=FIX 1
SET-CONDITION P=P00 MUR(O)=0 T=2773 Y(ZRO2_CUB,Y+3#1)=1e-7
EVAL MZO00

$

CREATE-NEW 410, 1
$ ZrO2 activities in ZRO2_CUB phase from 1985Bel
CHANGE-STATUS PHASE ZRO2_CUB=FIX 1
SET-CONDITION P=P00 MUR(O)=0 T=2773 Y(ZRO2_CUB,Y+3#1)=0.6667
EXPERIMENT AZR=0.23:10%

$

CREATE-NEW 451, 1
$ Y2O3 activities in ZRO2_CUB phase from 1984Vin
CHANGE-STATUS PHASE ZRO2_CUB=FIX 1
SET-CONDITION P=P00 MUR(O)=0 T=1300 Y(ZRO2_CUB,Zr+4#1)=1e-7
ENTER-SYMBOL VAR MYO00=2*MUR(Y)+3*MUR(O);
EVAL MYO00

$

CREATE-NEW 452, 1
$ Y2O3 activities in ZRO2_CUB phase from 1984Vin
CHANGE-STATUS PHASE ZRO2_CUB=FIX 1
SET-CONDITION P=P00 MUR(O)=0 T=1300 Y(ZRO2_CUB,Y+3#1)=0.261
ENTER-SYMBOL FUN
                    AY2O3_CUB=EXP((2*MUR(Y)+3*MUR(O)-MYO00)/8.314/1300);
EXPERIMENT AY2O3_CUB=0.00079:10%

$

CREATE-NEW 453, 1
$ Y2O3 activities in ZRO2_CUB+ZRO2_TETRgonal two phases REGION from 1984Vin
CHANGE-STATUS PHASE ZRO2_CUB=FIX 1
SET-CONDITION P=P00 MUR(O)=0 T=1300 Y(ZRO2_CUB,Zr+4#1)=1e-7
EVAL MYO00

$

CREATE-NEW 454, 1
$ Y2O3 activities in ZRO2_CUB+ZRO2_TETRgonal two phases REGION from 1984Vin
CHANGE-STATUS PHASE ZRO2_CUB ZRO2_TETR=FIX 1
SET-CONDITION P=P00 MUR(O)=0 T=1300
```

```
EXPERIMENT AY2O3_CUB=0.00002:10%

$

CREATE-NEW 455, 1
$ Y2O3 activities in ZRO2_CUB phase from 1984Vin
CHANGE-STATUS PHASE ZRO2_CUB=FIX 1
SET-CONDITION P=P00 MUR(O)=0 T=1300 Y(ZRO2_CUB,Zr+4#1)=1e-7
EVAL MYO00

$

CREATE-NEW 456, 1
$ Y2O3 activities in ZRO2_CUB phase from 1984Vin
CHANGE-STATUS PHASE ZRO2_CUB=FIX 1
SET-CONDITION P=P00 MUR(O)=0 T=1300 Y(ZRO2_CUB,Y+3#1)=0.4
EXPERIMENT AY2O3_CUB=0.022:10%

$

CREATE-NEW 457, 1
$ Y2O3 activities in ZRO2_CUB phase from 1984Vin
CHANGE-STATUS PHASE ZRO2_CUB=FIX 1
SET-CONDITION P=P00 MUR(O)=0 T=1300 Y(ZRO2_CUB,Zr+4#1)=1e-7
EVAL MYO00

$

CREATE-NEW 458, 1
$ Y2O3 activities in ZRO2_CUB phase from 1984Vin
CHANGE-STATUS PHASE ZRO2_CUB=FIX 1
SET-CONDITION P=P00 MUR(O)=0 T=1300 Y(ZRO2_CUB,Y+3#1)=0.46
EXPERIMENT AY2O3_CUB=0.082:10%

$

CREATE-NEW 459, 1
$ Y2O3 activities in ZRO2_CUB phase from 1984Vin
CHANGE-STATUS PHASE ZRO2_CUB=FIX 1
SET-CONDITION P=P00 MUR(O)=0 T=1300 Y(ZRO2_CUB,Zr+4#1)=1e-7
EVAL MYO00

$

CREATE-NEW 460, 1
$ Y2O3 activities in ZRO2_CUB phase from 1984Vin
CHANGE-STATUS PHASE ZRO2_CUB=FIX 1
```

```
SET-CONDITION P=P00 MUR(O)=0 T=1300 Y(ZRO2_CUB,Y+3#1)=0.52
EXPERIMENT AY2O3_CUB=0.34:10%

$

CREATE-NEW 461, 1
$ Y2O3 activities in ZRO2_CUB phase from 1985Bel
CHANGE-STATUS PHASE ZRO2_CUB=FIX 1
SET-CONDITION P=P00 MUR(O)=0 T=2773 Y(ZRO2_CUB,Zr+4#1)=1e-7
EVAL MYO00

$

CREATE-NEW 462, 1
$ Y2O3 activities in ZRO2_CUB phase from 1985Bel
CHANGE-STATUS PHASE ZRO2_CUB=FIX 1
SET-CONDITION P=P00 MUR(O)=0 T=2773 Y(ZRO2_CUB,Y+3#1)=0.1818
ENTER-SYMBOL FUN AY1=EXP((2*MUR(Y)+3*MUR(O)-MYO00)/8.314/2773);
EXPERIMENT AY1=0.009:10%

$

CREATE-NEW 463, 1
$ Y2O3 activities in ZRO2_CUB phase from 1985Bel
CHANGE-STATUS PHASE ZRO2_CUB=FIX 1
SET-CONDITION P=P00 MUR(O)=0 T=2773 Y(ZRO2_CUB,Zr+4#1)=1e-7
EVAL MYO00

$

CREATE-NEW 464, 1
$ Y2O3 activities in ZRO2_CUB phase from 1985Bel
CHANGE-STATUS PHASE ZRO2_CUB=FIX 1
SET-CONDITION P=P00 MUR(O)=0 T=2773 Y(ZRO2_CUB,Y+3#1)=0.3333
EXPERIMENT AY1=0.03:10%

$

CREATE-NEW 465, 1
$ Y2O3 activities in ZRO2_CUB phase from 1985Bel
CHANGE-STATUS PHASE ZRO2_CUB=FIX 1
SET-CONDITION P=P00 MUR(O)=0 T=2773 Y(ZRO2_CUB,Zr+4#1)=1e-7
EVAL MYO00

$

CREATE-NEW 466, 1
```

```
$ Y2O3 activities in ZRO2_CUB phase from 1985Bel
CHANGE-STATUS PHASE ZRO2_CUB=FIX 1
SET-CONDITION P=P00 MUR(O)=0 T=2773 Y(ZRO2_CUB,Y+3#1)=0.4615
EXPERIMENT AY1=0.081:10%

$

CREATE-NEW 467, 1
$ Y2O3 activities in ZRO2_CUB phase from 1985Bel
CHANGE-STATUS PHASE ZRO2_CUB=FIX 1
SET-CONDITION P=P00 MUR(O)=0 T=2773 Y(ZRO2_CUB,Zr+4#1)=1e-7
EVAL MYO00

$

CREATE-NEW 468, 1
$ Y2O3 activities in ZRO2_CUB phase from 1985Bel
CHANGE-STATUS PHASE ZRO2_CUB=FIX 1
SET-CONDITION P=P00 MUR(O)=0 T=2773 Y(ZRO2_CUB,Y+3#1)=0.5714
EXPERIMENT AY1=0.168:10%

$

CREATE-NEW 469, 1
$ Y2O3 activities in ZRO2_CUB phase from 1985Bel
CHANGE-STATUS PHASE ZRO2_CUB=FIX 1
SET-CONDITION P=P00 MUR(O)=0 T=2773 Y(ZRO2_CUB,Zr+4#1)=1e-7
EVAL MYO00

$

CREATE-NEW 470, 1
$ Y2O3 activities in ZRO2_CUB phase from 1985Bel
CHANGE-STATUS PHASE ZRO2_CUB=FIX 1
SET-CONDITION P=P00 MUR(O)=0 T=2773 Y(ZRO2_CUB,Y+3#1)=0.6667
EXPERIMENT AY1=0.27:10%

$

$ CHEMICAL POTENTIAL

$

CREATE-NEW 481, 1
$ Delta-mur(Y2O3) in Zr3Y4O12+Y2O3_CUB two-phase REGION from 1990Zai
CHANGE-STATUS PHASE ZR3Y4O12 Y2O3_CUB=FIX 1
SET-CONDITION P=P00 MUR(O)=0 T=1273 Y(Y2O3_CUB,Zr+4#1)=1e-7
```

```
EVAL MYO00

$

CREATE-NEW 482, 1
$ Delta-mur(Y2O3) in Zr3Y4O12+Y2O3_CUB two-phase REGION from 1990Zai
CHANGE-STATUS PHASE Y2O3_CUB=FIX 1
SET-CONDITION P=P00 MUR(O)=0 T=1273
ENTER-SYMBOL FUN MURYO=2*MUR(Y)+3*MUR(O)-MYO00;
EXPERIMENT MURYO=-3130:10%

$

CREATE-NEW 483, 1
$ Delta-mur(Y2O3) in Y2O3_CUB phase from 1990Zai
CHANGE-STATUS PHASE Y2O3_CUB=FIX 1
SET-CONDITION P=P00 MUR(O)=0 T=1273 Y(Y2O3_CUB,Zr+4#1)=1e-7
EVAL MYO00

$

CREATE-NEW 484, 1
$ Delta-mur(Y2O3) in Y2O3_CUB phase from 1990Zai
CHANGE-STATUS PHASE Y2O3_CUB=FIX 1
SET-CONDITION P=P00 MUR(O)=0 T=1273 Y(Y2O3_CUB,Y+3#1)=0.9189
EXPERIMENT MURYO=-2440:10%

$

CREATE-NEW 485, 1
$ Delta-mur(Y2O3) in Y2O3_CUB phase from 1990Zai
CHANGE-STATUS PHASE Y2O3_CUB=FIX 1
SET-CONDITION P=P00 MUR(O)=0 T=1273 Y(Y2O3_CUB,Zr+4#1)=1e-7
EVAL MYO00

$

CREATE-NEW 486, 1
$ Delta-mur(Y2O3) in Y2O3_CUB phase from 1990Zai
CHANGE-STATUS PHASE Y2O3_CUB=FIX 1
SET-CONDITION P=P00 MUR(O)=0 T=1273 Y(Y2O3_CUB,Y+3#1)=0.9743
EXPERIMENT MURYO=-1130:10%

$

CREATE-NEW 491, 1
$ Delta-mur(ZrO2) in ZRO2_CUB phase from 1994Zai
```

```
CHANGE-STATUS PHASE ZRO2_CUB=FIX 1
SET-CONDITION P=P00 MUR(O)=0 T=1273 Y(ZRO2_CUB,Y+3#1)=1E-7
EVAL MZO00

$

CREATE-NEW 492, 1
$ Delta-mur(ZrO2) in ZRO2_CUB phase from 1994Zai
CHANGE-STATUS PHASE ZRO2_CUB=FIX 1
SET-CONDITION P=P00 MUR(O)=0 T=1273 Y(ZRO2_CUB,Y+3#1)=0.2609
ENTER-SYMBO FUN MURZO=MUR(ZR)+2*MUR(O)-MZO00;
EXPERIMENT MURZO=-14600:10%

$

CREATE-NEW 493, 1
$ Delta-mur(ZrO2) in ZRO2_CUB phase from 1994Zai
CHANGE-STATUS PHASE ZRO2_CUB=FIX 1
SET-CONDITION P=P00 MUR(O)=0 T=1273 Y(ZRO2_CUB,Y+3#1)=1E-7
EVAL MZO00

$

CREATE-NEW 494, 1
$ Delta-mur(ZrO2) in ZRO2_CUB phase from 1994Zai
CHANGE-STATUS PHASE ZRO2_CUB=FIX 1
SET-CONDITION P=P00 MUR(O)=0 T=1273 Y(ZRO2_CUB,Y+3#1)=0.3333
EXPERIMENT MURZO=-19200:10%

$

CREATE-NEW 495, 1
$ Delta-mur(ZrO2) in ZRO2_CUB phase from 1994Zai
CHANGE-STATUS PHASE ZRO2_CUB=FIX 1
SET-CONDITION P=P00 MUR(O)=0 T=1273 Y(ZRO2_CUB,Y+3#1)=1E-7
EVAL MZO00

$

CREATE-NEW 496, 1
$ Delta-mur(ZrO2) in ZRO2_CUB phase from 1994Zai
CHANGE-STATUS PHASE ZRO2_CUB=FIX 1
SET-CONDITION P=P00 MUR(O)=0 T=1273 Y(ZRO2_CUB,Y+3#1)=0.4
EXPERIMENT MURZO=-21800:10%

$
```

```
CREATE-NEW 497, 1
$ Delta-mur(ZrO2) in ZRO2_CUB phase from 1994Zai
CHANGE-STATUS PHASE ZRO2_CUB=FIX 1
SET-CONDITION P=P00 MUR(O)=0 T=1273 Y(ZRO2_CUB,Y+3#1)=1E-7
EVAL MZO00

$

CREATE-NEW 498, 1
$ Delta-mur(ZrO2) in ZRO2_CUB phase from 1994Zai
CHANGE-STATUS PHASE ZRO2_CUB=FIX 1
SET-CONDITION P=P00 MUR(O)=0 T=1273 Y(ZRO2_CUB,Y+3#1)=0.4615
EXPERIMENT MURZO=-22300:10%

$

CREATE-NEW 499, 1
$ Delta-mur(ZrO2) in ZRO2_CUB phase from 1994Zai
CHANGE-STATUS PHASE ZRO2_CUB=FIX 1
SET-CONDITION P=P00 MUR(O)=0 T=1273 Y(ZRO2_CUB,Y+3#1)=1E-7
EVAL MZO00

$

CREATE-NEW 500, 1
$ Delta-mur(ZrO2) in ZRO2_CUB phase from 1994Zai
CHANGE-STATUS PHASE ZRO2_CUB=FIX 1
SET-CONDITION P=P00 MUR(O)=0 T=1273 Y(ZRO2_CUB,Y+3#1)=0.5185
EXPERIMENT MURZO=-26400:10%

$

CREATE-NEW 501, 1
$ Delta-mur(ZrO2) in ZRO2_CUB phase from 1994Zai
CHANGE-STATUS PHASE ZRO2_CUB=FIX 1
SET-CONDITION P=P00 MUR(O)=0 T=1273 Y(ZRO2_CUB,Y+3#1)=1E-7
EVAL MZO00

$

CREATE-NEW 502, 1
$ Delta-mur(ZrO2) in ZRO2_CUB phase from 1994Zai
CHANGE-STATUS PHASE ZRO2_CUB=FIX 1
SET-CONDITION P=P00 MUR(O)=0 T=1273 Y(ZRO2_CUB,Y+3#1)=0.5507
EXPERIMENT MURZO=-26400:10%

$
```

```
$ HEAT CAPACITY

$

CREATE-NEW 515, 1
$ Heat capacity of pure ZRO2_MONOclinic ZrO2 from 1999Toj2
CHANGE-STATUS PHASE ZRO2_MONO=FIX 1
SET-CONDITION P=P00 MUR(O)=0 T=300 Y(ZRO2_MONO,Y+3#1)=1E-7
ENTER-SYMBO FUN CPZRO2_MONO=H(ZRO2_MONO).T;
EXPERIMENT CPZRO2_MONO=56.33:10%

$

CREATE-NEW 516, 1
$ Heat capacity of ZRO2_CUB phase from 1999Toj2
CHANGE-STATUS PHASE ZRO2_CUB=FIX 1.0776
SET-CONDITION P=P00 MUR(O)=0 T=300 Y(ZRO2_CUB,Y+3#1)=0.144
ENTER-SYMBO FUN CPZRO2_CUB=H(ZRO2_CUB).T;
EXPERIMENT CPZRO2_CUB=60.40:10%

$

CREATE-NEW 517, 1
$ Heat capacity of ZRO2_CUB phase from 1999Toj
CHANGE-STATUS PHASE ZRO2_CUB=FIX 1.097
SET-CONDITION P=P00 MUR(O)=0 T=300 Y(ZRO2_CUB,Y+3#1)=0.1768
EXPERIMENT CPZRO2_CUB=61.22:10%

$

CREATE-NEW 518, 1
$ Heat capacity of ZRO2_CUB phase from 1999Toj
CHANGE-STATUS PHASE ZRO2_CUB=FIX 1.1135
SET-CONDITION P=P00 MUR(O)=0 T=300 Y(ZRO2_CUB,Y+3#1)=0.2039
EXPERIMENT CPZRO2_CUB=61.81:10%

$

SAVE
```

VITA

MOHAMMAD ASADIKIYA

Born, Tehran, Iran

Azad University, Zanjan, Iran. (Oct. 2002 – Sep. 2006),
B.S. in Mechanical Engineering - Designing of Solids,

Sharif University of Technology, Tehran, Iran. (Feb. 2007 – Jul. 2009),
M.S. in Materials Engineering - Corrosion & Protection,

Florida International University (FIU), Miami, FL, USA. (Apr. 2013 – Nov. 2017),
PhD in Materials Science and Engineering,

SELECTED PUBLICATIONS AND PRESENTATIONS

Asadikiya, M., P. Foroughi,Y. Zhong, Re-Evaluation of the Thermodynamic Equilibria on the Zirconia-Rich Side of the ZrO_2-$YO_{1.5}$ System, Calphad, Submitted, 2017.

Asadikiya, M., Y. Zhong, Oxygen Ion Mobility and Conductivity Prediction in Cubic Yttria-Stabilized Zirconia Single Crystals, Journal of Materials Science, DOI:10.1007/s10853-017-1625-1, 2017.

Asadikiya, M., et al., Integrated Investigation of the $Li_4Ti_5O_{12}$ Phase Stability, Ionics, DOI:10.1007/s11581-017-2248-x, 2017.

Asadikiya, M., et al., The Effect of Sintering Parameters on Spark Plasma Sintering of B_4C, Ceramics International, DOI:10.1016/j.ceramint.2017.05.167, 2017.

Asadikiya, M., et al., Thermodynamic Modeling and Investigation of the Oxygen Effect on the Sintering of B_4C, Journal of Alloys and Compounds, 699(2017): 1022-1029.

Asadikiya, M., et al., Phase Diagram for a Nano-Yttria-Stabilized Zirconia System, RSC Advances, 6.21 (2016): 17438-17445.

Asadikiya, M. and M. Ghorbani, Effect of Inhibitors on the Corrosion of Automotive Aluminum Alloy in Ethylene Glycol-Water Mixture, Corrosion, 67.12 (2011): 126001-1.

Asadikiya, M., et al., The role of CALPHAD approach in the sintering of B_4C with SiC as a sintering aid by spark plasma sintering technique, Additive Manufacturing and Strategic Technologies in Advanced Ceramics: Ceramic Transactions, 2016. 258: p. 185-191.

Asadikiya, M. and Y. Zhong, Oxygen Ion Mobility and Conductivity Prediction in Cubic Yttria-stabilized Zirconia Single Crystals, MS&T 2017, Pittsburgh, Pennsylvania, USA, October 2017.

Asadikiya, M. and Y. Zhong, Re-Evaluation of the Thermodynamic Equilibria on the Zirconia-Rich Side of the ZrO_2-$YO_{1.5}$ System, MS&T 2017, Pittsburgh, Pennsylvania, USA, October 2017.

Asadikiya, M. and Y. Zhong, Prediction of Cubic-YSZ Conductivity by Applying the CALPHAD Approach, ICACC 2017, Daytona Beach, Florida, USA, January 2017.

Asadikiya, M., et al., The Effect of Sintering Parameters on the Properties of B_4C Samples Sintered by SPS, ICACC 2017, Daytona Beach, Florida, USA, January 2017.

Asadikiya, M. and Y. Zhong, Study the Effect of Oxygen on the SPS of B_4C by Applying the CALPHAD Approach, MS&T 2016, Salt Lake City, Utah, USA, October 2016.

Asadikiya, M., P. Singh, Y. Zhong, Investigation of Mn-YSZ Conductivity by Applying the CALPHAD Approach, MS&T 2016, Salt Lake City, Utah, USA, October 2016.

Asadikiya, M., et al., Revising the Thermodynamic Database of ZrO_2-Y_2O_3 System, 2016 MRS Spring Meeting & Exhibit, Phoenix, Arizona, USA, March 2016.

Asadikiya, M., et al., Phase Stability of Nano-sized Yttria Stabilized Zirconia System, TMS 2016, Nashville, Tennessee, USA, February 2016.

Asadikiya, M. and Y. Zhong, Investigation of the Ionic Conductivity of C-ZrO_2 by Applying the CALPHAD Approach, TMS 2016, Nashville, Tennessee, USA, February 2016.

Asadikiya, M. and Y. Zhong, Integrated Investigation on the Amorphization Behavior of B_4C, ICACC 2016, Daytona Beach, Florida, USA, January 2016.

Asadikiya, M. and Y. Zhong, The application of CALPHAD Approach in the Nano-sized YSZ (n-YSZ) Phase Diagram, ICACC 2016, Daytona Beach, Florida, USA, January 2016.

Asadikiya, M., et al., Investigation of the Amorphization Behavior of B_4C by Doping, MS&T 2015, Columbus, Ohio, USA, October 2015.

Asadikiya, M. and Y. Zhong, Developing the Phase Diagram of Nano-Yttria-Stabilized Zirconia by Applying the CALPHAD Approach, MS&T 2015, Columbus, Ohio, USA, October 2015.

Asadikiya, M., et al., The Effect of Impurities on the Properties of SPS Sintered B_4C, TMS 2015, Orlando, Florida, USA, March 2015.

Asadikiya, M. et al., Using Sintering Aids in SPS of B_4C with the Help from Computational Thermodynamics, TMS 2015, Orlando, Florida, USA, March 2015.

Li, N., M. Asadikiya, Y. Zhong, P. Singh, Evolution of Porous YSZ Surface Morphology in YSZ-MnO_x System, Journal of the American Ceramic Society-Submitted, 2017.